Exploring the transition from sticking to bouncing for millimeter-sized dust aggregates

Von der Fakultät für Elektrotechnik, Informationstechnik, Physik
der Technischen Universität Carolo-Wilhelmina
zu Braunschweig
zur Erlangung des Grades eines
Doktors der Naturwissenschaften
(Dr.rer.nat.)
genehmigte
Dissertation

von René Weidling
aus Hameln

eingereicht am: 28.11.2016
Disputation am: 16.03.2017
1. Referent: Prof. Dr. Jürgen Blum
2. Referent: Prof. Dr. Gerhard Wurm
Druckjahr: 2017

Vorabveröffentlichungen der Dissertation

Teilergebnisse aus dieser Arbeit wurden mit Genehmigung der Fakultät für Elektrotechnik, Informationstechnik, Physik, vertreten durch den Mentor der Arbeit, in folgenden Beitragen vorab veröffentlicht:

Publikationen

Weidling, R. and Blum, J. (2015). *Free collisions in a microgravity many-particle experiment. IV. - Three-dimensional analysis of collision properties.* Icarus, 253: 31–39.

Weidling, R., Güttler, C., and Blum, J. (2012). *Free collisions in a microgravity many-particle experiment. I. Dust aggregate sticking at low velocities.* Icarus, 218:688–700.

Tagungsbeiträge

Weidling, R. and Blum, J., *Three-dimensional collision analysis of millimeter-sized dust aggregates*, Planet Formation and Evolution 2014, Kiel, Germany, 8.-10. Oktober 2014.

Weidling, R., Güttler, C., Kothe, S., and Blum, J., *Improving collision models of dust aggregates with MEDEA*, Dust Growth in Star- & Planet-Forming Environments, Heidelberg, Germany, 22.-25. Juli 2013.

Weidling, R., Kothe, S., and Blum, J., *A new approach to modeling collisions of protoplanetary dust aggregates*, Protostars & Planets VI, Heidelberg, Germany, 15.-20. Juli 2013.

Weidling, R., Beitz, E., Blum, J., Güttler, C., and Kothe, S., *Dust-aggregate collisions at low velocities*, Planet Formation and Evolution 2012, München, Germany, 3.-7. September 2012.

Weidling, R., Güttler, C., and Blum, J., *Low-velocity collisions of millimeter-sized dust aggregates*, Dust and grains in low gravity and space environment, Nordwijk, Niederlande, 2.-4. Mai 2012.

Weidling, R., Blum, J., Brisset, J., Güttler, C., Heißelmann, D., and Kothe, S., *MEDEA and SPACE: experiment hardware on planet formation*, Next-Generation Suborbital Researchers Conference 2012, Palo Alto, USA, 27.-29. Februar 2012.

Weidling, R., Güttler, C., and Blum, J., *Free Collisions at Low Velocities*, EPSC-DPS Joint Meeting 2011, Nantes, Frankreich, 2.-7. Oktober 2011.

Weidling, R., Güttler, C., and Blum, J., *Sticking of Dust Aggregates at Low Velocities*, EPSC-DPS Joint Meeting 2011, Nantes, Frankreich, 2.-7. Oktober 2011.

Weidling, R., Güttler, C., Blum, J., and Colwell, J., *Aggregation of Millimeter-Sized Dust Particles in MEDEA*, Next-Generation Suborbital Researchers Conference 2011, Orlando, USA, 27. Februar - 2. März 2011.

Weidling, R., Güttler, C., and Blum, J., *Collisional Evolution of a Many-Particle System of Dust*, Planet Formation and Evolution 2011, Göttingen, Deutschland, 14.-16. Februar 2011.

Contents

Abstract

In the past years, systematic star surveys with dedicated instruments such as the *Kepler* spacecraft or the *HARPS* spectrometer (High Accuracy Radial Velocity Searcher) have revealed the existence of thousands of planets outside of our solar system. These findings have renewed the interest in the formation process of planets. At the same time, they provide a challenge to researchers in providing a multitude of possible orbital configurations that models must be able to explain.

In the early phases of planet formation, growth is governed by intermolecular forces and not yet by gravity. Starting at micrometer sizes, dust particles collide with each other and initially stick together due to the van der Waals force to form larger aggregates. Laboratory experiments are an important means of exploring the outcome of such collisions. The results are then used as input for growth simulations which follow the evolution of the dust particles. In one such simulation, Zsom et al. (2010) found the transition from sticking to bouncing to be important for the maximum size the dust aggregates can grow to.

In this work, an experimental setup suitable for generating collisions between millimeter-sized dust aggregates at velocities of millimeters to centimeters per second under microgravity conditions is presented. This is the velocity range where the sticking-bouncing transition is expected to occur. Additionally, a numerical model for these collisions is developed and used to predict the outcome of collisions for aggregates of other sizes. Furthermore, a comparison between an analysis of the experimental results using two- and three-dimensional data is made. It shows that for velocity evaluation 2D data from just one camera perspective is sufficient, while accurate values for the coefficient of restitution and the impact parameter require 3D input. The experimental results show the transition zone between sticking and bouncing to be much broader than assumed previously.

Zusammenfassung

In den vergangenen Jahren wurden bei der systematischen Untersuchung von Sternen mit speziellen Instrumenten wie dem *Kepler*-Weltraumteleskop oder dem *HARPS*-Spektrometer (High Accuracy Radial Velocity Searcher) tausende Planeten außerhalb unseres Sonnensystems entdeckt. Während diese Entdeckungen das Interesse an den genauen Prozessen die zur Entstehung von Planeten führen erneuert haben, stellen sie gleichermaßen Forscher vor die Herausforderung, dass ihre Modelle eine Vielzahl an möglichen Bahnparametern der so entstandenen Planetensysteme erklären können müssen.

In der Frühphase der Planetenentstehung wird das Wachstum von Teilchen nicht durch Gravitation, sondern durch intermolekulare Kräfte bestimmt. Anfänglich etwa mikrometergroße Staubteilchen kollidieren miteinander und haften aufgrund von Van-der-Waals-Kräften aneinander. Laborexperimente dienen dazu, die Resultate solcher Kollisionen zu untersuchen und zu klassifizieren. Daraus kann dann ein Kollisionsmodell erstellt werden, auf Grundlage dessen Wachstumssimulationen durchgeführt werden können, die die Entwicklung der Staubteilchen vorhersagen. Zsom et al. (2010) haben ein solches Modell entwickelt und dabei herausgefunden, dass es für die maximale Größe zu denen die Staubaggregate wachsen können, von entscheidender Bedeutung ist unter welchen Voraussetzungen diese in Kollisionen aneinander haften bleiben oder voneinander abprallen.

In dieser Arbeit wird ein Versuchsaufbau vorgestellt, mit dem sich Kollisionen von millimetergroßen Staubaggregaten bei Geschwindigkeiten von Millimetern bis Zentimetern pro Sekunde unter Schwerelosigkeitsbedingungen untersuchen lassen. In diesem Geschwindigkeitsbereich wird der Übergang von Haftung zu Abprallen vermutet. Weiterhin wird ein Kollisionsmodell basierend auf den Ergebnissen der Kollisionen millimetergroßer Staubagglomerate entwickelt und geprüft, ob Vorraussagen für Kollisionen von Aggregaten anderer Größe getroffen werden können. Darüber hinaus werden die Ergebnisse des Experiments einmal basierend auf zwei- und einmal basierend auf dreidimensionalen Daten ausgewertet. Ein Vergleich zeigt, dass es für die Ermittlung von Kollisionsgeschwindigkeiten ausreicht, 2D-Daten zu benutzen, während für den Restitutionskoeffizienten und den Impaktparameter 3D-Informationen benötigt werden. Die Ergebnisse der Experimente deuten darauf hin, dass dieser Übergangsbereich von haftenden zu abprallenden Stößen deutlich breiter ist als bisher angenommen.

1 Introduction

The night sky has fascinated mankind for thousands of years. In the past, one prominent question for philosophers and scientists alike has been whether or not the Earth or our Solar System are unique. Only 25 years ago, no planet outside of our solar system had been discovered with certainty. Today, several thousand extrasolar planets (exoplanets) are known, some of them were even observed directly by telescopes (e.g. Kalas et al. 2008, Currie et al. 2012). Modern star surveys revealed that most stars are orbited by at least one planet (Fressin et al. 2013), even the star closest to the sun, Proxima Centauri, is thought to have a planet (Anglada-Escudé et al. 2016).

Age determinations from our solar system imply that it takes millions of years for planets to form (see e.g. Trieloff 2009, and references therein) after the first solids, like calcium-aluminum-rich inclusions, have condensed (Amelin et al. 2002). Thus, even if we could observe a planet forming system up close, we would see only one small step of the whole formation process. Planet formation is a fascinating puzzle, which has to be solved using observations, simulations and laboratory experiments alike to explain the numerous processes that are involved in transforming micrometer-sized dust grains into planets with diameters of more than 100,000 km. This work will extend the knowledge about the sticking-bouncing transition for millimeter-sized dust aggregates, an important phase during the early growth process.

In Chapter 2 of this work, an overview of the current understanding of planet formation is given. First, the broad picture from the formation of the central star to the formation of the terrestrial planets is summarized, then the results of collisions between small dust aggregates are presented in more detail.

The forces governing the collisions between dust aggregates are presented in Chapter 3. Based on these forces, an equation of motion for the collision is derived. The results of this model are then compared to experiments to check the validity and scalability of the model.

Chapter 4 introduces the experimental setup MEDEA. It can be used in a microgravity environment to investigate collisions between dust aggregates with sizes of a few hundred micrometers to a few millimeters at velocities of around 1 $\mathrm{cm\,s^{-1}}$. This velocity range is of particular interest in early planet formation, as the results of collisions change here from sticking to bouncing. Growth models by Zsom et al. (2010, 2011) show that this transition is critical for the maximum size dust aggregates can grow to via collisions. The chapter also summarizes the performed experiments and gives an overview of the used samples.

In Chapter 5 the analysis method for experiments performed with the MEDEA setup is presented. It also includes a discussion about the relevance of rotational energy in the collisions, as well as about the influence of electro-static charges on the collisional results.

An analysis of one experiment using the methods given in the previous chapter is presented in Chapter 6. Following an evaluation of the velocity evolution during the experiment, a detailed comparison of the collision parameters using two- and three-dimensional data for the analysis is being made. Thereafter, the results of collisions are presented and brought into context of the current collision model. As a last aspect, the results of collisions of dimers with other aggregates and their implication for aggregate growth is discussed.

The results of this work are summarized in Chapter 7 and an outlook to future experiments and simulations is given.

2 Planet formation

Until the early 1990s, theories of planet formation concentrated exclusively on our own Solar System, as no planets outside of it were known. In 1992 the first exoplanets, i.e. planets outside of our Solar System, were discovered (Wolszczan and Frail 1992). They were orbiting a pulsar and formed a system completely unlike our Solar System.

In the meantime, many more planets have been found as the sensitivity of the detection methods increased. By now, more than 3400 exoplanet detections have been confirmed (NASA Exoplanet Archive, 11/15/2016). Two main conclusions can be drawn from these discoveries: *i)* Planetary systems are very common. Based on the data from the *Kepler* mission, Fressin et al. (2013) estimate that 52% of all stars have at least one planet orbiting it with an orbital period of less than 85 days. *ii)* Our solar system is not the norm. Planetary systems can have very different properties regarding the number, mass and distances of their planets.

Therefore, theories of planet formation have to explain an ubiquitous process that allows for diversity in the final properties of the planets and their orbits. In this chapter, the current paradigm of planet formation is summarized. An overview of the complete process is given in Section 2.1, followed by a more detailed introduction into the growth of dust aggregates, which is being investigated in this work, in Section 2.2.

2.1 An overview of planet formation

Planet formation is tightly coupled to the formation of the star of the system. In order for a star to form, a molecular cloud has to locally exceed the Jeans mass, leading to gravitational collapse. The required local density enhancements can be triggered by external sources such as supernovae. The collapse of the cloud leads to the formation of a protostar. Due to the rotation of the galaxy, molecular clouds have a certain angular momentum, which has to be conserved during the collapse. Therefore, material along the axis of rotation can freely fall unto the young star, while material perpendicular to it is prevented from doing so. This results in a disk-like structure around the protostar, called a protoplanetary disk (PPD, see Figure 2.1 a)). It is in these disks that planet formation occurs (see e.g. Dullemond et al. 2007, and references therein for details on the disk formation).

During the collapse the disk is heated by gravitational energy. As the collapse slows down, the disk is cooling, allowing for different materials to condense in certain distances from the star, such as metals, oxides, silicates, and ices. For the sake of simplicity, all solid materials within the disk will be referred to as dust hereafter, only ices may at times be called out individually.

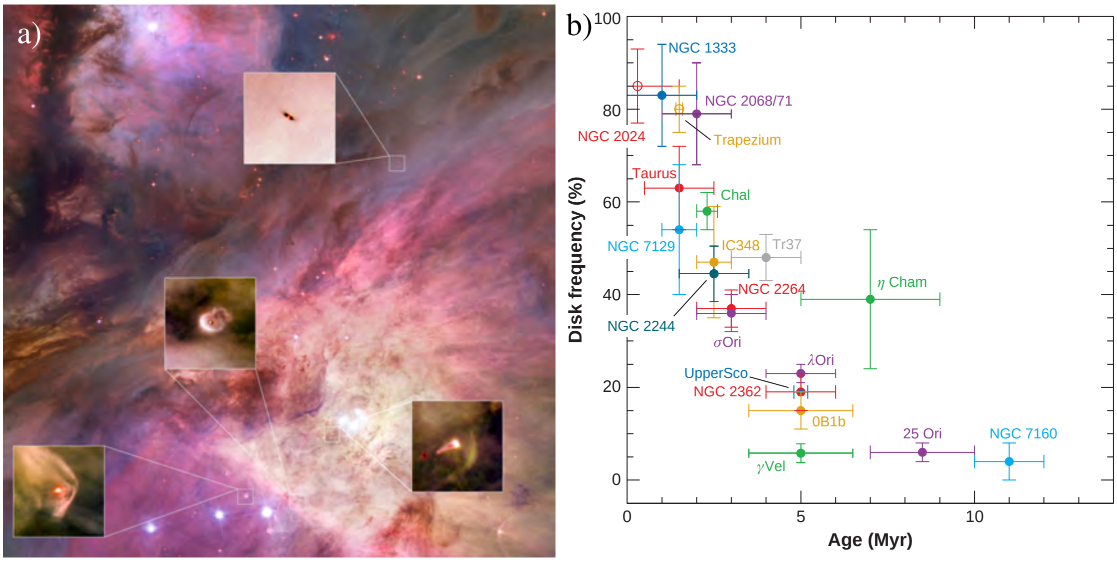

Figure 2.1: a) This figure shows a Hubble Space Telescope image of the Orion nebula. The insets are zoomed in pictures of protoplanetary disks around young stars found within the nebula. *Cropped from APOD091222, image credit: NASA, ESA, M. Robberto (STScI/ESA), the HST Orion Treasury Project Team, and L. Ricci (ESO)* b) The data give the percentage of sun-like stars that have a protoplanetary disk (based on infrared-excess) within different clusters of stars. After a few million years, most stars have no detectable PPD, indicating that it has dissipated by then. *Figure by Wyatt (2008), Evolution of Debris Disks, Annual Review of Astronomy & Astrophysics.*

The mass, composition, and distribution of the disk material, of the gas and the dust, are important parameters for planet formation. One of the most intuitive models is the Minimum-Mass Solar Nebula (MMSN) model by Weidenschilling (1977b). For the model, the mass of each planet is complemented by the addition of volatile gases until the elemental composition matches the solar one. Then, this mass is smeared out into a concentric ring reaching halfway to the neighboring planets, leading to different surface densities Σ at certain distances r from the star. These densities are then fitted by a power law, resulting in $\Sigma(r) \sim r^{-3/2}$. In a disk with such a surface density, the mass would be dominated by the outer region, matching the size of the planets in our solar system. The total mass of the disk is on the order of a few percent of the mass of the star.

However, other models show very different exponents for the power law. Andrews and Williams (2007) calculated the density based on submillimeter continuum survey observations of 24 different disks and found a vast range of exponents. Their median value is $\Sigma(r) \sim r^{-1/2}$, however, due to systematic errors and an oversimplified temperature profile, they claim a more realistic exponent to be in the range of -0.7 to -1. Desch (2007) used the same general principle as Weidenschilling, however, he did not use the position of the planets as we find them today. Instead, he used the starting positions found in the Nice model (e.g. Tsiganis et al. 2005), which initially places the giant planets much closer to the sun. This results in a steeper power law of the form $\Sigma(r) \sim r^{-2.168}$.

Another important factor for planet formation is the amount of solids (i.e. dust) in the disk and their size. The amount of solids is governed by the metallicity, which is usually given as the logarithm of the amount of iron compared to the amount of hydrogen relative to the solar ratio. For a metallicity similar to that of the Solar System, the mass ratio of dust to gas is about 1:100 (Lodders 2003).

The size of the dust depends on the condensation parameters. Their size can be estimated using the spectral slope of the opacity of PPDs, but this method has many free parameters. The Stardust mission has been measuring the sizes directly, finding monomers from a few nanometers to more than 10 μm (Brownlee et al. 2006). There, a spacecraft gathered dust in the coma of comet Wild 2 and returned the samples to earth. It is believed that material on a comet is mostly unaltered since its formation and still has its primordial size. Chondrites, a class of meteorites, have 0.1 - 1.5 μm-sized particles in their matrix (Scott and Krot 2005). Interplanetary dust particles collected in our solar system also show similar sizes of about 0.3 μm (Jessberger et al. 2001). Therefore, a monomer size of about 1 micrometer is commonly used for experiments.

An important constraint for planet formation models is the lifetime of the PPD. Once the disk vanishes due to photoevaporation from external sources of radiation and UV rays and solar winds from the central star, the remaining mass is not sufficient to form planets. Especially the cores of gas giants have to be formed before that, so they can accumulate the gas in their vicinity. Wyatt (2008) compiled several observations of clusters of stars (see Figure 2.1 b)), where the ratio of sun-like stars within the cluster that still have a disk was measured. It can be seen that most stars have lost their disk after a few million years. Therefore, models have to explain the formation of the cores of gas giants within about 10^6 years.

In the early stages of planet formation, when the dust particles are only micrometers in size, gravitational forces do not play a role. Instead, intermolecular forces, the van der Waals forces, determine whether or not a collision between dust particles will lead to aggregate growth (cf. Chapter 3). Collisions occur because the motion of the dust particles is influenced by the gas of the disk. The strength of the coupling to the gas is characterized by the Stokes number St, a dimensionless number. For small Stokes numbers (small particle sizes) the particles couple to the gas perfectly, while for higher Stokes numbers the inertia of the particles will dominate. The dust particles do not revolve around the star on perfectly stable orbits. Instead, depending on their Stokes number and position in the disk, several effects influence the motion and affect the orbit, which in turn may lead to collisions with other particles (see Figure 2.2).

The gas of the PPD is rotating at a sub-Keplerian speed. Due to a pressure gradient in the disk, the gravitational force of the star is compensated partly, leading to a speed less than Keplerian speed to keep the gas molecules on a stable orbit. The dust particles, on the other hand, do not feel the pressure gradient, but are slowed down by the gas nevertheless. Thus, they drift inward towards the star. The drift velocity is highest for particles with $St = 1$ (Weidenschilling 1977a).

For very small particles, Brownian motion is the most important source of relative velocites (Blum et al. 1996). This motion is the result of many gas molecules with Maxwellian velocity distribution colliding with the dust particle from random directions (Einstein 1905). For dust particle sizes up to a few micrometers, the resulting velocity is much larger than e.g. the drift velocity.

The gas in the disk is also not static, but undergoing turbulent motion. The velocity of the dust particles in turbulent regions depends on their Stokes number and the size of

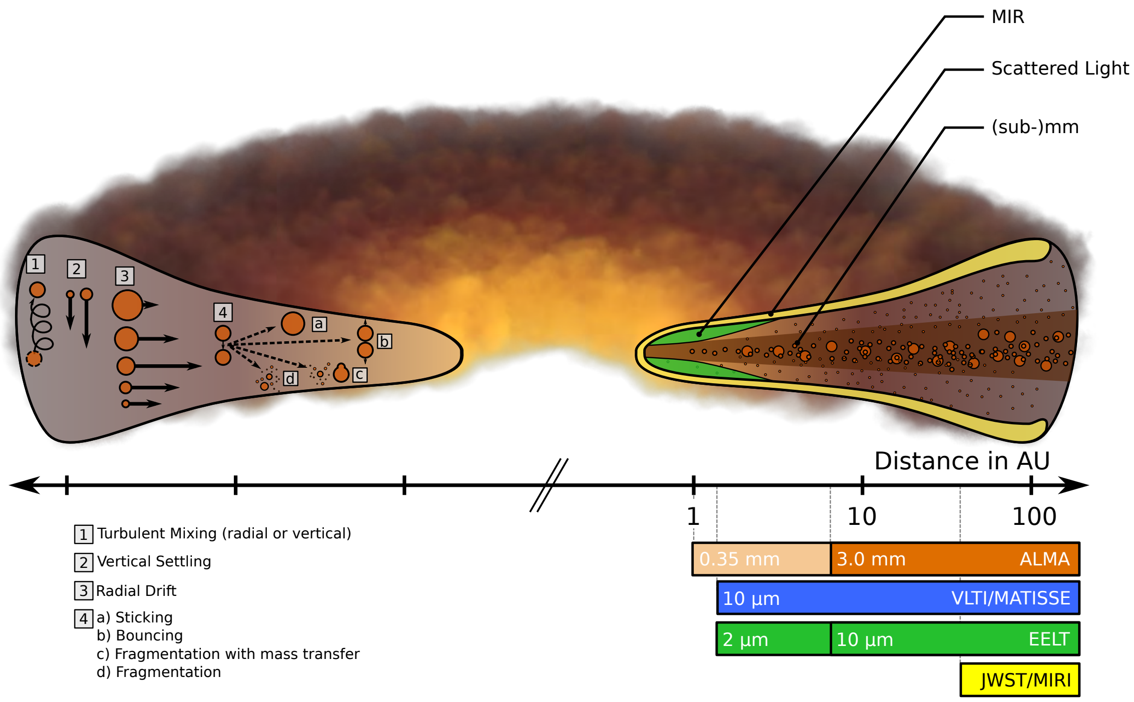

Figure 2.2: Schematic view of a protoplanetary disk from Testi et al. (2014). On the left-hand side different sources of relative velocities for dust and collision mechanisms are shown. The right-hand side of the scetch shows which wavelengths can be used to probe certain areas of a PPD and the instruments capable of detecting them. *From Protostars and Planets VI edited by Henrik Beuther, Ralf S. Klessen, Cornelis P. Dullemond, and Thomas Henning. © 2014 The Arizona Board of Regents. Reprinted by permission of the University of Arizona Press.*

the turbulent vortices. The strength of the turbulence is commonly denoted by the dimensionless parameter α, which is assumed to be between 10^{-2} and 10^{-4} in protoplanetary disks.

Dust particles that are not located in the midplane of the disk are subject to sedimentation. They drift towards the midplane of the disk because the gravitational force of the star has a vertical component, which is larger the further away from the midplane the particle is. However, particles do not all cluster at the exact midplane, as turbulence can push particles in the opposite direction, leading to an equilibrium between sedimentation and mixing.

Another source of aggregate motion is photophoresis, where particles are moving because of a temperature gradient induced by impinging sunlight (Matthews et al. 2016). However, the midplane of the disk is optically thick in the early phases, preventing most radiation to penetrate deeply. Thus, the effects of photophoresis are usually neglected in models. Loesche et al. (2016) propose to change that in future models, as temperature fluctuations due to thermal radiation within the disk can cause significant photophoretic velocities.

Combining these sources of relative velocities between dust aggregates with a model for the solar nebula yields typical collision velocities for particles of a given size. Weidenschilling and Cuzzi (1993) published the first results using this approach, which has been refined since then. Figure 2.3 shows a more recent model by Johansen et al. (2014), giving the isolines for the collision velocity in meters per second between two particles for a MMSN model at a distance of 1 AU from the star. It can be seen that particles of similar size collide at much lower velocities than differently sized particles. This is due to them experiencing almost identical forces. Millimeter-sized particles are shown to collide at velocities of a few centimeters per second. In the original calculations by Weidenschilling and Cuzzi (1993) these particles were predicted to collide at a few millimeters per second. The upper two panels of Figure 2.3 are for a stronger turbulence with $\alpha = 10^{-2}$ and the lower two panels for a weaker turbulence with $\alpha = 10^{-4}$. In the two panels on the right-hand side particles are allowed to be on eccentric orbits due to gravitational effects of gas density fluctuations due to turbulence. The strength of this effect is denoted by the parameter γ. The panels with the included gravitation effects show much higher collision velocities for aggregates larger than about 10 meters in diameter.

Utilizing this information it is now possible to conduct experiments colliding dust particles of appropriate size at velocities similar to those in a PPD or simulate these collisions numerically. While micrometer-sized monomers collide at very low velocities and always stick together at the point of contact (hit-and-stick), the collision velocities increase as the aggregates grow. With the increase in collision energy, eventually the aggregates do not stick to each other anymore, but bounce off, halting the growth through direct sticking collisions at about centimeter sizes (Zsom et al. 2010). A more detailed overview of this growth phase is given in Section 2.2.

In order for gravity to become important, the aggregates would need to reach sizes of about one kilometer, though. There are currently three theories as to how the growth from centimeter- to kilometer-sizes may occur:

I) One possible method of further growth are "lucky winners" among the dust aggregates. These are aggregates that happened to grow to larger sizes than the others by colliding at less than average velocities or extremely unlikely sticking events (Windmark et al. 2012a,b, Garaud et al. 2013). If these aggregates then collide with smaller ones, the small aggregates are destroyed, but a part of them sticks to the larger aggregate, which is gaining mass (mass transfer). The rest of the smaller aggregate fragments into very small sizes, which may subsequently be swept up by the large aggregates. However, as the collision velocities rise due to the large difference in size, erosion sets it (Schräpler and Blum 2011, Krijt et al. 2015).

II) Based on the work by Okuzumi et al. (2012), Kataoka et al. (2013) showed that aggregates can grow to kilometer sizes by direct sticking. In their simulations, water ice monomers with a diameter of 0.1 micrometers form very fluffy aggregates, with a volume filling factor as low as 10^{-5}. The volume filling factor ϕ is the ratio of the sum of the volumes of the monomers within an aggregate and the macroscopic volume of the aggregate. The large size at very low masses leads to low collision velocities as well as preventing the aggregates to reach a Stokes number of 1 and drift into the central star. However, for this to work, the monomers have to stick very well, e.g. by taking into account ice instead of dust and smaller monomers (see Chapter 3 for details). Due to the disk parameters, this method only works at distances from the central star significantly larger than 1 AU.

III) The third theory is a local accumulation of small dust aggregates until they gravi-

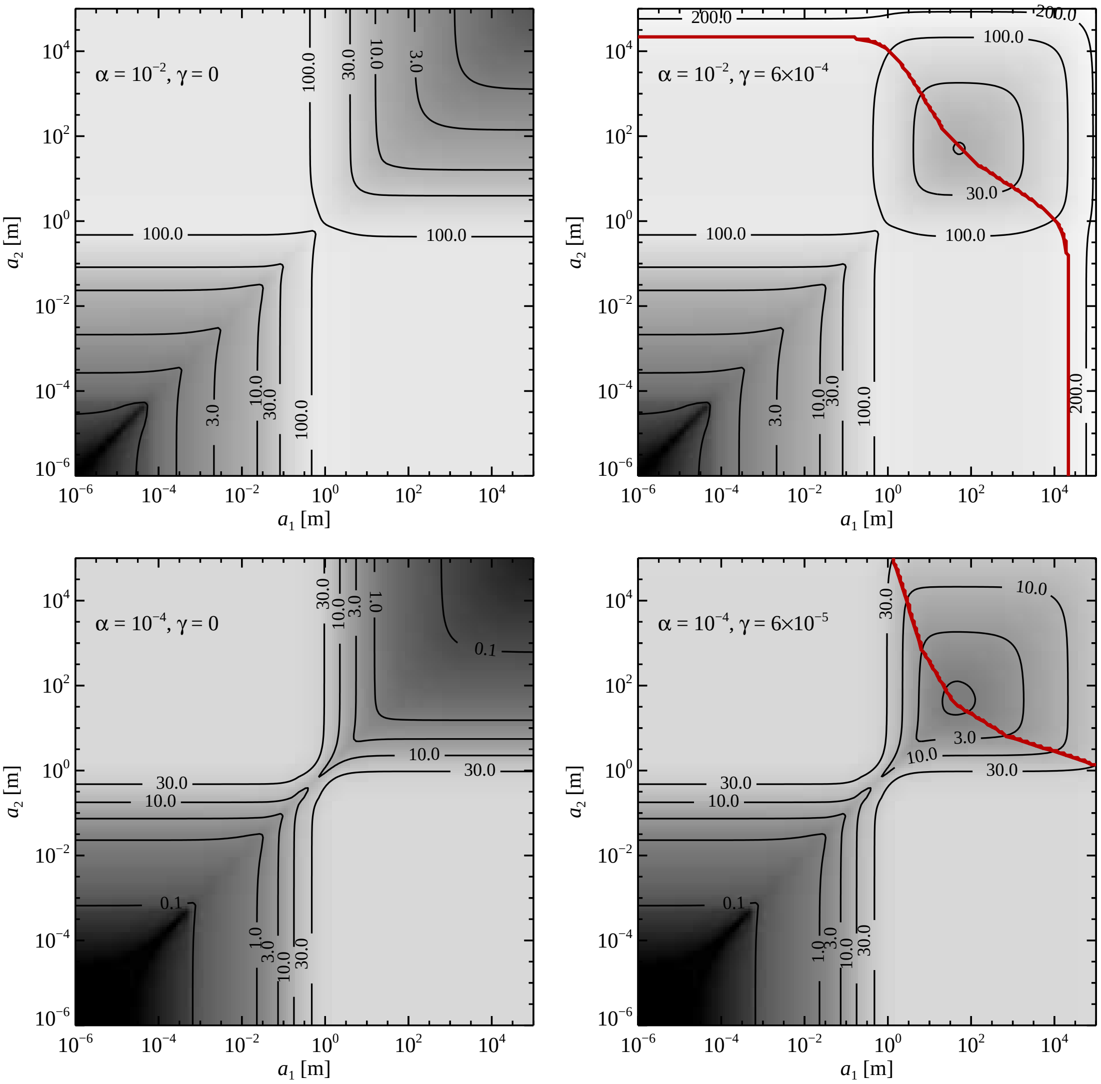

Figure 2.3: This figure from Johansen et al. (2014) shows the collision speed, in meters per second, between two dust aggregates of sizes a_1 and a_2 for an MMSN model at 1 AU. The sources of relative velocity are Brownian motion, differential drift and gas turbulence. The upper panels give the collision speeds for $\alpha = 10^{-2}$ and the lower panels for $\alpha = 10^{-4}$. The right-hand panels include the gravitational influence of turbulent gas density fluctuations. *From Protostars and Planets VI edited by Henrik Beuther, Ralf S. Klessen, Cornelis P. Dullemond, and Thomas Henning. © 2014 The Arizona Board of Regents. Reprinted by permission of the University of Arizona Press.*

tationally collapse by means of the streaming instability (e.g. Johansen et al. 2007, Youdin and Goodman 2005, Johansen and Youdin 2007). If dust aggregates concentrate locally, e.g. due to a pressure gradient or in turbulent vortices (Johansen et al. 2014, Figure 6), the local dust-to-gas ratio rises. The more dust is present, the more it does affect the surrounding gas, triggering the streaming instability. This forces the surrounding gas to a velocity closer to Keplerian velocity. Thus, the clump catches up with the slower dust on the same orbit and has a reduced radial drift, allowing for accumulation of inward-drifting dust.

This can lead to massively increased dust-to-gas ratios of up to 100. While the Kelvin-Helmholtz instability may cause the clumps to fracture, the high dust densities can trigger local gravitational collapse, forming bodies of several hundred kilometers in size from a large number of much smaller aggregates. These kilometer-sized bodies are called planetesimals, a term created from the two words *planet* and *infinitesimal*, designating a very small fraction of a planet.

The passive enhancement of the density and the resulting streaming instability are most efficient for a Stokes number of $St = 1$. Bai and Stone (2010) and Carrera et al. (2015) find that the streaming instability can be triggered by particles with Stokes numbers as low as $St = 10^{-2}$, corresponding to much smaller particles of about centimeter size, which may form more readily by collisional mechanisms, especially outside of the snowline (Drążkowska and Dullemond 2014). The snowline marks the distance from the star at which it is cold enough for water ice to condense, which increases the amount of solids in this region. Another important factor is the metallicity of the PPD, which in this context gives the mass of solid materials in the disk compared to the mass of the gas. Enhancing the canonic ratio of 1:100 by only a factor of 2 increases the efficiency of the streaming instability dramatically (Johansen et al. 2009).

While the exact parameters at which the streaming instability is triggered and the biggest size the dust aggregates can grow to through collisions are still subject to further investigation, this theory currently seems to be the most promising to explain this step of planet formation. Evidence may be found in comets, which are thought to be mostly unaltered since their formation. Skorov and Blum (2012) showed that cometary activity can only be explained for a low tensile strength of the surface material. They calculated the tensile strength from a gravitational collapse to be around 1 Pa and were able to confirm this experimentally (Blum et al. 2014). Theory *I* would form much more compact bodies with a higher strength. As of now it is unclear which level of tensile strength a body formed by theory *II* would have, but theory *III* can result in bodies with a tensile strength as low as this.

The gravitational force of these planetesimals is large enough to significantly increase their collisional cross section and influence bodies on nearby orbits. At this size, the influence of the surrounding gas is low and is usually neglected.

The collision velocities between planetesimals are significantly higher than for the micrometer-sized monomers, on the order of kilometers per second, frequently leading to fragmentation of the bodies. However, it is possible for these bodies to reaccrete matter through gravitation, if the fragments move away with less than escape velocity. During this phase, runaway growth sets in, letting the already biggest planetesimals grow much faster than the smaller ones (Greenberg et al. 1978). At the end of this oligarchic growth phase, a small number of very large bodies emerge that have reached Moon- to Mars-size and are called planetary embryos (e.g. Kokubo and Ida 1998, 2000, 2012). Simultaneously, lots of planetesimals are still present in the disk.

Beyond the snowline, the embryos grow even more rapidly and to larger sizes (e.g. Kokubo and Ida 2002, Morbidelli et al. 2008). This allows for large planetary cores of about 10 Earth masses to form that accrete the gas of the disk to eventually become the gas and ice giants of our Solar System. The formation of these planets has to be finished by the time the gas of the disk is dissipated.

Further inwards, in the region of the terrestrial planets, collisions are less frequent due to less condensed material being available, leading to slower growth. Once the giant planets have formed, however, especially the mass of Jupiter leads to a significant disturbance of the planetesimals and embryos further in. Several simulations - dubbed the Nice model and The Grand Tack - show that a 2:1 resonance of Jupiter and Saturn due to migration leads to an even larger disturbance that can explain many features of the solar system like the number, mass distribution and formation timescale of the terrestrial planets, the likelihood of Moon-forming events, the mass of the asteroid belt or the occurrence of the late heavy bombardment (e.g. Tsiganis et al. 2005, O'Brien et al. 2006, Raymond et al. 2009, Walsh et al. 2011, 2012). In this phase, the orbital parameters of all planets can shift significantly, potentially placing planets in a position far away from the region where they were formed.

Nearly all phases of planet formation are still subject to current research. One of the biggest open questions is the formation mechanism of planetesimals. Depending on the nature of the formation mechanism, they can have vastly different initial masses as well as different formation timescales, both of which have implications for the later stages of planet formation. On the other hand, the direct interaction of dust aggregates in mutual collisions governs which formation theory is the most likely. Therefore, it is of great interest to investigate collisions of dust aggregates in simulations and in the laboratory.

2.2 Growth processes of dust aggregates

Laboratory experiments are important for the understanding of the earliest phases of planet formation. The relevant collision velocities can be taken from models of the solar nebula and its interaction with the dust aggregates, for example the one from Johansen et al. (2014) presented above. As the predicted relative velocities vary with the used models and distances from the star, most experiments are carried out for a range of velocities.

It is very time-consuming and sometimes difficult to repeat all experiments with different kinds of monomers, as these could vary in material, shape and size. Poppe et al. (2000a) performed impact experiments of various monomers onto a target and determined their sticking probability based on the impact velocity. They found that the material properties are not as relevant for the stickiness of a monomer as the shape and size.

Most experiments presented hereafter were carried out with silica (SiO_2) particles. While not abundant in the PPD, especially when compared to silicates (Gail 2004), its collisional properties are comparable and it can be easily obtained and used in the laboratory. SiO_2 also is a non-magnetic isolator. Experiments for example by Nuth et al. (1994), Dominik and Nübold (2002), and Nübold et al. (2003) showed that magnetism can enhance the sticking probabilities of aggregates, but it is unclear to what extend the dust in the PPD is magnetized. Also, magnetism most strongly increases the collisional cross section at low velocities and becomes less relevant with increasing relative velocities. While triboelectric charges can accumulate on the silicate particles (Poppe et al. 2000b) and large charges can influence the result of collisions (Matthews et al. 2012), their influence is likely constrained to a yet unknown part of the disk (Okuzumi et al. 2011). In Section 5.2 it will be shown that electric charges do not influence the results found in this work. The main force between silica particles is caused by dipole interaction. The resulting van der Waals force is explained in more detail in Chapter 3.

The silica particles used in the experiments are either perfect spheres with a monodisperse size distribution or irregular particles with a polydisperse distribution. For the spheres, diameters between 0.5 and 1.9 μm have been used. The irregular particles have diameters ranging from 0.1 to 10 μm, a size distribution can be found in Kothe et al. (2013, their figure 3). The used sizes are well within the range of expected sizes of monomers in the PPD. While monodisperse spheres are not representative for the dust in a PPD, they are convenient for simulations and provide an excellent means of comparison between experiments and numerical work.

In the collision experiments with different monomers, Poppe et al. (2000a) found that silica spheres stick to a larger target up to velocities of about 1 $\mathrm{m\,s^{-1}}$. Experiments by Wurm and Blum (1998), Blum et al. (1998, 2000, 2002), and Krause and Blum (2004) showed that when the monomers collide with each other at low velocities, very open fractal-like structures emerge. The dust aggregates stick to each other perfectly at the point and angle of impact. This is the so-called hit-and-stick regime, which had been predicted earlier by Dominik and Tielens (1997). This process also leads to a very narrow or even monodisperse size distribution of the dust aggregates (Blum 2006).

While the expected collision velocities do not rise by much for small aggregates, their increased mass also means an increase in impact energy. Dominik and Tielens (1997) already predicted that once the impact energy surpasses 5 times the energy to overcome rolling friction, the aggregates would still stick together, but restructuring of the aggregate would start. Blum and Wurm (2000) were able to confirm aggregate restructuring experimentally, while Wada et al. (2007) presented n-particle simulations also showing more compact aggregates as the collision energy increased.

For millimeter-sized aggregates the predicted collisions speeds are on the order of a few millimeters to several centimeters per second. Blum and Münch (1993) showed that colliding aggregates of this size made out of $ZrSiO_4$ and Aerosil bounce off each other at velocities of 0.1 to 1 $\mathrm{m\,s^{-1}}$, which was confirmed later for SiO_2 aggregates by Heißelmann et al. (2007). Both observed coefficients of restitution, i.e. the ratio of the relative velocity after the collision compared to the velocity before the collision, of much less than 1. This loss of kinetic energy was attributed to plastic deformation of the aggregates during the collision. Weidling et al. (2009) showed that the dust aggregates are indeed being compacted in bouncing collisions, up to a volume filling factor ϕ of about 0.37.

At velocities above 1 $\mathrm{m\,s^{-1}}$, Blum and Münch (1993) observed fragmentation of the millimeter-sized aggregates, i.e. at least one of the aggregates broke into smaller fragments. Lammel (2008) also observed fragmentation at velocities of a few meters per second, both for compacted ($\phi = 0.35$) and more porous ($\phi = 0.15$) SiO_2 aggregates.

If the two colliding aggregates happen to have drastically different masses, the above results may be altered. Teiser and Wurm (2009) performed experiments where millimeter-sized aggregates collided with very large targets at velocities up to 60 $\mathrm{m\,s^{-1}}$. While the aggregates fragmented in the collision, a small part stuck to the target, leading to growth. The same result had been observed earlier by Wurm et al. (2005b), who found bouncing of the small aggregate up to 13 $\mathrm{m\,s^{-1}}$, and fragmentation with part of the aggregate sticking to the target at higher velocites. This process is called sticking by mass transfer to indicate net growth of the larger body, although the smaller one is fragmenting.

If the impacting particle is very small and only consists of a monomer or a few monomers, it can erode larger aggregates. While the impacting particle usually sticks to the target, some other monomers with a total mass larger than the projectile are lost. This means that the target loses mass (Schräpler and Blum 2011). The same effect can be observed for larger projectiles that are either more compact or have very high collision velocities. They fragment at impact and part of their mass sticks to the target. However, the impact also leads to the formation of a crater, where more mass is lost than is being deposited by the remains of the projectile (Wurm et al. 2005a, Paraskov et al. 2007).

Güttler et al. (2010) were the first to characterize the wealth of experiments and categorize the different outcomes of the collisions. They distinguished between four different kinds of sticking or net growth (hit-and-stick, sticking through surface effects, sticking through penetration, and mass transfer), two kinds of bouncing or neutral growth (bouncing with compaction and bouncing with mass transfer, where the larger target loses a small amount of mass to the projectile), and three types of fragmentation or mass loss (fragmentation, erosion, and fragmentation with mass transfer). They also divided the collisions into eight categories by distinguishing between collisions among aggregates with roughly identical masses and those where one collision partner was more than 100 times as massive as the other one and by discriminating porous and compact aggregates, where the latter are aggregates with a volume filling factor of $\phi > 0.4$.

For each of the eight possible combinations of collision partners they then used the results found in previous experiments to determine which combination of aggregate mass and collision velocity yields what kind of collisional result. Where no experiments had been performed at that time, available results were extrapolated or simple scaling laws derived. In most of the eight categories a similar picture emerged. At low collision velocities and for low masses, i.e. for low collision energies, the aggregates stuck to each other. At higher masses and higher velocities, bouncing was observed, with a small transition regime in between, where both sticking and bouncing can occur with a certain probability. At velocities above 1 $\mathrm{m\,s^{-1}}$, fragmentation was observed.

This model containing the outcome of collisions was then used by Zsom et al. (2010) in a Monte Carlo based growth simulation. They simulated the evolution of an ensemble of monomers at a static location with a distance of 1 AU from the star. Collisions among dust particles happened based on a probability weighted with the collisional cross section and the number density. For the chosen aggregates the collision velocity was taken from one of three different disk models. The outcome was based on the model by Güttler et al. (2010). Zsom et al. (2010) found that the dust initially grows monotonically, while at the same time the aggregates become more and more porous, i.e. their volume filling factor becomes lower. However, once the aggregates are massive enough to bounce off each other, growth stalls. The aggregates are compacted in the bouncing collisions, but can not grow any further. This phenomenon, where the largest dust aggregates reached masses of only a few grams in the MMSN model, was called bouncing barrier.

The simulations also revealed a need for improvement of the collision model. Figure 2.4 shows the color-coded number of collisions per grid cell of the simulation for the MMSN model. The eight boxes represent the different combinations of aggregate mass ratio and compactness, while the solid white lines give the borders between different collision outcomes. The dashed and dotted gray boxes mark the part of the parameter space where experiments had been performed at that time. It can be seen that the results of most collisions in the simulation were based on extrapolations or scaling laws instead of experimental data. In the top left panel, where porous aggregates of about the same mass collide, it can be seen that the aggregates cross the boundary from sticking to bouncing with masses of 10^{-9} to 10^{-7} kg, which correlates to about millimeter-sized aggregates. In the MMSN model, these collide at velocities of around one millimeter per second. The transition from sticking to bouncing turned out to be a crucial stage in the early planet formation and is the focus of the experimental setup MEDEA presented in this work.

Following up on the previous simulations, Zsom et al. (2011) followed the growth of a population of monomers in a vertical 1D column in the disk. They found that the dust aggregates reach masses of only 10^{-5} kg. Further growth was again stopped by bouncing. A major difference in this model was the presence of micrometer-sized dust, i.e. monomers, in the upper layers of the disk, a feature that has been observed in the spectral energy distributions (SEDs) of several PPDs (Pinte et al. 2007). However, Dullemond and Dominik (2008) argue that this feature may be an artificial effect of choosing bimodal size distributions when modeling the SED.

Following the collision model and growth simulations, numerous experiments and simulations have been conducted in order to substantiate previously extrapolated parameter spaces with data or to find alternative ways of growth. Kothe et al. (2010), Teiser et al. (2011), Meisner et al. (2013), Deckers and Teiser (2014), and Bukhari Syed et al. (accepted) studied the efficiency of mass transfer in collisions of small aggregates with larger targets. Theory *II* for the formation of planetesimals (presented above, Windmark et al. 2012a,b, Garaud et al. 2013) was founded on these results.

Beitz et al. (2011) showed that the fragmentation of aggregates occurs at velocities of less than 1 $\mathrm{m\,s^{-1}}$ for aggregates of centimeter size. The experiments by Schräpler et al. (2012), Deckers and Teiser (2014) and Bukhari Syed et al. (accepted) also determined the onset of fragmentation, but for different sizes of the dust agglomerates. Additionally, they measured the size distribution of the fragments in the collisions. Wada et al. (2013) showed that the efficiency of the fragmentation also depends on the impact parameter.

Fragmentation or collisions with mass transfer always produce monomers and small aggregates consisting of just a few dimers. If these collide with larger aggregates, they can erode these (Schräpler and Blum 2011, Krijt et al. 2015). Teiser and Wurm (2009) showed that the eroded mass is not always lost, but may be reaccreted by the larger body in a secondary collision caused by the increased headwind the eroded particles are experiencing compared to the large target.

Several experiments with the MEDEA setup presented in this work have been aimed at a better understanding of the transition from sticking to bouncing. In Weidling et al. (2012), the width of the transition zone was found to be broader than in the model by Güttler et al. (2010) and Kothe et al. (2013) found the slope of the power law to differ as well. Brisset et al. (2016) used a smaller, but similar setup to investigate aggregates a few hundred micrometers in diameter in a sounding rocket experiment. They were able to deduce the maximum velocity at which aggregates always stick to each other as well as a velocity where the sticking probability was less than 5%.

Kelling et al. (2014) and Kruss et al. (2016) investigated the results of collisions at velocities where the sticking probability was low. Their experimental results support the existence of a bouncing barrier. In their experiments, all clusters of aggregates formed in sticking events were broken up again in subsequent collisions, leading to no net growth. Jankowski et al. (2012) performed similar experiments with basalt aggregates, which were made up of larger monomers and had a high filling factor of about 0.5. They ob-

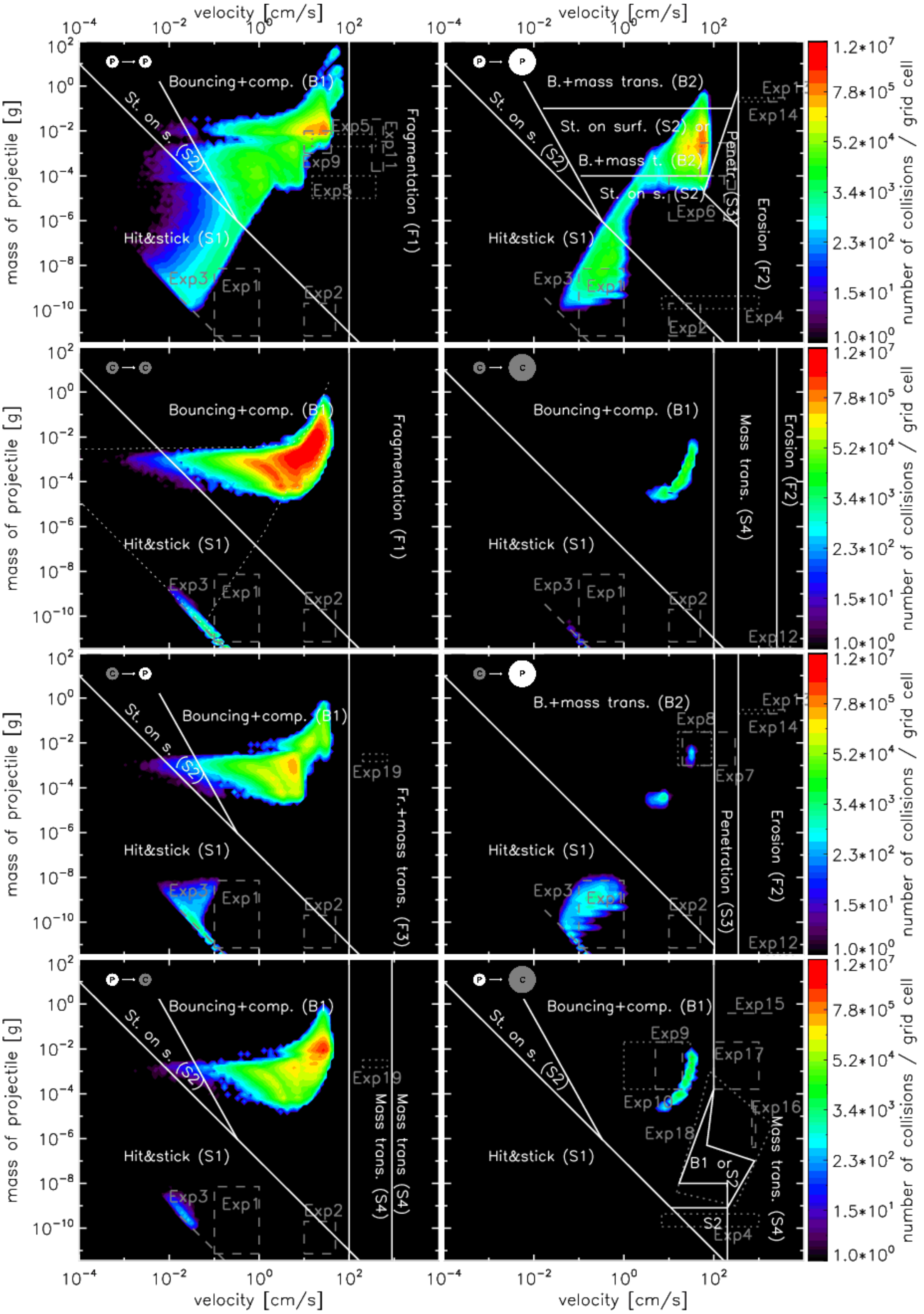

Figure 2.4: The colors indicate which collisions occur most frequently in an MMSN model at 1 AU when simulating the evolution of an ensemble of monomers based on the collision model by Güttler et al. (2010). The panels on the left show that many collisions happen at the transition from sticking to bouncing. *Figure by Zsom et al., A&A, Volume 513, A57, 2010, reproduced with permission © ESO.*

served more sticking collisions than the other experiments, but were not able to determine whether some clusters of aggregates might grow much bigger than millimeter-size or if they are destroyed in subsequent collisions.

While *n*-particle simulations of collisions previously resulted in either sticking or fragmentation, Wada et al. (2011) were able to reproduce bouncing collisions. However, they do not find bouncing for filling factors of less than 0.3. They require high contact numbers for the monomers for the energy to be dissipated efficiently.

Kothe (2016) has updated the collision model by Güttler et al. (2010) to include all of the results found in the meantime. However, to date no growth model that includes the change of the slope and width of the sticking-bouncing transition zone, a slope in the fragmentation velocity, growth through mass transfer, and erosion has been published. Thus, it is not clear yet whether the resulting dust aggregates can grow larger than predicted by Zsom et al. (2010) or not. It is likely that erosion will weaken or even compensate for the positive effects of collisions with mass transfer due to the amount of monomers created in them.

If the final aggregate size in future growth simulations turns out to be smaller than in those by Zsom et al., it is likely that planetesimals cannot be formed by micrometer-sized silicate monomers alone. In this case, smaller monomers or different materials like organics or ices may play a crucial role even at a solar distance of 1 AU. Therefore, the results of such a model would help in focussing future experimental efforts on parameter combinations that are relevant for the PPD.

3 Surface forces of dust aggregates

The early stages of planet formation are not governed by long-ranged effects like gravity, but rather by the microphysics of the interaction of single dust grains or the forces acting in the collision between two aggregates. While there are a lot of models describing the physics of the collision between two solid spheres, some of which are presented in Section 3.1, no analytical model exists that treats collisions of porous aggregates such as the dust aggregates present in a protoplanetary disk. In Section 3.2, a simple equation of motion is derived that can describe collisions between dust aggregates. The results are presented in Section 3.3 and compared to experimental data.

3.1 Contact theory

The growth of dust aggregates is governed by the forces acting between the aggregates. For silicates, which make up the main group of material during planet formation in a terrestrial distance from the star and the only material used for the experiments and calculations discussed in this work, the most important binding force is the van der Waals force. It is an intermolecular force that combines all attractive or repulsive effects between molecules that are not caused by direct electrostatic interaction or covalent bonds, but by induced dipoles.

The first efforts of quantifying the contact mechanics between two elastic bodies with a curved surface were made by Heinrich Hertz (1881). Hertz developed equations to calculate the shape of the contact area and the distribution of the pressure therein. He assumed that the bodies are much larger than the contact area and that pressure is only exerted along the axis connecting the two bodies. For spherical bodies, the contact area becomes a circle with radius

$$a_{\mathrm{Hertz}}^3 = \frac{3FR}{4E}, \tag{3.1}$$

where F is the force pressing one sphere onto the other, $R = r_1 r_2/(r_1 + r_2)$ is the reduced radius of the spheres with r_1 and r_2 being the radii of the individual spheres and E is Young's modulus, respectively. Since the spheres may consist of different materials, it is calculated based on the elastic constants of both bodies in contact:

$$E = \left(\frac{1 - \nu_1^2}{E_1} + \frac{1 - \nu_2^2}{E_2} \right)^{-1}. \tag{3.2}$$

Here, E_1 and E_2 are the Young's moduli of the two spheres and ν_1 and ν_2 are Poisson's ratios, respectively. The indentation δ of the two bodies, the distance that two distant points within the spheres approach each other due to the external force, is given by

$$\delta^3 = \frac{9F^2}{16RE^2}. \tag{3.3}$$

However, Hertz's theory is valid only for two bodies that are pressed together with a certain force, since there are no attractive forces between the two bodies. Experiments with rubber and glass spheres showed that the above equations deviate significantly from the observed values at low loads in showing finite values for the area of contact and the indentation for zero load. This effect was attributed to adhesion between the two bodies, which provides a finite attractive force between them. Therefore, Johnson et al. (1971) expanded Hertz's theory to account for the effect of adhesion by introducing the specific surface energy γ. The surface energy is a measure for the amount of adhesion between the bodies, which is assumed to only be effective within the contact area. Their model for the contact mechanics of small and soft bodies has come to be known as JKR theory, named after its authors.

More precisely, the specific surface energy γ of a material is the amount of energy per unit area that is necessary to create new surface, i.e. to break up intermolecular bonds between two bodies touching each other. Differentiating the total energy in the contact with respect to the movement of the spheres relative to each other yields an approximation for the force necessary to separate the two bodies. Since the distribution of the stress within the area of contact changes with the indentation, δ and the real indentation are not exactly identical.

A more exact calculation utilizes a different load-displacement relation found in experiments by Johnson (1958). This yields a modified equation for the radius of the contact area, which simplifies to

$$a^3 = \frac{9\pi\gamma R^2}{2E} \tag{3.4}$$

if no external force is applied to the spheres (Johnson et al. 1971, their equation 20). Here, γ is the sum of the specific surface energies of the two materials in contact. Applying a negative force until the contact radius vanishes yields a criterion for the force necessary for the separation of the spheres:

$$F = -\frac{3}{2}\gamma\pi R. \tag{3.5}$$

Since γ is the combined surface energy of the two bodies, adding up the two surface energies means that for two bodies made of the same material, a factor of 2 has to be applied to the surface energy of the material.

A slightly different approach was used by Derjaguin et al. (1975) who allow for adhesive forces outside the contact area and a different distribution of the pressure within the contact area. This model, which has come to be known as the DMT model, is more suited to describe the behavior of large and hard materials, i.e. those with a small surface energy. However, the dependencies of the major parameters are identical to the JKR model and only differ in the prefactor. Here, for the separation of two particles a force of $-2\gamma\pi R$ is necessary. The difference between the two theories is rather small.

Tabor (1977) showed that both theories are extreme cases of a general theory and introduced a parameter to determine which one is valid in a special situation. The parameter compares the size of the neck of the contact zone with the equilibrium distance of atoms and is defined as

$$T = \frac{R\gamma^2}{E^2 z^3}, \tag{3.6}$$

where $z = 0.2...0.4$ nm is the spacing between atoms. For aggregates with a radius of 1 mm, a specific surface energy of 0.037 J/m^2 (Heim et al. 1999) and a Young's modulus of 8100 Pa (see below), T is on the order of 10^5. This means that the neck region is much larger than the distance between atoms and forces outside of the contact area can be neglected. Therefore, JKR theory is used in this work.

Thornton and Ning (1998) expanded upon the JKR theory by adding the possibility of plastic deformation. Once a certain yield pressure is exceeded within a body, the internal structure of that region is changed irreversibly. The plastic deformation dissipates energy. The yield velocity v_y is associated with the yield pressure. It is the impact velocity above which plastic deformation occurs (Thornton and Ning 1998, their equation 10):

$$v_\mathrm{y} = 3.2 \sqrt{\frac{p_\mathrm{y}^5 R^3}{E^4 M}}. \tag{3.7}$$

Here, $1/M = 1/m_1 + 1/m_2$ is the reduced mass of the two spheres of mass m_1 and m_2. For solid particles, the mass is the product of the particles' volume V and density ϱ, for aggregates, the volume filling factor ϕ has to be taken into account:

$$m = \frac{4}{3}\pi r^3 \varrho \phi. \tag{3.8}$$

The volume filling factor ϕ denotes the ratio of the aggregate volume that is filled with solid monomers. Thornton and Ning (1998) also find an equation for the sticking velocity, which defines the maximum collision velocity of two spheres at which they will stick to each other (their equation 54):

$$v_\mathrm{s} = 3.77 \left(\frac{\gamma^5 R^4}{M^3 E^2} \right)^{1/6} \tag{3.9}$$

Combining the force-displacement relationships with Newton's laws of motion allowed Thornton and Ning to predict the coefficient of restitution ε, the ratio of the relative velocity after and before the collision, depending on the collision velocity. Since these are much easier to find experimentally for the dust aggregates than the contact area, they can be used to obtain material parameters. Three equations are used to describe the curve for the coefficient of restitution. For collision velocities lower than the sticking velocity, the spheres stick to each other due to adhesion and ε is 0. For higher velocities the equations are a little more complex and depend on the yield and sticking velocities as well as on the collision velocity (Thornton and Ning 1998, their equations 80 and 81). They describe a rise of ε to a maximum at or below a value of 1 and a subsequent monotone decrease due to energy dissipation by plastic deformation.

While in experiments, such as those described in detail in Chapter 4, collisions occur with random impact parameters the theories outlined above are valid for central collisions of spheres only. Another difference to the experiments presented in this work is that the spheres are assumed to be completely homogeneous instead of being porous aggregates. Nevertheless, a fit of ε (equation 81 by Thornton and Ning 1998) to experimental data of the coefficient of restitution did yield plausible results (Weidling et al. 2012). The yield velocity found in this case was $v_{\mathrm{y}} = 0.9^{+1.8}_{-0.6}\ \mathrm{mm\,s^{-1}}$. Although the error margin is quite large, the value compares very well with the maximum velocity for hit-and-stick as defined by Güttler et al. (2010, their equation 7) following Dominik and Tielens (1997), which also denotes a velocity at which restructuring sets in. Using their approach, a velocity of $0.2\ \mathrm{mm\,s^{-1}}$ is found for aggregates with a diameter of 1 mm consisting of monomers with a diameter of 1 μm.

The fitted yield velocity and known aggregate dimensions and yield pressure give a value of $E = 8100$ Pa for Young's modulus of the dust aggregates. However, no experimental data was available for velocities lower than the yield velocity. Therefore, the sticking velocity could not be determined by a fit. Using Equation 3.9 with the above value for E and the specific surface energy measured by Heim et al. (1999) would yield an unrealistically high value of almost $0.1\ \mathrm{m\,s^{-1}}$, where the aggregates in the experiment clearly bounced off each other.

More realistic values for the sticking velocity can be obtained by modifying the theory of Thornton and Ning to take into account the specific properties of dust aggregates. The most convenient way to account for these is by modifying the surface energy into an effective surface energy γ_{eff}. It accounts for the effect of a reduced contact area, as an aggregate does not have a flat surface, but one made up of monomers. With the specific surface energy denoting the amount of energy per surface area, it makes no difference for the calculations whether the reduction is included in the term for the contact area or in the term denoting the surface energy.

The reduction of the contact area is a function of the volume filling factor. Here, it is assumed that the share of the surface area which is filled with monomers can be approximated by the volume filling factor ϕ. In a first step, the specific surface energy is multiplied with this factor. However, with $\phi = 0.35$ the sticking velocity obtained with Equation 3.9 would still be of the order of centimeters per second. The growth model by Güttler et al. (2010) suggests that this is the sticking velocity for aggregates with a diameter of less than 100 μm and, thus, unrealistic for millimeter-sized aggregates.

As an estimate on the smallest possible contact area the Hertz factor is introduced. It gives the ratio of the contact area of two monomers in contact by adhesion to their cross section. Here, it is assumed that the monomers can be approximated as spheres with a characteristic diameter, even if the experiments were conducted with polydisperse, irregular dust particles. Additionally, it is assumed that the size of the contact area between two monomers is determined by the properties of the monomers and not of the aggregate. Thus, the monomers will have a contact area smaller than their cross section. The ratio can be determined by using Equation 3.4 and substituting the material parameters of one monomer instead for those of the pair:

$$\frac{\pi a^2}{\pi r_{\mathrm{m}}^2} = \frac{a^2}{r_{\mathrm{m}}^2} = \left(\frac{9\pi\gamma(1-\nu^2)}{4E_{\mathrm{m}}r_{\mathrm{m}}}\right)^{2/3} \tag{3.10}$$

with r_{m} and E_{m} being the radius and Young's modulus of a monomer and a being the contact radius of this monomer, respectively. It should be noted that Young's modulus of a monomer is identical to that of the bulk material, while it is reduced significantly for aggregates. For monomers with a radius of $r_\mathrm{m} = 0.5\,\mu$m made of $\mathrm{SiO_2}$ with $\gamma = 0.037$ J/m^2 (Heim et al. 1999, Gundlach et al. 2011, twice the given value is taken since two identical surfaces are in contact here), $E_\mathrm{m} = 72.1$ GPa and $\nu = 0.18$ (Clark 1966, p.173) this amounts to $a^2/r_\mathrm{m}^2 = 3.7 \cdot 10^{-4}$. It should be noted that the equation given here deviates from that derived in Weidling et al. (2012) by a factor of 4 and that the value for Young's modulus is different as well.

Combining these two concepts gives an equation for the effective surface energy:

$$\gamma_\mathrm{eff} = \gamma \cdot \phi \cdot \frac{a^2}{r_\mathrm{m}^2}. \tag{3.11}$$

This is the smallest possible contact area of two aggregates, where the contact forces are reduced by a factor of $1.3 \cdot 10^{-4}$ compared to that of two solid spheres. It leads to a reduction of the calculated sticking velocity to about 0.01 mm s^{-1}. This value seems to be too low to be realistic, but gives a lower boundary for the sticking velocity. Deformation of the aggregates upon collision will lead to an increase of the contact area due to interlocking of monomers. However, the contact area will only increase by a factor of a few, which leaves the effective surface energy to remain several orders of magnitude lower than the value for the solid material.

The effect of the effective surface energy is quite severe. An aggregate with radius r_agg has to be many orders of magnitude larger in size than the monomers (i.e. solid spheres) of radius r_m it consists of in order to have an identical adhesive van der Waals force. Combining Equations 3.5, 3.10 and 3.11 yields

$$r_\mathrm{agg} = 1.2 \cdot 10^8 \cdot \frac{1}{\mathrm{m}^{2/3}} \cdot r_\mathrm{m}^{5/3}. \tag{3.12}$$

Two monomers with a radius of $0.5\,\mu$m are therefore attracted by a van der Waals force identical to that between two aggregates with a radius of 3.9 millimeters. Since at least two monomers must be in contact in a collision, this could lead to a step-wise increase in the contact energy between two aggregates. In this scenario, very small aggregates would have a much larger relative contact energy than millimeter-sized aggregates.

The expression for the effective surface energy obtained here can not only be used to investigate the sticking behavior of dust aggregates. Skorov and Blum (2012) applied the same scaling to the tensile strength of aggregates, since this scales with the surface energy as well. Doing so allowed them to calculate the force necessary to remove aggregates from the surface of a comet.

Although the effective surface energy obtained in Equation 3.11 may be a little too low for collisions at velocities of centimeters per second – which is faster than the yield velocity and should lead to compression of the aggregates and, therefore, to an increase in the number of contacts – it can still be used to investigate collisions at velocities closer to the yield velocity. Since the sticking velocity decreases with increasing aggregate radius, it is experimentally challenging or even impossible to verify this for aggregates larger than a few millimeters. Collisions among these aggregates have to be studied in numerical simulations. The most common methods used in this context are molecular dynamics (MD) and smoothed-particle hydrodynamics (SPH) simulations.

MD simulations solve the equations of motion for every single monomer that an aggregate consists of and are also referred to as *n*-particle simulations. Seizinger et al.

(2012) presented a model based on the theory of Dominik and Tielens (1997) that fits very well to experimental results. They were able to reproduce the compressive behavior of dust aggregates and in later papers also showed that the code could simulate bouncing and erosion in collisions (Seizinger and Kley 2013, Seizinger et al. 2013). However, since every single monomer has to be considered in n-particle simulations, computing power quickly becomes a limiting factor. Once aggregates reach a size of a few hundred micrometers, it is not feasible to use MD to predict their behavior.

On the other hand, SPH simulations are able to simulate larger aggregates. Originally created to simulate fluid behavior, it can also be used for dust aggregates. The dust aggregates are divided into discrete elements that have a certain spatial distance. Their physical properties are then obtained by summing up over all other elements that lie within range of the kernel, a function detailing how each element is to be ‘smoothed’ over their surroundings. An application to SiO_2 dust aggregates was presented by Geretshauser et al. (2010). While the code was calibrated on several experiments (Güttler et al. 2009), simulations of collisions of cm- to dm-sized aggregates (Geretshauser et al. 2011a,b, Meru et al. 2013) often have a ‘fluid’ look to the visualized results. This does not match experimental observations, leaving doubts to their scalability. This may be due to uncertainties in the relations between the elastic constants of the material. Just like MD simulations, SPH also requires massive computing power, especially when a larger parameter space is being investigated.

Krijt et al. (2013) also presented a model predicting the coefficient of restitution in a collision. They added energy dissipation by viscoelastic cracks, a dissipation mechanism working even below the threshold for plastic deformation, to the JKR model and successfully fitted it to a broad range of experimental results. Instead of solving the equations of motion for every constituent particle as in MD simulations, they solve the equation of motion for the complete colliding body. The approach is similar to the one presented in this work. However, the model presented here is aimed at collisions of porous aggregates, whereas Krijt et al. (2013) concentrate on solid spheres of different materials.

Since the growth of dust aggregates in growth simulations is very sensitive to the transition from sticking to bouncing collisions (Zsom et al. 2010), obtaining more data to constrain the position, width and slope of the transition zone is of high interest. In the following section a computationally inexpensive approach using the equation of motion for the complete dust aggregate is presented, where the adhesive forces are described using the effective surface energy and properties measured for macroscopic dust aggregates.

3.2 Equation of motion

The collision of two dust aggregates can be described with an equation of motion. The forces acting on the aggregates are decelerating them, govern the loss of energy and re-accelerate them. In this model three forces are considered: *(i)* an elastic compression force following the theory of Hertz, *(ii)* adhesive van der Waals forces acting over the contact area, *(iii)* a fully plastic deceleration force during the penetration.

Several simplifications have been implemented into the model. The dust aggregates are assumed to be spherical and of equal material, size and mass. Therefore, the values for Young’s modulus, radius and mass are twice as large as their reduced counterparts.

All effects of porosity and surface roughness on the contact are incorporated in the effective surface energy as introduced in the previous chapter. Collisions are assumed to be perfectly central at an initial velocity v_0 and rotation of the aggregates is negligible. All calculations are done in the center of mass of the two-particle system.

Solving Equation 3.3 for the force yields an expression for elastic Hertzian contacts:

$$F_{\text{Hertz}} = \sqrt{\frac{16RE^2}{9}} \cdot \delta^{3/2}, \tag{3.13}$$

where R and E are the reduced radius and reduced Young's modulus as given above, respectively. While the aggregates are in contact and the indentation δ grows, elastic energy is stored within the aggregates. The above equation gives the resulting force that is responsible for driving the aggregates apart again and determines the point of deepest penetration.

The van der Waals forces are governing the adhesion between bodies. The energy in an adhesive contact E_{vdW} is given by the unit surface energy γ times the contact area A. The stored adhesive energy is equivalent to the integrated van der Waals force acting during the indentation:

$$E_{\text{vdW}} = \gamma A = \int F_{\text{vdW}}\, d\delta. \tag{3.14}$$

The contact area has the form of the base area of a spherical cap, where the cap is the volume that is compressed in the collision. Therefore, the contact area is given by the amount of indentation by $A = \pi(2r\delta - \delta^2)$. Owing to the porosity of the aggregate the real contact area is smaller, but this effect is accounted for by using the effective surface energy introduced in Equation 3.11. Solving for the van der Waals force yields:

$$F_{\text{vdW}} = \frac{dE}{d\delta} = \frac{d}{d\delta}\gamma_{\text{eff}}\pi(2R\delta - \delta^2) = 2\gamma_{\text{eff}}\pi(2R - \delta). \tag{3.15}$$

As a source of energy dissipation a volume-pressure work of the form $W = \int p\, dV$ is assumed, where W is the work, p the pressure and dV the change in volume, respectively. Here, the volume of the spherical cap affected by the penetration is approximated by a cylinder with the area of the spherical cap and the height being the intrusion depth. For small intrusions this overestimates the volume by approximately a factor of 2, which is compensated for by adding a factor of 0.5 to the term in the equation of motion. The major advantage is that the area is constant and does not change for a fixed intrusion depth. Since the related force is equal to the derivative of the work with respect to the taken path, which equals the depth of intrusion in this case, we find for the force term:

$$F_{\text{plastic}} = \frac{dW}{d\delta} = p\,A = p\pi(2R\delta - \delta^2). \tag{3.16}$$

Here, p is the pressure distribution at the area of contact. For simplicity, it is assumed that p is constant over the area and always reaches the yield pressure of 200 Pa (Blum et al. 2006).

With the forces acting on the colliding aggregates defined, the equation of motion can be compiled. The signs are chosen in such a way that attractive forces are positive, while repulsive forces are negative. The basic equation reads:

$$\begin{aligned} F_{\mathrm{total}} &= -F_{\mathrm{Hertz}} + F_{\mathrm{vdW}} - 0.5 \cdot F_{\mathrm{plastic}} && (3.17) \\ M\ddot{\delta} &= -\sqrt{\frac{16RE^2}{9}} \cdot \delta^{3/2} + 2\pi\gamma_{\mathrm{eff}}(2R - \delta) - 0.5 \cdot p\pi(4R\delta - \delta^2). && (3.18) \end{aligned}$$

This equation of motion is used to determine the outcome of a collision. It should be noted that the term for the plastic deformation F_{plastic} is only considered for positive velocities, i.e. only while the aggregates approach each other. If the adhesive forces are large enough, the aggregates will stick together and a velocity of $v = 0$ is reached for a finite, positive value of δ. If the energy stored in the elastic compression is high enough to drive the aggregates apart, then the aggregates will part with a finite velocity v, which can be used to determine the coefficient of restitution of the collision. The numerical implementation of the model will be described in the following section.

3.3 Simulations of collisions among millimeter-sized dust aggregates

In order to solve Equation 3.18 numerically, it is reformulated in such a way as to eliminate all units. First, a scale-free length y is introduced by substituting $y \equiv \delta/R$:

$$\begin{aligned} \ddot{\delta} &= -\frac{4R^{1/2}E}{3M} \cdot \delta^{3/2} + \frac{2\pi}{M}\gamma_{\mathrm{eff}}(2R - \delta) - \frac{p\pi}{2M}(4R\delta - \delta^2) && (3.19) \\ \frac{\ddot{\delta}}{R} &= -\frac{4RE}{3M} \cdot \left(\frac{\delta}{R}\right)^{3/2} + \frac{2\pi}{M}\gamma_{\mathrm{eff}}\left(2 - \frac{\delta}{R}\right) - \frac{p\pi R}{2M}\left(4\frac{\delta}{R} - \left(\frac{\delta}{R}\right)^2\right) && (3.20) \\ \ddot{y} &= -\frac{4RE}{3M} \cdot y^{3/2} + \frac{2\pi}{M}\gamma_{\mathrm{eff}}(2 - y) - \frac{p\pi R}{2M}(4y - y^2). && (3.21) \end{aligned}$$

As a last step, the equation is multiplied by a time squared to remove the last units. Here, $\tau \equiv R/v_0$ is chosen as a typical timescale, leading to the final form of the equation:

$$\ddot{y}\tau^2 = -\frac{4RE\tau^2}{3M} \cdot y^{3/2} + \frac{2\pi\tau^2}{M}\gamma_{\mathrm{eff}}(2 - y) - \frac{p\pi R\tau^2}{2M}(4y - y^2). \qquad (3.22)$$

The differential Equation 3.22 was solved numerically with an IDL (Interactive Data Language) program, using a classical (i.e. 4th order) Runge-Kutta method. The Runge-Kutta method is a procedure to numerically solve differential equations of first order by approximating the derivative with difference quotients. Since the equation of motion does not contain any terms with the first derivative with respect to the time, it can be divided into two differential equations of first order. Both of these equations are solved simultaneously, using the results after each time step as input for the next time step of the other equation, respectively.

As a discrete time step for the integration, $\Delta t = 10^{-6}$ seconds is chosen. While the contact time of colliding dust aggregates has as of yet not been measured directly, high-speed video data and analysis of experiments suggests that it is on the order of milliseconds

Table 3.1: This table contains all parameters used in the calculations solving the equation of motion of the dust aggregates.

parameter		value	source
collision velocity	v	10^{-5} ... 10 $\mathrm{m\,s^{-1}}$	
integration time steps	Δt	10^{-7} ... 10^{-5} s	
aggregate radius	r	$5 \cdot 10^{-6}$ ... $15 \cdot 10^{-3}$ m	
monomer radius	r_m	$0.5 \cdot 10^{-6}$ m	Kothe et al. (2013, fig. 3)
SiO_2 density (monomer)	ϱ	2600 $\mathrm{kg\,m^{-3}}$	Blum et al. (2006, table 1)
aggregate filling factor	ϕ	0.35	Weidling et al. (2012, fig. 2)
Young's modulus	E	$72.1 \cdot 10^9$ Pa	Clark (1966, page 173)
Poission's ratio	v	0.18	Clark (1966, page 173)
yield pressure	p	200 Pa	Blum et al. (2006, table 2)
surface energy (for two identical bodies)	γ	0.037 J/m^2	Heim et al. (1999)

(Heißelmann et al. 2007, Weidling et al. 2009). The contact time can also be calculated using Hertzian theory (Hertz 1881):

$$t_\mathrm{contact} = 3.12 \sqrt[5]{\frac{m^2}{v_0 r E^2}}. \tag{3.23}$$

For two aggregates with a mass of $m = 4.8 \cdot 10^{-7}$ kg, a radius of $r = 0.5 \cdot 10^{-3}$ m, Young's modulus of $E = 8100$ Pa and and collision velocity of $v_0 = 0.01\ \mathrm{m\,s^{-1}}$, this yields a collision time of 3 milliseconds. In order to ensure high temporal resolution of the collisions investigated in the simulations, the time step was chosen 3 orders of magnitude smaller than the expected duration. The time steps were decreased or increased dynamically up to an order of magnitude for particularly high or low velocities.

In order to get a broad overview of the results, the aggregate size and collision velocity were varied over several orders of magnitude each. For the radius two values per magnitude were used, for the velocity 20 values per order of magnitude. While this large span will quite possibly include parameter ranges where the above assumptions do not hold, the emerging picture is plausible in most cases. Table 3.1 gives an overview of the parameters used in the simulations.

Each simulation results in a time sequence giving the penetration depth of the two colliding dust aggregates over time. This is used to determine the outcome of the collision. *(i)* If the total acting force and, therefore, the acceleration, as well as the velocity of the aggregates are zero while the penetration depth is larger than zero, the aggregates can not separate again and the aggregates stick together. *(ii)* Should the penetration depth reach zero again after the initial intrusion and the repulsing force is bigger than the adhesive force, bouncing will occur. The velocity of the aggregate separation at this time is used to calculate the coefficient of restitution for the collision. *(iii)* In case not enough energy is dissipated into plastic deformation to prevent the penetration depth from reaching one aggregate radius, the calculation is stopped at this point and the aggregates are considered to have fragmented.

Figure 3.1 shows the result of two dust aggregates with a diameter of one millimeter

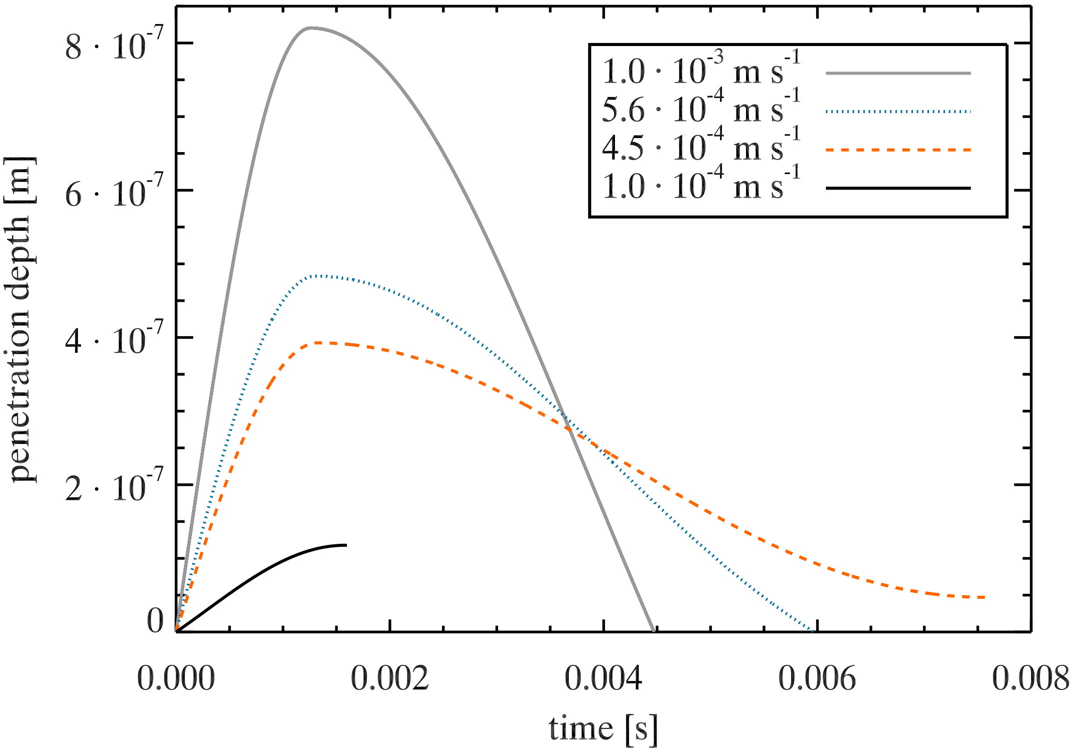

Figure 3.1: Penetration depth of two dust aggregates with a diameter of one millimeter each at four different collision velocities from 10^{-4} to 10^{-3} m s^{-1}. The two lower velocities result in sticking of the dust aggregates, since the resulting velocity reaches zero while they are still in contact. The two higher velocities result in bouncing and the aggregates separate from each other with different velocites.

colliding at different velocities. At 10^{-4} m s^{-1} (solid black line) nearly all energy is dissipated until the deepest intrusion is reached and the aggregates stick together shortly after reaching it. At a velocity of $4.5 \cdot 10^{-4}$ m s^{-1} (dashed orange line), the aggregates are parting again, however, the van der Waals force overcomes the Hertzian load before the aggregates are separated and they stick together with a small intrusion. This is the highest velocity where sticking occurs (comparable to the value found by Weidling et al. 2012), for higher velocities the aggregates bounce off each other. At $5.6 \cdot 10^{-4}$ m s^{-1} (dotted blue line) and 10^{-3} m s^{-1} (solid gray line) the aggregates separate, but the contact time is different, as are the maximum intrusion depth and the rebound velocity. Velocities higher than about 1.4 m s^{-1} lead to a penetration depth greater than the aggregate radius. The figure also shows that the calculations result in a contact time on the order of milliseconds, as estimated above.

Figure 3.1 already shows a trend of an increasing maximum penetration depth with increasing velocity. The values for the complete range of velocities for dust aggregates with a diameter of one millimeter are plotted in Figure 3.2. For very low velocities the increase is rather small, but from about 10^{-4} m s^{-1} the maximum penetration depth increases with $v^{0.9}$. Since higher collision velocities equal higher collision energies, the resulting increase in penetration depth was to be expected.

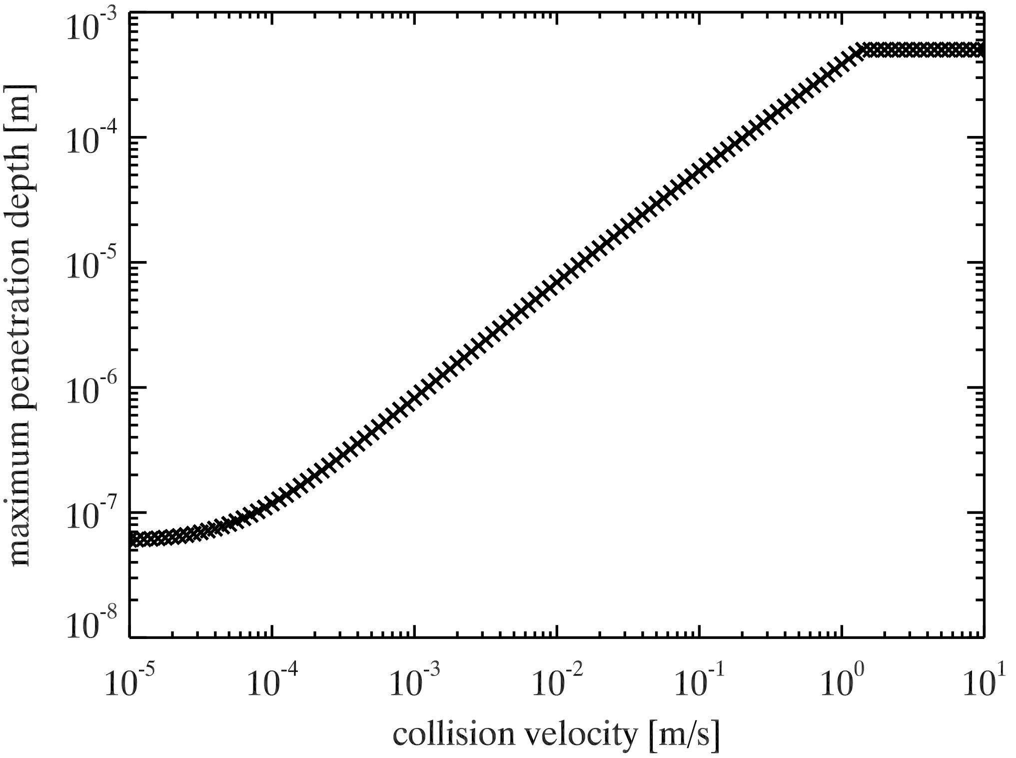

Figure 3.2: This plot shows the maximum penetration depth of two dust aggregates with a diameter of one millimeter over a large range of collision velocities. While the maximum penetration depth increases slowly for velocities less than about 10^{-4} $\mathrm{m\,s^{-1}}$, it increases with a power law for higher velocities. The highest values are capped artificially, as the calculations were stopped once the penetration reached the aggregate radius.

The constant value of 0.5 millimeters maximum penetration depth for high velocities is a result of the stopped calculations. Starting at 1.4 $\mathrm{m\,s^{-1}}$, it gives the velocity at which fragmentation occurs. This agrees very well with the results of Blum and Münch (1993), who found fragmentation for velocities larger than about one meter per second for millimeter-sized aggregates. While the condition of having to reach one aggregate radius in penetration for fragmentation to occur is arbitrary, changing this would still result in similar values for the fragmentation velocity.

Another interesting parameter is the coefficient of restitution, a measure for the loss of energy in the collision. Figure 3.3 shows this trend over the collision velocity. Up to the sticking velocity of $4.5 \cdot 10^{-4}$ $\mathrm{m\,s^{-1}}$, all collisions lead to sticking. Numerical artifacts lead to some values being displayed as slightly greater than zero, while in reality they are not. For velocities higher than this, the coefficient of restitution is increasing continuously until fragmentation sets in. This behavior is in contrast to the predictions by Thornton and Ning (1998), who found a steep increase of the coefficient of restitution up to a maximum value at the yield velocity and a slow decrease for higher velocities.

A monotone increase of the coefficient of restitution is also surprising, because the dissipated energy is assumed to be proportional to $p \cdot V$ and, thus, to the penetration depth to the third power. However, this means that the dissipated energy increases with $v^{2.7}$,

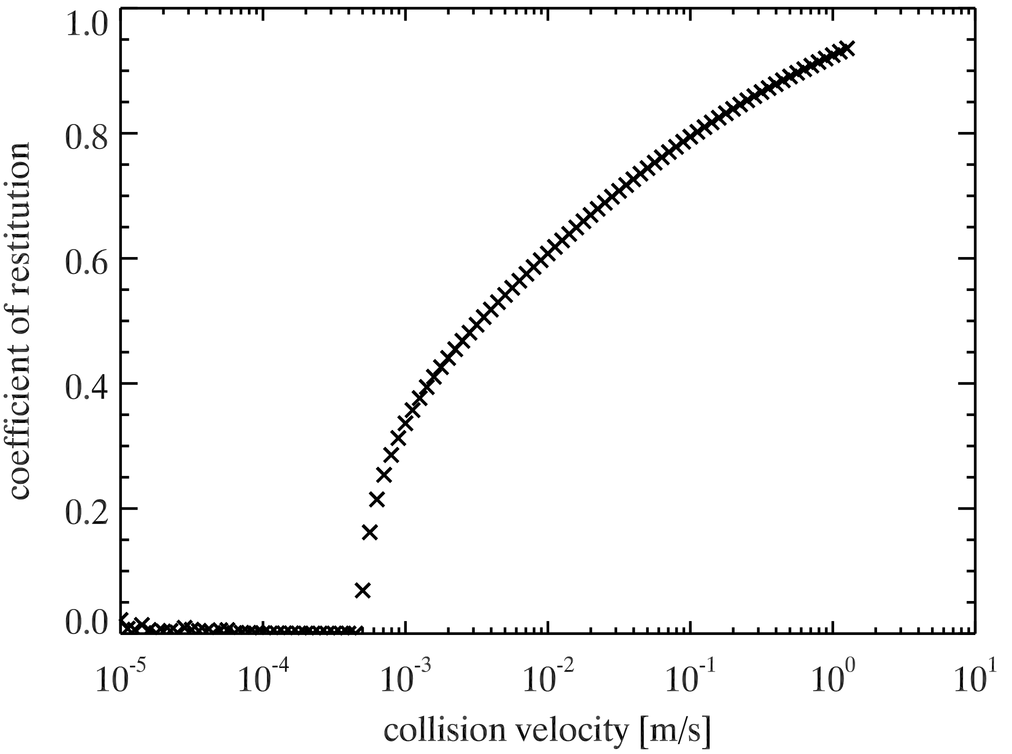

Figure 3.3: The coefficient of restitution is increasing monotonic with collision velocity in the bouncing regime between $4.5 \cdot 10^{-4}$ m s^{-1} and 1.4 m s^{-1}. At lower velocities the aggregates stick together, while they fragment at higher velocities.

whereas the impact energy only increases with v^2. Therefore, a decrease of the coefficient of restitution with increasing collision velocity would be expected, just as Thornton and Ning (1998) predict. It is not clear which effect causes the observed behavior. While the energy stored elastically in the Hertzian contact also increases with collision velocity, the high amount of energy dissipation into plastic deformation should still be the dominating factor.

The values for the sticking and fragmentation velocity for millimeter-sized aggregates observed in experiments can be reproduced with the simulations, as shown above. However, the main goal is to make predictions for aggregates sizes that are not easily accessible in experiments. Therefore, the above calculations were performed for a broad range of aggregate sizes from a diameter of 10 μm up to 30 mm, spanning roughly 10 orders of magnitude in mass. The resulting sticking velocities are shown in Figure 3.4 (blue crosses). The sticking velocity is lower for larger aggregates, as expected. Except for a jump between aggregates with a diameter of 3 mm and 10 mm, respectively, it follows a power law with a slope of -0.75.

The dashed gray line shows the velocity where 50% of the aggregates stick as given by Weidling et al. (2012). The absolute values compare very well, considering that this line may be shifted up or down depending on which part of the experimentally observed transition zone from perfect sticking to perfect bouncing is compared to the calculations, where the transition is sharp. The slope of -0.78 is also comparable. This is a good sign that the calculations are a viable model for adhesive elastic-plastic contacts as described by Thornton and Ning (1998), since this model was used in the original collision model by Güttler et al. (2010). The velocity given in Weidling et al. (2012) was in turn based on this, but scaled to fit the experimental results found for millimeter-sized aggregates.

However, experiments with aggregates of other sizes showed that this theoretical slope does not hold in reality. Kothe et al. (2013) combined results of experiments with aggregates from a few hundred micrometers to a few millimeters in size and arrived at a slope of -2.2 (solid gray line in Figure 3.4) for the 50% sticking velocity. For these sizes the absolute values agree with the calculations presented here, but for larger or smaller aggregates the prediction is very different.

It cannot be stated at this time which prediction is more accurate, since the theory considers idealized systems, whereas in experiments there will always be scatter in the results due to imperfections in the aggregates or other parameters that will differ slightly. Also, the experimental range of aggregate sizes has to be increased, since the slope found in Kothe et al. (2013) is based on a rather narrow size range. While the absolute values from Weidling et al. (2012) are also based on a single aggregate size only, the slope is based on the model from Thornton and Ning (1998), which should be valid for a large size range. However, the results presented in Section 6.3 indicate that the experimental results for dust aggregates differ from that model.

The orange pluses in Figure 3.4 give the sticking velocity for various sizes when using the equation for the effective surface energy as given in Weidling et al. (2012, their equation 7). The sticking velocity obtained this way is a factor of 1.8 higher than with γ_{eff} as given in Equation 3.11, but shows an identical trend otherwise.

Using the unaltered surface energy without the Hertz factor as found by Heim et al. (1999, black circles in Figure 3.4) yields sticking velocities very different than the other simulations and the experiments. Millimeter-sized aggregates would stick together up to velocities of about 0.1 $\mathrm{m\,s^{-1}}$, which is unrealistically fast. Additionally, these calculations do not yield results for smaller aggregates, as even the smallest used velocity of 10^{-5} $\mathrm{m\,s^{-1}}$ resulted in a penetration of one aggregate radius and, therefore, fragmentation.

The fragmentation velocity is constant over all sizes and all versions of the effective surface energy at 1.4 $\mathrm{m\,s^{-1}}$ (for the unaltered surface energy this is true only for aggregates larger than 0.3 mm). The collision model by Güttler et al. (2010) also gives a constant value for the collision of equally-sized aggregates, though it is a little lower with 1 $\mathrm{m\,s^{-1}}$.

While in reality the value will depend on the surface energy, since it is required to break the contacts between monomers in order for fragmentation to occur, in the model presented here the energy of the incoming aggregate is reduced by plastic and elastic energy, both of which do not depend on the surface energy. Therefore, the collision energy determines the intrusion depth, as the aggregates penetrate deeper into each other until this energy is completely converted. In reality, the effectiveness of the energy dissipation will likely be a function of the structure of the aggregate, which in turn depends on the cohesion.

It should be noted that there are arguments for a size dependency of the fragmentation velocity. Windmark et al. (2012a) present a collision model featuring such a trend and e.g. Beitz et al. (2012) also found experimental evidence for it. However, as with the sticking velocity the experimental values are based on experiments in a rather small size interval,

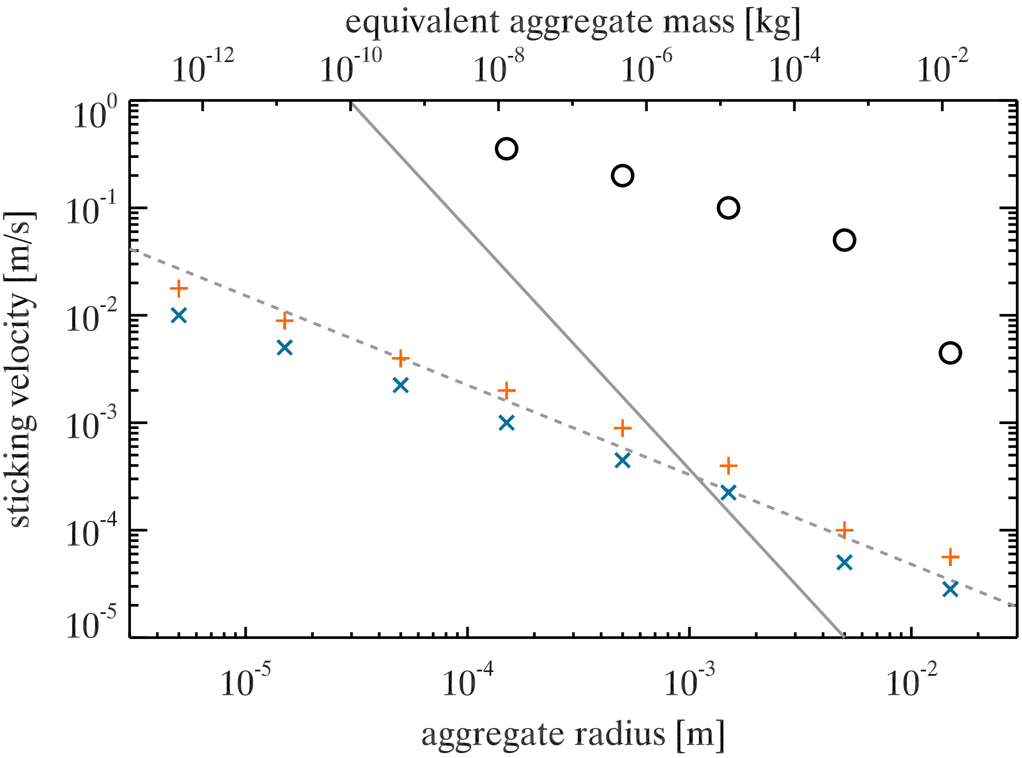

Figure 3.4: This plot gives the sticking velocity for colliding dust aggregates by solving their equation of motion. The surface energy was varied between the one given in equation 3.11 (blue crosses), the effective surface energy as given in Weidling et al. (2012, orange pluses) and the classic surface energy as found by Heim et al. (1999, black circles). The solid and dashed gray lines represent the 50% sticking velocity as given by Kothe et al. (2013) and Weidling et al. (2012), respectively.

which leaves room for mistakes in the determination of the boundary.

In conclusion, the model presented above does very well in reproducing the observed behavior of millimeter-sized dust aggregates. The dependence of the sticking and fragmentation velocities upon the aggregate size are also in line with previous experimental results, however, those are limited to a rather small size range and may deviate for aggregates significantly larger or smaller than a millimeter. The detailed results of the simulations, in particular the predictions for the coefficient of restitution, leave severe doubts as to the validity of the presented model, since newer experiments and other models show a different behavior for high velocities.

While the scaling of the surface energy with the Hertz factor works very well for the millimeter-sized aggregates, it remains to be seen whether this also holds up for aggregates of very different sizes or if another effect than the reduced contact area is causing the difference of aggregate behavior when compared to solid spheres and the Hertz factor just happens to fit with millimeter-sized aggregates. Kothe et al. (2013) showed that the sticking velocity of dust aggregates with a diameter of 100 to 250 μm is much higher than predicted with this model. This indicates that more adjustments need to be made to the models for solid spheres when dealing with porous bodies than only scaling the surface energy.

Another possibility for the mismatch of experiments and contact theory is that the theories are based on van der Waals forces. Kimura et al. (2015) speculate that the forces between silicate aggregates are caused by silanol (Si-OH) groups instead, which are much stronger and would lead to higher surface energies. They argue that previous measurements are biased towards lower surface energies by layers of water on the surface of the silicates. However, previous experiments have shown that the interaction between monomers can be well described by van der Waals forces (e.g. Blum and Wurm 2000). Since the interaction between aggregates is just an integration over the interaction of several monomers of identical material, there is no reason why the van der Waals forces should be replaced by something else.

With the results of the presented model not being scalable, it was investigated whether the model by Krijt et al. (2013) is applicable to dust aggregates. The material parameters were taken from Table 3.1. In order to account for the porosity, the volume filling factor was introduced and multiplied to the mass of the aggregate. Instead of using the specific surface energy for SiO_2, the effective surface energy γ_{eff} was used. The interatomic distance was adopted unchanged, as was the ratio of relaxed to instantaneous elastic modulus, which is a constant describing the viscoelastic crack theory (Greenwood 2004). This leaves two free parameters, the viscous relaxation timescale T_{vis} and the time step for the numerical iteration. While the latter is a parameter defining the resolution of the calculations, the viscous relaxation timescale denotes both how quickly stresses are distributed in a body as well as the form of the adhesion hysteresis at the edge of the contact area.

As a calibration, the sticking threshold of $0.117\ \mathrm{m\,s^{-1}}$ found by Brisset et al. (2016) for dust aggregates with a mean diameter of 325 μm was used. For velocities faster than this they found bouncing to set in. The model by Krijt et al. (2013) allows for the calculation of the coefficient of restitution for different collision velocities, just as the model presented in this work. For velocities below the sticking threshold it will result in a coefficient of restitution of 0, as the collision partners have no relative velocity when sticking together. For velocities above the sticking threshold, $0 < \varepsilon \leq 1$ is expected.

While Krijt et al. (2013) give an estimate on the expected relaxation timescale depending on the particle radius (their figure 8 b)), here, the coefficient of restitution was calculated for a broad range of T_{vis}. For the dust aggregates, viscous relaxation timescales from $2.8 \cdot 10^{-2}$ s to $8.8 \cdot 10^{-10}$ s were used, with the steps separated by a factor of $\sqrt{10}$. According to Krijt et al., the shorter timescales are more likely to yield plausible results. Heißelmann (2015) found a timescale of $2.85 \cdot 10^{-7}$ s to fit experiments with centimeter-sized water ice spheres. For the ice particles, a change of the viscous relaxation timescale by a factor of $\sqrt{10}$ changed the sticking threshold by less than one order of magnitude. Therefore, it was to be expected that the spacing for the chosen timescale would suffice to yield a visible change in the coefficient of restitution, if the model was valid for the dust aggregate material parameters.

The calculations were performed for various lengths of the time step of the numerical iteration (10^{-3} to 10^{-7} times the relative change of the radius of the contact area). For each of these timescales and time steps, the coefficient of restitution was calculated for 40 logarithmically equidistant velocities in the range 10^{-5} to $10^{1}\ \mathrm{m\,s^{-1}}$.

For timescales larger than $8.8 \cdot 10^{-7}$ s, the coefficient of restitution is always found to be 0, indicating sticking at all studied velocities. This result is not observed in experiments.

Using timescales smaller than this yields coefficients of restitution larger than 0 in the considered velocity range. They have a maximum value at around 10^{-5} m s^{-1} and then gradually decline with rising velocity. However, no value for T_{vis} could be found that yields a sticking velocity in the range of 0.1 m s^{-1}. Using values of the viscous relaxation timescale smaller than $8.8 \cdot 10^{-10}$ s resulted in inconsistent results, likely due to numerical problems with very small numbers. Therefore, these values were not compared to the experimental results of Brisset et al. (2016).

In conclusion, the model by Krijt et al. (2013) does not seem to be applicable to porous aggregates without further modifications. One reason might be the mechanism for dissipation of energy. In their model, energy is dissipated by viscoelastic cracks, while in the model presented in this work energy is dissipated by plastic deformation. For very porous aggregates, both effects might have to be included due to their low yield strength.

Thus, to date no model can correctly predict the contact behavior of dust aggregates from monomer sizes up to several milli- or centimeters in size. Therefore, it is necessary to further enhance the models by understanding the physics of the contact, but also to increase the number of experiments covering the parameter space (i.e. combinations of dust aggregate sizes, volume filling factors, and collision velocities) as important reference values for these models.

4 Design and development of the experimental setup MEDEA

The transition from perfect sticking to perfect bouncing in the collision of dust aggregates is crucial for planet formation, as shown in Chapter 2. It governs the size that dust aggregates can grow to via direct growth, that is by acquiring additional mass in collisions with other dust aggregates. This size is an important factor in subsequent growth mechanisms, such as the gravitational instability.

As has been shown before, experiments are important in understanding collisions among dust aggregates. While not all parameters in the course of planet formation are accessible in the laboratory, it is important to calibrate numerical models with those parameters that can be studied in experiments. The collisions among millimeter-sized dust aggregates occur at velocities of millimeters to centimeters per second in the protoplanetary disk at a distance of 1 AU to the star (Weidenschilling 1977a, Johansen et al. 2014). Utilizing the energy loss in mutual collisions, these velocities can be achieved in ensembles of aggregates in microgravity. In this chapter the experimental setup and its concept are presented (Section 4.1) along with an overview of the developments of suitable opportunities for microgravity and of the setup itself (Section 4.2) and the materials used in the experiments (Section 4.3).

4.1 The experimental setup

The goal of the experimental setup is to provide free collisions of millimeter-sized dust aggregates at velocities of millimeters to centimeters per second to investigate the transition from sticking to bouncing as shown in Chapter 2. It is very difficult to consistently achieve these low collision velocities for pairs of aggregates in the laboratory. Therefore, a different approach is used, following the experiments by Heißelmann et al. (2010). An ensemble of particles is floating freely in a defined volume under microgravity conditions, leading to collisions among each other which are observed with a camera. Due to deformation of the dust aggregates, energy is lost in each collision (Heißelmann et al. 2007). Thus, the aggregates slow down with each collision, until they reach the desired relative velocities of millimeters per second. Advantages of this method are that a range of velocities can be investigated with a single experiment run and that the collisions are completely free from outside effects.

This section describes the mechanical setup that was used to achieve the goals mentioned above. Due to the chronological developments explained in the following section, the setup was redesigned several times. The changes for each iteration are detailed below.

MEDEA-I: For the first drop-tower campaign four identical setups were constructed that only shared a vacuum system. Each unit consisted of a particle chamber mounted on a shaking mechanism (see Figure 4.1 a)) and had its own optical system including a camera.

The particle chamber was a glass cylinder with an inner diameter of 25 mm. It had ISO-KF flanges at both ends, allowing for the integration into a vacuum system. The lower end was sealed by a custom-made aluminum flange (see Figure 4.1 b)). Above the glass cylinder a flexible bellows was mounted in order to allow for shaking of the particle chamber, while the parts above the bellows remained in fixed positions. A grating with a mesh size of 50 μm was attached to the centering ring between the glass cylinder and the bellows. The mesh filled the entire cross section of the glass cylinder and was used to prevent dust aggregates from leaving the particle chamber while allowing for evacuation.

The four experiment units were connected by a vacuum system. The vacuum system included a pressure gauge, a valve and a connection to the outside of the drop tower capsule. During the preparation of the experiment outside of the drop tower, a vacuum pump was connected to the system to evacuate the particle chambers. Then the valve was closed and the vacuum pump was disconnected. Inside the drop tower the valve was opened again when the pressure in the drop tower tube reached that inside the experiment's vacuum system. This allowed for an evacuation down to about 0.1 mbar, matching the pressure inside the drop tower.

The lower flange was built in two different versions, each used in two of the four units. One version featured a small hole covered by a lid. The hole served as a particle reservoir. Particles were stored inside this volume at the beginning of the experiment, then the lid was opened and the particles were released into the particle chamber. The other version had an electromagnetic coil built into the inside of the closed socket. A permanent magnet was placed on top of the flange and the particles were poured on top of it. By applying a current to the coil, the permanent magnet could be accelerated away from the bottom flange and into the particle chamber by electromagnetic repulsion. This mechanism was used to introduce a solid, fast-moving object into the ensemble of dust aggregates which is able to destroy clusters of aggregates that withstand the shaking. While two of the top flanges also had a particle reservoir, this was not used anymore after the first experiments, since the dust aggregates got stuck in the reservoir instead of drifting into the observable volume.

The lower flange of the particle chamber was attached to a shaking mechanism (see Figure 4.1 c)). A DC motor was turning an eccentric wheel with its axis being horizontal. This generated an up- and down-motion of the uppermost part of the wheel. The plate holding the lower flange of the particle chamber was mounted on top of the wheel. Thus, turning the wheel resulted in an up- and down-motion of the particle chamber. The amplitude of the shaking could be adjusted by the shape of the wheel, while the frequency was given by the voltage applied to the motor. Springs connecting the shaker housing to the plate and the bellows on top of the chamber served to ensure contact of the plate and the wheel in microgravity.

In order to place dust aggregates into the particle chamber, the chamber and the top and bottom flanges can be removed from the shaker and vacuum system. The dust aggregates are placed onto the lower flange (cf. Figure 4.1 b)) or stored inside the reservoir, if applicable. Due to the large number of aggregates required to reach an optical depth of

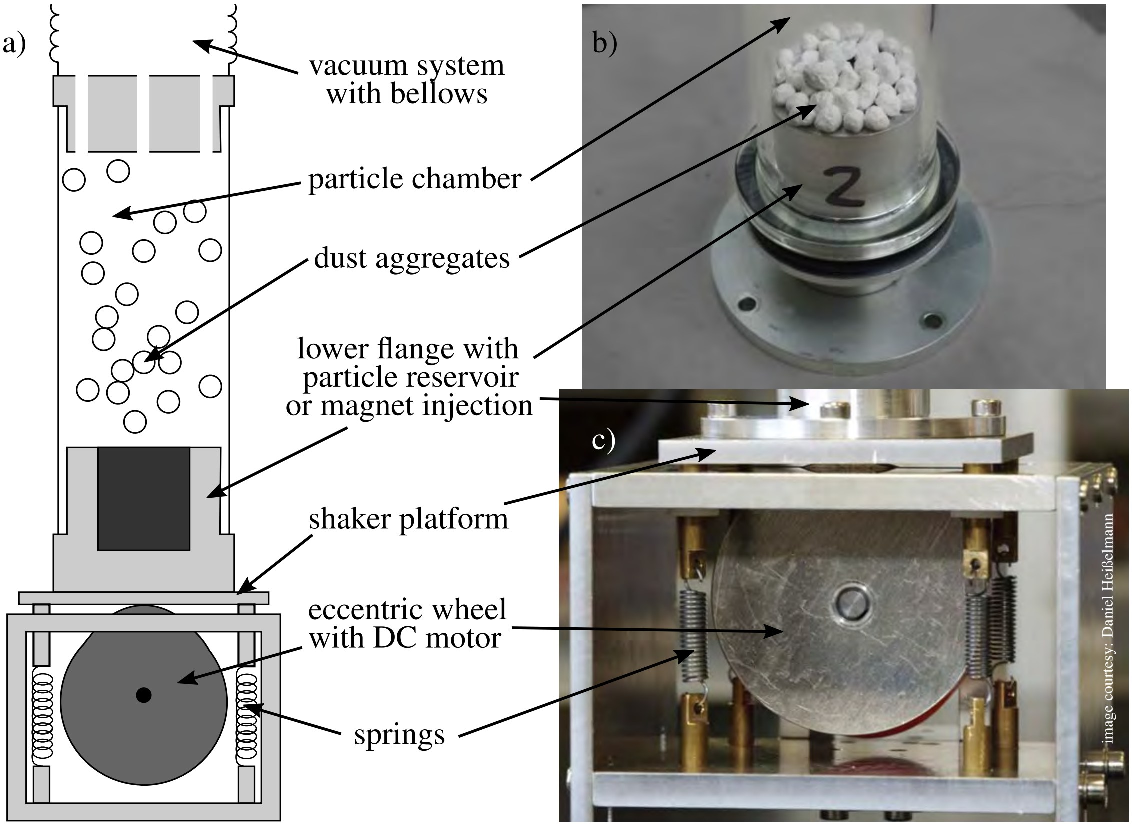

Figure 4.1: a) Schematic of the MEDEA-I shaker setup. A vacuum particle chamber containing the dust aggregates is mounted on top of an eccentric wheel (the eccentricity in the sketch is exaggerated for illustrative purposes). The vacuum bellows and springs push it into contact with the wheel. b) The particle chamber (diameter 25 mm) filled with dust aggregates. c) Close-up of the shaking mechanism. The eccentric wheel is lifting the particle chamber up from the housing.

about 0.3, the number of aggregates is not counted but instead estimated by filling them into a defined volume before they are inserted into the setup. Here, the optical depth is defined as the ratio between the sum of the cross sections of all aggregates within the experiment and the visible cross section of the particle chamber.

In order to observe the collisions among dust aggregates, a high-speed camera was used. One requirement was a minimum resolution of 500 × 500 pixels, since this amounts to a resolution of 0.1 millimeter per pixel or 10 pixel in diameter for a millimeter-sized aggregate, if the particle chamber fills the entire field of view. This is sufficient to quantify differences in size of the dust aggregates.

To be able to observe the aggregates moving by one pixel between two frames, a temporal resolution of better than 100 frames per second is required at the desired aggregate velocities of around 1 $\mathrm{cm\,s^{-1}}$. The Allied Vision ProSilica GE680 meets these requirements at 640 × 480 pixels and 205 frames per second, but the camera needs an external recording system. In the early planning stages Blue Origin stated that their command module would record any data obtained by ProSilica cameras. Therefore, a recording system was omitted in this setup.

Two Photron Fastcam MC-2 systems that are available at the drop-tower facility were used for the first drop-tower campaign. Both feature a recording unit with two camera heads each, allowing for the observation of all four setups at the same time. The camera heads have a resolution of 512 × 512 pixels at 500 frames per second, also meeting the requirements of the optical system.

The optical setup allows for a very precise determination of the velocity. The resolution using the Photron Fastcam MC-2 was 94 μm per pixel. If just one pixel of an aggregate with a typical area of 100 pixels is moving in the time between two frames, this corresponds to a velocity of $1/100$ pixel/frame = $4.7 \cdot 10^{-4}\ \ \mathrm{m\,s^{-1}}$. Since aggregates are usually observed over a much longer duration, theoretically velocities even lower than this value can be measured by fits to the aggregates trajectories.

For a precise analysis of the collisions, the three-dimensional trajectories of the involved dust aggregates are required. Images of the particle chamber from at least two different points of view are necessary in order to obtain three-dimensional information. Here, two images were created by placing a rectangular mirror, serving as a beam-splitter, and two additional flat mirrors in the optical path (see Figure 4.2 a)). Thus, two images of the particle chamber separated by an angle of 90° can be recorded with a single camera.

The particle chamber was illuminated from the back by an LED array. LEDs with a maximum emission at a wavelength of 470 nm were chosen, since the sensors of the ProSilica cameras have a their highest sensitivity at blue colors. They were arranged in a dense hexagonal pattern. One diffusor was placed directly in front of the LEDs and a second one was attached to the particle chamber in order to widen the radiation angle of only 15° and provide a homogeneous illumination. The LEDs were connected in such a way as to limit the maximum voltage to 26 V. This value is below the 28 V provided on the rocket and serves to keep a homogeneous background with no fluctuations to the brightness if the voltage should drop due to the battery being drained.

This version of the MEDEA setup is also described in detail in Weidling et al. (2012).

MEDEA-II: For the MEDEA-II setup the mirrors were exchanged for an equal-sided prism. The prism allows for the observation of the particle chamber from two perspectives separated by an angle of 30° (see Figure 4.2 b) and c)). While this angle requires some additional calculation to obtain the three-dimensional information (see Section 5.1), the particles are much easier to correlate in the two views. The prism also reduces the floor space occupied by each setup. Since the two perspectives are separated by a smaller angle, only one LED array was necessary to illuminate each setup.

The experiments with the MEDEA-I setup showed that dust aggregates had stopping times on the order of seconds (Weidling et al. 2012, Appendix A). The stopping time is the time until the velocity of a particle has decreased to $1/e$ of its original value due to gas drag. In the Epstein regime, it is inversely proportional to the gas density. Therefore, a lower gas pressure within the particle chamber, which corresponds to a lower gas density, leads to an increase in the stopping time. High stopping times are desirable, as the effect of gas drag on the particle velocities can be neglected in this case.

To achieve this, the vacuum system was redesigned completely, now using CF (ConFlat) components. The particle chambers were custom made, where the glass cylinder, the bellows and the metal flanges at the ends were included into a single piece (cf. Figure 4.3 a)). A turbomolecular pump was included in the connection between the chambers, improving the vacuum quality to about 10^{-4} mbar. This increased the stopping time far be-

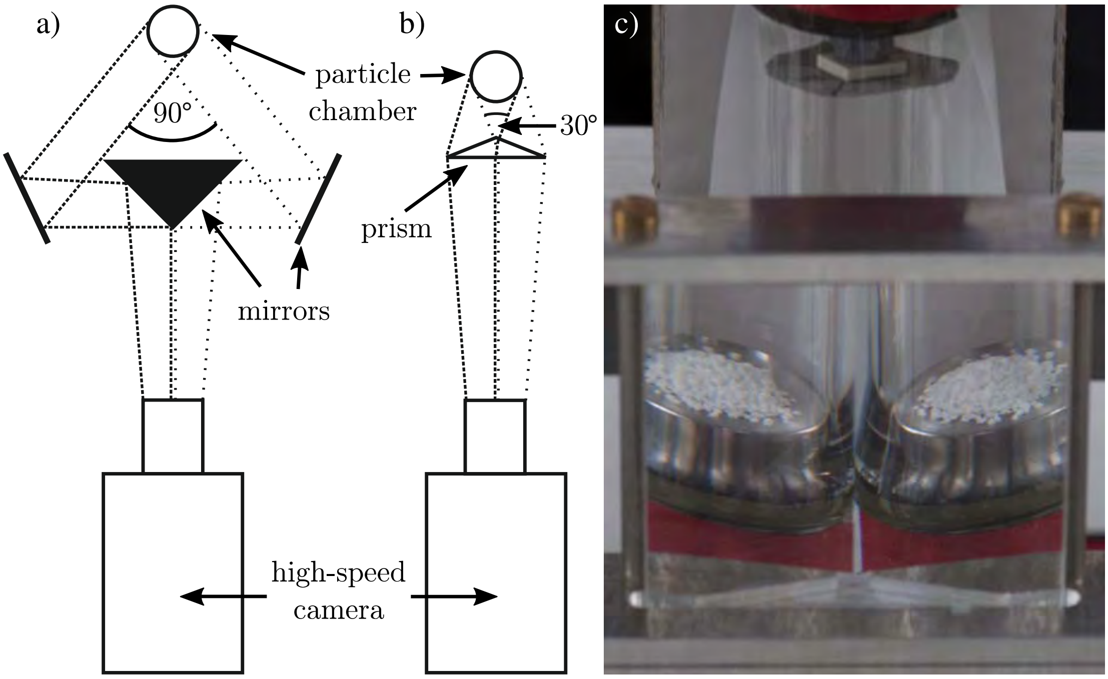

Figure 4.2: a) Illustration of the optical path in the MEDEA-I setup. A rectangular mirror splits the camera view and two plane mirrors on the sides deflect the view onto the particle chamber. The two views are separated by 90° in this method. b) Sketch of the optical path for all setups from MEDEA-II to MEDEA parabolic. An equal-sided prism serves as both beam-splitter and deflector, resulting in two views separated by 30°. c) View of the particle chamber through the prism. The apparent skewness of the lower flange is a result of the picture being taken from above the optical axis.

yond the duration of the experiment, since the lower pressure, and therefore, longer mean free path of the gas molecules means that the aggregate is in the Epstein drag regime. With the stopping time being inversely proportional to the pressure, increasing the vacuum quality by a factor of 1000 increases the stopping time by as much (Blum 2006, their equation 102).

In order to get closer to an actual flight model for the suborbital flight, three of the setups with the configuration stated above were mounted together into a single frame with dimensions of $40 \times 40 \times 40$ cm^3. In one of the setups, the lower flange was modified to hold a small inset for the particle chamber that was a small particle chamber with a height of 17 mm and a diameter of 10 mm itself. This inset was used to study the collisional behavior of dust aggregates with a diameter of 100 to 500 μm (Kothe et al. 2013). For these experiments the lens was exchanged for a telecentric lens with a longer focal length to increase the resolution and avoid distortion of the images.

MEDEA-III: In a next step, the LED arrays were improved to enhance the homogeneity of the illumination in both perspectives. The arrays were split in two halves which were placed behind the particle chamber as before, but the two halves were now angled towards one another under an angle of 150°. Thus, each half was directly facing in one of the observation directions.

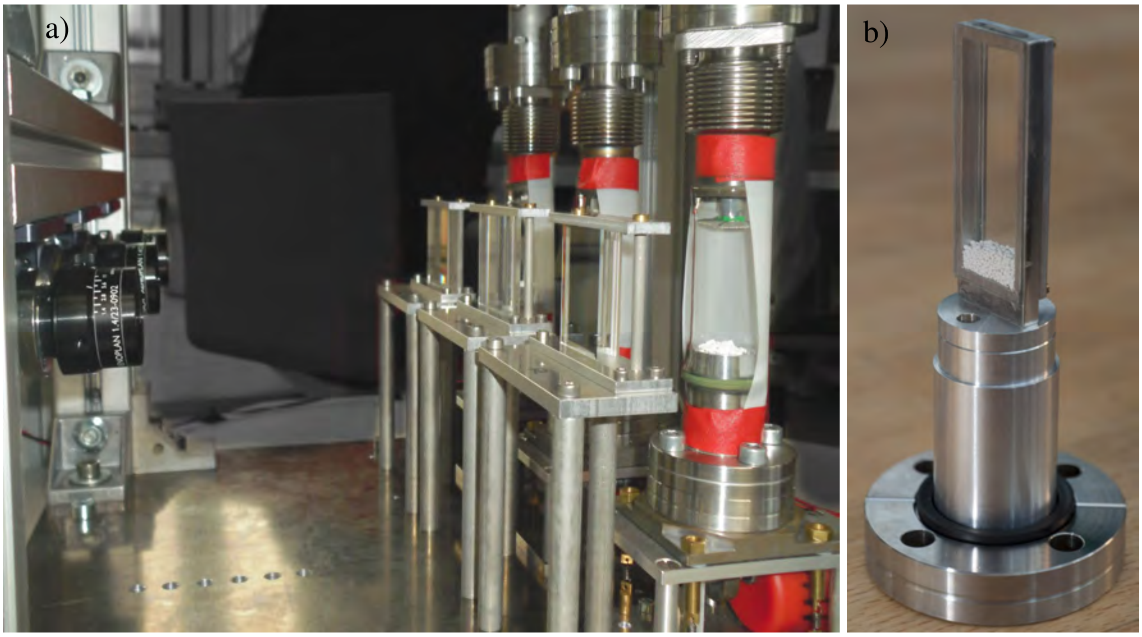

Figure 4.3: a) Three MEDEA-III setups integrated in a single framework. On the left hand side the high-speed cameras can be seen, on the right-hand side the particle chambers with attached diffusor sheets are mounted on their shakers. The prisms are mounted between the two components, the LED arrays are not visible. b) Image of a quasi-2D inset (4 mm depth) bottom flange for the particle chamber filled with dust aggregates with a diameter of 0.5 to 1 mm. With this inset, single collisions can be observed at higher optical depths.

The vacuum system connecting the three setups was changed to a single custom-made piece, reducing the number of seals and connections. It also featured a flange to attach a pressure gauge. A manually controlled valve was used to preserve the vacuum after the vacuum pump was shut down. While it was not used in the drop tower, this was necessary for the following suborbital flights.

A new inset for the particle chamber restricted the space available to the dust aggregates to a depth of a few millimeters, therefore creating a quasi-2D setup (Figure 4.3 b)). This allowed for the observation of individual particles at high number densities without their cross sections overlapping too much. However, it also dramatically increases the influence of the collisions with the walls.

The wheels of the shakers were exchanged for wheels with smaller radii. These were round instead of eccentric, but had an off-center axis to create an identical up- and down-movement of the experiment container. This served to decrease the load on the motors and to lower the chance of the motor getting stuck.

MEDEA suborbital: For the suborbital flights with Armadillo Aerospace, the MEDEA-III setup was used with additional data storage and experiment control. Both were adapted from the SPACE experiment (Brisset et al. 2013). Each of the three setups had a dedicated data storage system and experiment control, making them independent of each other – except for the shared vacuum system. The complete setup is shown in Figure 4.4 a).

The data storage system consisted of a single-board computer (Toradex Robin Z530 V2.0) capable of processing the jumbo frames that the high-speed camera (Allied Vision

ProSilica GE680) generates. A baseboard (Toradex Daisy V1.1) provided the ethernet connector to the camera and an S-ATA connector. The latter was linked to an adapter with a fast CompactFlash card (Transcend CompactFlash 32GB 600×) with sufficient storage to record for the whole duration of the rocket flight. Upon powering the computer, a program was started automatically that established connection with the camera, configured it and then started streaming the data to the CompactFlash card until power was shut down.

The experiment control consisted of a printed circuit board with a microcontroller and several DC/DC converters. It served to distribute the power supplied by the rocket to the different components of the setup. The microcontroller controls which components are supplied with power and regulates the frequency of the shaking mechanism following a pre-defined procedure upon receiving the motor shut-down signal. However, in the case of a shorter duration of motor thrust (as experienced in the flights with Armadillo Aerospace), a second signal, e.g. at liftoff, would have been very helpful and should be included in all future iterations of the setup to use the available time as well as possible.

MEDEA parabolic: A parabolic flight campaign was used to test a new shaking mechanism for the setup. It consisted of two electromagnetic coils that were arranged perpendicular to each other. A permanent magnet in their center can be moved up and down by applying an alternating current to the coils. This movement is relayed by an axis attached to the magnet. One of the coils is attached to the axis of the other coil and the particle chamber in turn is attached to the axis of the second coil (see Figure 4.4 b)). This creates a 2D shaking system, moving the particle chamber up and down as well as towards and away from the camera. In contrast to a motor driven shaker, the coils can not get stuck. While the amplitude of the movement is restricted by the confines of the permanent magnet, the frequency can be changed by changing the frequency of the alternating current. For the parabolic flight both coils were attached to the same power source. Decoupling the two coils would allow for independent frequencies and facilitates an adaptation of the shaking level to different levels of residual acceleration in the two directions. However, this would require two power sources, which would mean a significant increase in mass that is not favorable in suborbital flights.

For the particle chamber a glass tube with a KF-25 flange at one end is used. The other end of the glass cylinder is closed by a fixed glass plate. At the end with the flange, a lightweight electromagnetic valve is attached via an adapter piece (see Figure 4.4 b)). With a mass of less than 600 g, the assembly can be attached directly to the shaker without further mechanical support. As each particle chamber has its own valve, each setup of this type is completely independent of other experimental units.

The camera was exchanged for a GoPro modified in such a way as to allow mounting any lens with a C-mount (Back-Bone GoPro Hero 3+). Therefore, a lens with an appropriate focal length and less distortion than the standard lens can be used. The WVGA video mode allows for the recording of movies with a frame rate of 240 images per second at a resolution of 848 × 480 pixels, sufficient to meet the spatial and temporal requirements of the experiment. The advantages over the ProSilica camera are the internal battery and recording system of the GoPro. However, the internal video storage comes at the cost of compressed movie files being stored instead of lossless single images. This leads to some artifacts when decomposing the movie into single images again, but tests in the laboratory showed that the quality is sufficient for the desired analyses. The positions of the aggregates can still be resolved, but the cross section is artificially enlarged if the aggre-

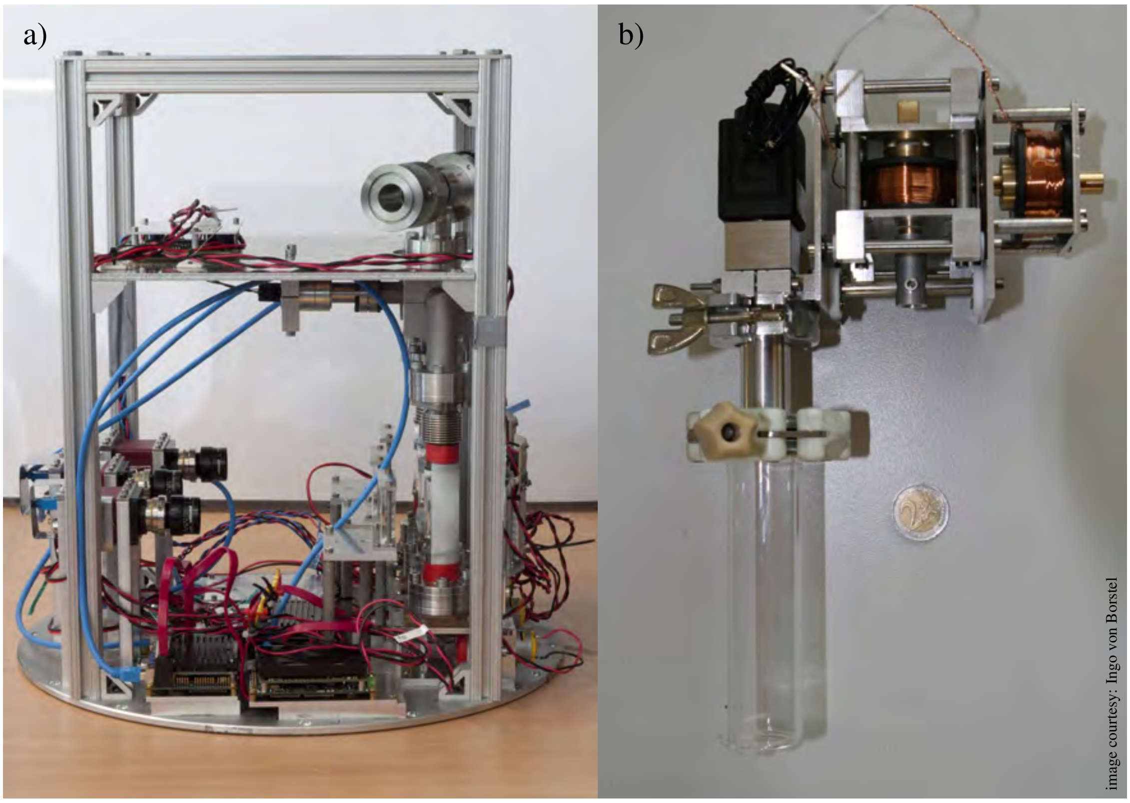

Figure 4.4: a) Complete setup MEDEA suborbital with 3 individual units. The units are not parallel to each other due to less than ideal optical paths. The high-speed cameras are mounted on the left-hand side, the particle chambers on the right-hand side. On the baseplate three single-board computers can be seen in the front. b) Electromagnetic shaker for the parabolic flights. The coils are supplied with an alternating current and push a permanent magnet in their middle for a 2D shaking movement. The particle chamber is sealed by an electromagnetic valve on its top.

gates move quickly. This leads to a larger uncertainty in the aggregate mass, but yields information on the velocities as before.

For the parabolic flight just one complete setup was used due to mass restrictions. However, in order to get data on several aggregate materials and sizes, the particle container was exchanged for another one in the middle of the flight. The shaking frequency and times were adjusted manually during the parabolas. The GoPro was set to record during the whole duration of the flight.

MEDEA suborbital II: A preliminary analysis of the parabolic flights revealed that the electromagnetic shaker is not suitable for the experiments due to too high accelerations and velocities with the available control components. Therefore, the shaking is driven by a motor again, though with completely different mechanics to convert the rotation to a linear motion. An eccentric is driving a two-sided actuator, moving the particle chamber linearly in one direction and a counterweight into the opposite direction. The actuator is mounted at an angle of 45° to the floor in order to move radially and vertically in the rocket to counter residual accelerations both from spin and atmospheric drag.

Additional electronics boards are added for each setup. They are used to convert

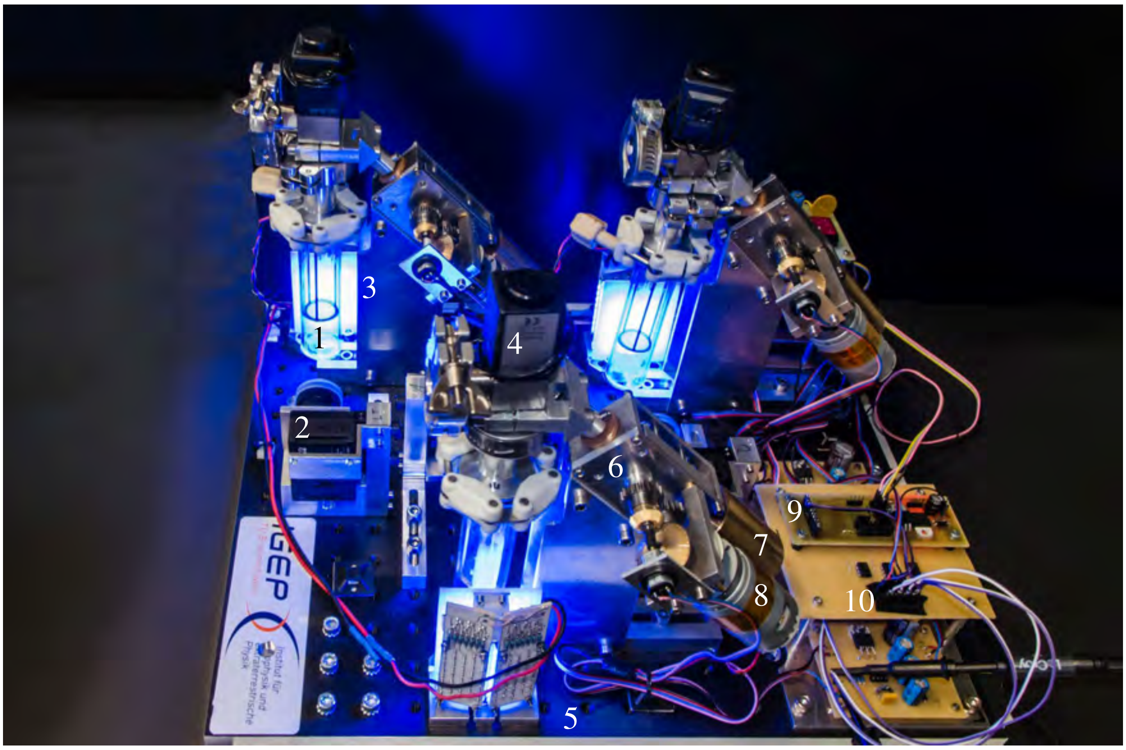

Figure 4.5: Full MEDEA suborbital II setup with 1) particle chamber with mesh, 2) GoPro camera, 3) LED array, 4) electromagnetic valve, 5) baseplate, 6) shaking mechanism mounted at 45° angle, 7) counterweight, 8) DC motor, 9) microcontroller, 10) control electronics.

the power from 28 VDC to -15 to +15 V, as well as provide controllers that adjust the power output to keep the shakers at the desired frequency in case of higher loads. The control voltage is monitored by a microcontroller. Digital input signals from the payload controller at pre-defined times are used to trigger the respective control voltage.

The GoPro cameras are fitted with a lens with a focal length of 12 mm. The short focal length leads to a clearly observable difference in size of aggregates that are in the front or in the back of the chamber, respectively. Since this can be used to obtain depth information from a single perspective, no prisms are included in this iteration. This allows for more compact setups and increases the resolution of the video.

The particle chamber has not been modified from the parabolic flights. Having small chambers with individual valves allows for them to be installed into the experiment as late as possible and separately from the other components. An image of the complete setup can be found in Figure 4.5.

The expected duration of a microgravity quality of better than $5 \cdot 10^{-3}$ g is between 120 and 180 seconds of the total duration of the flight, with the least residual acceleration in the middle of this time frame. In order to have comparable results, all three shakers follow the same frequency profile (see Table 4.1). It is designed to allow for two separate phases of aggregate growth and two different modes of aggregate separation. Once the main rocket engine is cut off (MECO), the shakers work at their maximum frequency of 10 Hz, where Hz refers to the revolutions per second. This is reduced in 3 steps to 0.7 Hz, when the residual acceleration is expected to drop below $5 \cdot 10^{-3}$ g and the coast phase

Table 4.1: Overview of the shaker profile used in the suborbital flight with Blue Origin. After the main engine is cut off, a strong shaking phase disperses the aggregates. 30 Seconds after separation of main engine and the crew capsule containing the experiment, the aggregates are dispersed again. Next, the shaker will run at the lowest setting, allowing for very low velocities around apogee. From 90 to 110 seconds after the separation event the shaking velocity is ramped up linearly to its maximum to find the fragmentation velocity of formed clusters. The shaker is switched off once the parachutes are deployed and the microgravity phase ends.

flight event	shaker frequency [1/s]	wall velocity [cm/s]	wall acceleration [g]
MECO + 0.5 s	10	7.2	0.46
separation	4.9	3.5	0.11
separation + 5 s	1.25	0.9	0.007
separation + 15 s	0.7	0.5	0.002
separation + 30 s	10	7.2	0.46
separation + 38 s	0.7	0.5	0.002
separation + 90 s	0.7 . . . 10	0.5 . . . 7.2	0.002 . . . 0.46
separation + 110 s	10	7.2	0.46
under chutes	0	0	0

starts. The shaker acceleration of $2 \cdot 10^{-3}$ g ensures that the aggregates do not cluster at the walls, while the wall speed of 5 mm s^{-1} should be low enough as to prevent fragmentation of clusters of aggregates. After 35 seconds, the shakers are operated at 10 Hz again for 8 seconds. This serves to desagglomerate any clusters and resets the experiment for the phase with the best quality of microgravity around apogee. The duration of 8 seconds is long enough to ensure that all aggregates that do not collide with other aggregates reach the far wall due to residual acceleration.

After the strong shaking phase, the frequency is reduced to 0.7 Hz again until 90 seconds after separation. Depending on the exact flight profile, apogee is expected to be in the middle or towards the end of this phase. Here, the residual acceleration is lowest and the aggregates experience very few disturbances, allowing them to collide and slow down to very low velocities. Afterwards, the shaker frequency is increased linearly over the next 20 seconds, from 0.7 Hz to 10 Hz. This corresponds to a linear increase in the velocity of the shaker walls. The time at which clusters start to break up automatically gives the critical velocity for bound aggregates to survive subsequent collisions. The maximum frequency of 10 Hz is then maintained until the parachutes are deployed.

4.2 Development of microgravity opportunities

Ever since the decision to stop the Space Shuttle program, NASA started funding private companies who intend to develop rockets that might replace the Shuttle in the future. One of these companies is Blue Origin, which is building a reusable suborbital rocket that can carry several passengers or scientific payloads up to a height of approximately 100 km as a step towards orbital spaceflight. As part of the flight demonstration program for the suborbital rocket, several Pathfinder experiments were chosen for the first flights to test the collaboration with researchers and provide early access to the rocket. One of these experiments is MEDEA (Microgravity Experiment on Dust Environments in Astrophysics), proposed by Prof. Colwell from the University of Central Florida. The experiment consists of three parts, one of which is built in Florida, one by Dan Durda at the Southwest Research Institute and one part is the setup presented in this work.

Suborbital flights offer continuous microgravity durations of about three minutes, which is much longer than can be obtained by any other method except reaching orbit. The quality of the microgravity changes during the flight, with the least residual acceleration around apogee. The flights place several restrictions on the experimental setups, such as limits to size, mass and electric power, as well as necessitating an autonomous operation of the experiment. The setup described in this work, called MEDEA, was developed with these limitations in mind.

The setup has to fit in a double size locker of the Blue Origin payload system. This offers an available volume of $51.6 \times 41.8 \times 47.4$ cm^3 and a maximum mass of 22.68 kg. An electrical peak power of 200 W is available via four channels with 28 VDC each. The power output can be activated based on trigger signals or predefined time lines and it is possible to use real-time rocket data to trigger certain events. Blue Origin also offered a video recording system, providing a camera from the Allied Vision ProSilica series and a data storage system as part of the on-board computer.

As a first step, an experiment campaign at the drop tower in Bremen was performed in June 2010. The experimental setup, called MEDEA-I, was not yet in a state that would have fit inside the rocket. Its main purpose was a test of several ideas for the suborbital flight. A scientific analysis of the resulting data (Weidling et al. 2012) revealed that several changes would improve the setup, such as adding a turbomolecular pump to decrease the residual gas pressure and the use of prisms instead of mirrors.

As it became apparent that the rocket flight would not occur within that year, an improved version of the setup (MEDEA-II) was tested at the drop tower as well (November 2010). This setup was mounted into a casing that fit the mass and size restrictions given by Blue Origin. While the cameras were different than the ones intended for use in the suborbital flight, everything else was as close to the setup for the rocket as possible.

When the launch was delayed even further, a short third campaign at the drop tower was conducted in August 2011. While the main part of the setup remained the same, a few minor improvements were made (MEDEA-III). This campaign was also used to test additional modifications, like insets for the particle chambers.

All results presented in this work were obtained from the experiments in the MEDEA-II and -III campaigns. In total, 115 individual experiments have been conducted in the three drop tower campaigns. They were not only used to test different versions of the hardware and shaker frequencies, but also samples of several sizes and materials, which are detailed in Section 4.3. While most of the hardware performed as expected, several crucial improvements were made based on the experience from the drop tower campaigns.

By this time, several other companies intending to serve the suborbital market had emerged. One of these was Armadillo Aerospace, who offered launches of their STIG-B rocket. While this rocket places roughly the same restrictions on power, mass and dimensions as does Blue Origin, there are some important differences (MEDEA suborbital). The on-board rocket computer is used solely for the purpose of controlling the rocket.

The experiments may receive one trigger signal, but all other commands controlling the experiment sequence have to be generated and executed by the experimental setup itself. The data storage has to be included in the setup as well. Since the available cameras, chosen based on the proposal by Blue Origin, do not feature internal data storage capabilities, the command and data storage system from the SPACE experiment were adopted (Brisset et al. 2013).

The campaigns with Armadillo Aerospace took place in 2012 and 2013, but all three subsequent launches were unsuccessful in providing a microgravity environment sufficient for the experiment[1]. The first launch on 10/6/2012 resulted in a higher velocity over ground than the allowed threshold, causing the board computer to shut down the rocket motor 22 seconds after ignition. The rocket reached a maximum height of close to 4.5 km, leading to a very short and low-quality phase of reduced gravity. On 11/3/2012 the motor was shut down even earlier than that, after only 15 seconds. This time the reason was the detection of a bubble of gas in a hose transporting propellant, leading the board computer to falsely conclude that the rocket had run out of propellant. The apogee was at about 2.5 km over ground, and duration and quality of the microgravity were insufficient for the experiment again. However, the recovery system was working in both cases, safely landing the rocket with the experiment module under parachute. While the motor burn duration for the third launch on 1/5/2013 was the longest, it lasted only 24 seconds, leading to a maximum height of the trajectory of 5.5 km. This time, the parachute failed to open and the rocket crashed to the ground with the experiment module. The CompactFlash cards containing the experiment video footage were unscathed, but the data was not scientifically usable. The particle chambers were destroyed in the crash, as were the prisms. The other components suffered some dents, but were still operational.

In the meantime, Blue Origin pursued building its rocket and announced a possible launch in early 2015. Since crucial components of the previous setup were destroyed in the crash, a new setup was built based on the lessons learned. The SPACE experiment showed that two-dimensional shaking can be very helpful in case the rocket is rotating. While Blue Origin's rocket has thrusters to null out rotation, there is as yet no data of their effectiveness. Redesigning the shaking mechanism also influenced the choice of the new particle chambers. Additionally, a change in the camera system was announced by Blue Origin. Now, the cameras of choice are GoPros that store the recorded data internally on a microSD card. A customized casing of the camera allows for the mounting of any C-mount lens to replace the stock wide angle lens.

An opportunity to test the new setup (MEDEA parabolic) was the participation in a parabolic flight in May 2015. Since the setup was only appended as an addition to an already existing, larger experiment, the mass and size restrictions were comparable to the suborbital flights. In order to further reduce the required resources, just one experiment unit was used. While the optical setup was satisfying in the previous alterations, the vacuum system and shaker were modified completely. The new vacuum system was much lighter and consisted of off-the-shelf components. The electromagnetic shaker was less likely to get stuck than the eccentric motor in the previous versions, but turned out to be too fast. Due to the automatic video compression of the GoPro and the accompanying

---

[1] Detailed reports on the launch campaigns and their results can be found at `https://web.archive.org/web/20160412230544/http://armadilloaerospace.com/n.x/armadillo/home/news?` under STIG B-x Mission Report.

decrease of the quality of the video data, the parabolic flights were a good opportunity to test its viability under microgravity. Although some details are lost, the quality turned out to be sufficient for an analysis of the dust aggregate collisions.

For the suborbital flight with Blue Origin, the shaking system was redesigned yet again. The setup was augmented with dedicated controllers for the motors, while the prisms were omitted to allow for a better resolution. The manual controls of the parabolic flight for shaker and illumination were replaced with the automated payload control system offered by Blue Origin's Payload Controllers. Three identical units are build into the payload locker to make the most use of the available space and microgravity time.

On 6/19/2016, the suborbital flight with Blue Origin took place. The payload reached an altitude of close to 328,000 feet (100 km) and landed safely. The microgravity time, which is defined here as the duration between the *separation* signal (given when the crew capsule separated from the propulsion module) and the *coast end* signal (given when the acceleration consistently exceeds 3.22 $\mathrm{ft/s^2}$, i.e. 1 $\mathrm{m/s^2}$) was 168 seconds, close to three minutes.

While the flight itself was a success, the experiment did not work as planned. Out of the three setups, two of the GoPros did not record any footage at all, while the third one only recorded until the separation event. Therefore, no videos of the microgravity phase were obtained. The most likely reason is a short circuit in the shaker control causing a brief loss of power of the GoPro camera. If a GoPro camera loses power for less than one second, it reboots in a safe mode and will only resume recording after a press of a button. As this feature was only discovered after the flight, no means to achieve a press of the button were included in the setup.

4.3 Sample material properties

The multitude of experiments in the drop-tower campaigns was used to explore the parameter space of different colliding aggregates as well as to determine the reliability of the components of the setup. The particles used in the experiments can be divided into two groups, one being aggregates made of different kinds of dust and the other being solid particles.

For the dust aggregates, the size was varied from 100 μm to about 4 mm. Here, size always refers to the diameter. Narrow size distributions were achieved by sifting the particles through a stack of sieves with decreasing mesh sizes and using only dust aggregates left between two of the sieves. With mesh sizes of 100 μm, 250 μm, 500 μm, 1 mm, 1.6 mm, and 2.5 mm the size range can be controlled well. The effective radii are distributed approximately normally in each interval, with a slight shift towards bigger radii due to the ellipticity of the aggregates (Weidling 2010). While in most experiments just one size interval was used, others featured a combination of different aggregate radii.

In most experiments, SiO_2 was used, which was available in several microscopic forms: polydisperse irregular, polydisperse spherical and monodisperse spherical SiO_2. Mostly, the polydisperse irregular dust was used. It consists of ground down SiO_2 with a bulk density of 2600 $\mathrm{kg\,m^{-3}}$, where 99% of the monomers have a diameter between 0.5 and 10 μm (manufacturer information, Sigma-Aldrich, Silicon dioxide S5631). Measurements of this dust with particle size analyzers by Kothe et al. (2013) and Deckers and

Teiser (2014) suggest that the smallest monomers have a diameter of about 0.3 μm and confirm a maximum size of a few to 10 μm.

The monodisperse spherical monomers have a diameter of 1.5 μm and a bulk density of 2000 $\mathrm{kg\,m^{-3}}$ (Blum et al. 2006). Poppe and Schräpler (2005) showed that the size distribution is indeed very narrow. Despite the differences in the monomer structure, previous experiments could show that the respective aggregates have very similar collisional properties (e.g. Kothe et al. 2013, Brisset et al. 2016).

In the MEDEA suborbital II experiments, monodisperse dust with a diameter of 0.2 μm was used to investigate whether the monomer size has an influence on the collisions among aggregates of comparable size. According to Dominik and Tielens (1997) the energies, and therefore also the velocities, at which aggregates stick together or break apart are inversely dependant on the monomer size. Following their model, aggregates consisting of smaller monomers would stick and fragment at higher velocities than those with larger monomers.

The fourth microscopic form of SiO_2 used in the experiments also consists of spherical monomers, but with a size distribution from about 0.1 to 5 μm, centered at 1 μm (manufacturer information, Admatechs, Admafine SO-E3). Ground iron dust, with polydisperse irregular monomers, was used to investigate possible magnetic effects, but the dark dust turned out to soil the glass of the particle chamber too quickly to facilitate a proper analysis.

In order to investigate the effects of magnetism, aggregates made of iron oxide were used. However, many monomers were sticking to the particle chambers shortly after the begin of the experiment, obstructing view of the aggregates.

Other than the aforementioned variation of dust types and sizes, the number of particles in the chamber was varied. The ideal optical depth allowing for the tracking of single particles while providing enough collisions turned out to be around 0.3. Higher number densities were intentionally used in a few experiments to check for clustering effects as described e.g. by Goldhirsch and Zanetti (1993), Miller and Luding (2004), and Opsomer et al. (2012). Different size intervals were combined to investigate the effect of a large factor between the masses of two colliding aggregates.

The solid particles used in the experiments were made of glass, iron and a ceramic (Si_3N_4), respectively. Experiments with spheres with a diameter of 3 mm were carried out for all three materials to investigate the influence of the particle material on the reduction of the coefficient of restitution at low velocities (Sorace et al. 2009). For glass, additional experiments with diameters from 1 to 10 mm were performed to probe size and size ratio effects, e.g. a change of the coefficient of restitution with changing mass ratio of the collision partners as predicted by Thornton and Ning (1998).

Several experiments investigating the coating of chondrules also featured spheres made out of alumina (Al_2O_3) as analog materials for the chondrules.

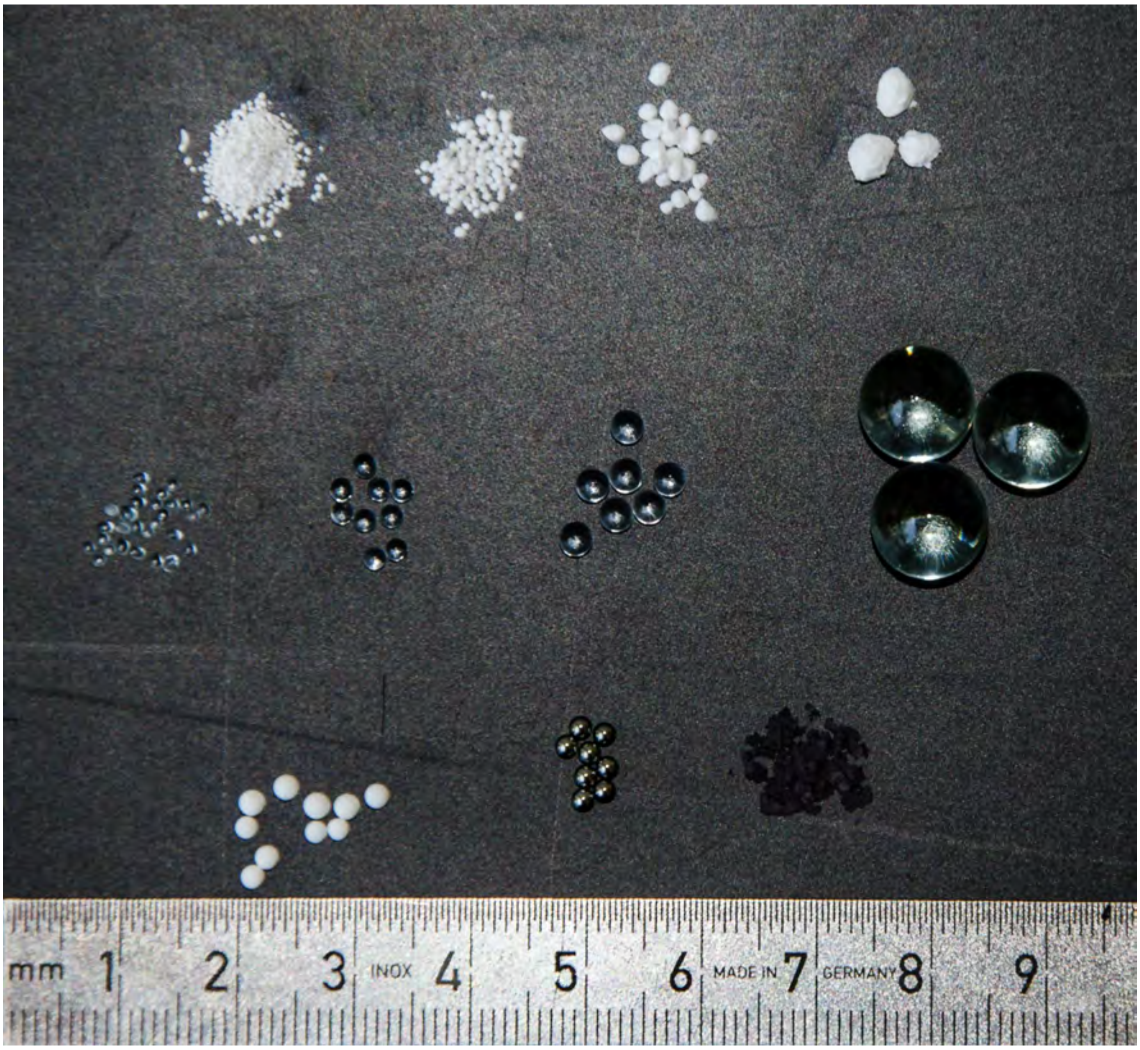

Figure 4.6: Image of different sample materials. In the upper row aggregates made of polydisperse irregular SiO_2 in different sizes ranges. The sieve mesh sizes used are: 0.25 - 0.5 mm, 0.5 - 1.0 mm, 1.0 - 1.6 mm, and 3 - 5 mm (from left to right). The second row shows glass spheres of 1, 2, 3 and 10 mm diameter, respectively. The lower row shows alumina (Al_2O_3) spheres with a diameter of 2 - 3 mm, iron spheres with a diameter of 2 mm, and unsieved iron oxide dust.

5 Analysis methods

In order to thoroughly analyze an experiment containing many dust aggregates that undergo lots of collisions, several effects have to be considered. In Section 5.1 the method of analysis is presented. The subsequent Sections 5.2 and 5.3 deal with the effects that electrical charges and rotation can have on the results, respectively.

5.1 Calculation of aggregate parameters

For analysis, experiments were chosen that featured dust aggregates around one millimeter in size and looked most promising after visual inspection. Important aspects were good desagglomeration of the dust at the beginning of the experiment, a mostly homogeneous distribution of the aggregates in the chamber, an optical depth allowing for the tracking of individual particles while providing enough collisions, and a shaker profile that prevents the sticking of a larger part of the aggregates to the glass walls of the chamber.

In order to obtain the aggregate positions over time, a semi-automatic tracking programm was used. The programm calculates and stores the position and visible area of a chosen aggregate based on a binarized version of the video frame (see Figure 5.1 b)). Binary frames are obtained by dividing the image in areas lighter and darker than a given threshold brightness. Here, the threshold was chosen in such a way as to preserve the projected area of the particles as much as possible. Comparing pixel counts of projected areas in different regions of the image made by the program and by hand confirmed that the threshold held up to this expectation and that the size of the area is not affected by the background illumination, which was not perfectly homogeneous.

The trajectories of dust aggregates are followed automatically over multiple frames by applying a linear extrapolation to the known positions. Manual corrections may be necessary, if the aggregates deviate from the linear path due to collisions with the wall or other aggregates, or if the aggregates enter an area with many other aggregates and only emerge again after longer duration. The aggregates are tracked successively in order of appearance as distinctly separated projections in the binary frames and then followed for as long as they are visible. This process ensures that all particles that may be used for analysis are being tracked and no bias is introduced by selecting those aggregates that catch the eye. During tracking any events, like deviations from the linear path, are stored with reference to the number of the frame to help find the parts of interest later on.

Once all aggregates have been tracked, a table of all collisions of the particles is generated based on the stored events. Then, the aggregates from both camera perspectives are correlated by hand and missing (i.e., a particle was tracked in one perspective but not in the other) aggregate trajectories are obtained. Often, this includes manually tracking

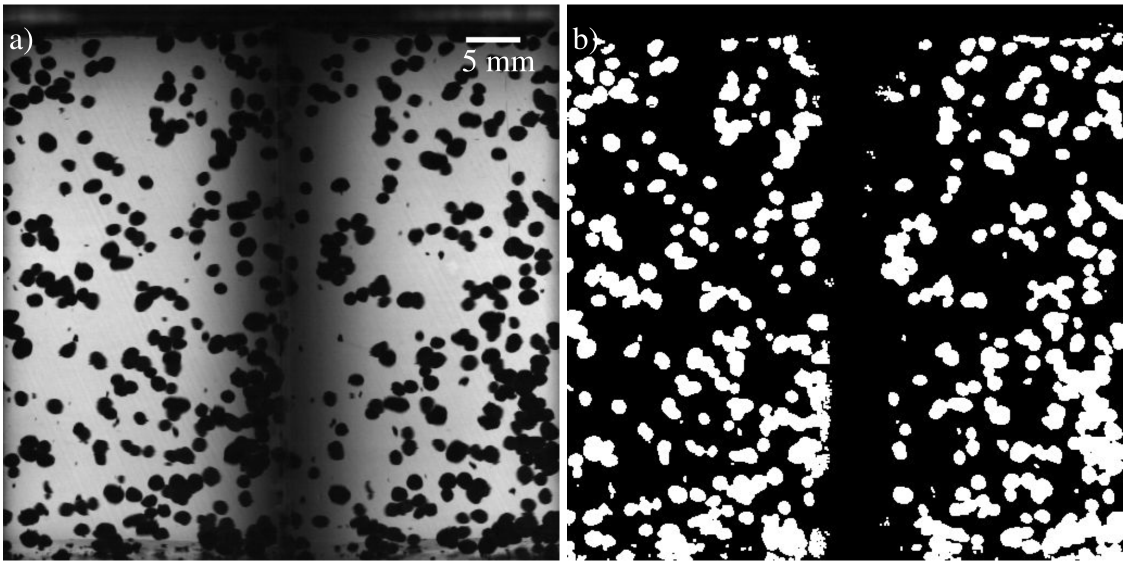

Figure 5.1: a) Example of a typical image obtained by the high-speed camera. The dark round spots are the dust aggregates, which have a size of 1 to 1.6 mm. The particle container, which has a height of around 5 cm and a diameter of 2.5 cm, is visible twice due to the prism. b) A binarized version of the image is shown on the right. The threshold to distinguish the aggregates (white) from the background (black) has been chosen is such a way as to preserve the area of the aggregates as well as possible. Aggregates in the center of the image cannot be analyzed here. All calculations are based on this kind of processed images.

the aggregate positions, i.e. clicking on the center of mass by hand instead of calculating it based on the projection, because the projection of the aggregate of interest is overlapping with other aggregates' projections in one of the perspectives. Since the program does not take into account shape, but only connected areas in the binary image, this would result in a wrong calculation of the aggregate position and mass.

Following the tracking process, the velocity of each aggregate is calculated. As a first step, the trajectory is split into undisturbed parts, i.e. parts where the aggregate does not collide, based on the event table. Afterwards, a linear least-squares fit is applied to the two tracked perspectives. To obtain the three-dimensional velocity vector, the two-dimensional values obtained from these fits are used. For simplicity, the coordinate system was chosen in such a way that two of the three coordinate axes coincide with those from the left-hand projection, with the third coordinate axis being in the line of sight of the left-hand projection. Since the camera and prism are not perfectly aligned the z-coordinate is averaged over both perspectives. The coordinates of the left-hand projection are x_l being perpendicular to both the line of sight and the axis of the particle chamber and z_l being along the axis of the particle chamber. The definition of x_r and z_r in the right-hand projection follows accordingly. With an angle of 30° between the projections the three-dimensional coordinates are then calculated as

$$\begin{aligned} x &= x_\mathrm{l} \\ y &= \frac{x_\mathrm{r}}{\sin(30°)} - \frac{x_\mathrm{l}}{\tan(30°)} = 2x_\mathrm{r} - \sqrt{3}x_\mathrm{l} \\ z &= (z_\mathrm{l} + z_\mathrm{r})/2. \end{aligned} \tag{5.1}$$

The velocities are calculated in like fashion from the fit parameters of the two-dimensional projections. For each aggregate under consideration the three components of the velocity vector are used. Relative velocities are calculated by

$$v_\mathrm{rel} = \sqrt{(v_{x,1} - v_{x,2})^2 + \left(v_{y,1} - v_{y,2}\right)^2 + (v_{z,1} - v_{z,2})^2}, \tag{5.2}$$

where the subscripts x, y, and z denote the respective components of the velocity vector and subscripts 1 and 2 denote the two aggregates. Based on these values the coefficient of restitution is calculated as

$$\varepsilon = \frac{v_\text{rel, after}}{v_\text{rel, before}}, \tag{5.3}$$

where $v_\text{rel, after}$ is the relative velocity after and $v_\text{rel, before}$ is the relative velocity before the collision, respectively. It denotes the fraction of the relative velocity that is preserved in a collision.

For the error in velocity the 1σ-uncertainty level of the linear fit is used. The error in the coefficient of restitution is then calculated by propagation of uncertainty.

Usually, the trajectories of the particles before and after a collision do not intersect numerically. Therefore, the mean value of the closest approaches of the trajectories of both particles is used for the time of contact. This, in turn, is used for the calculation of the impact parameter b (see Figure 5.2). The impact parameter denotes whether a collision is happening head-on or grazing and is defined as the projection of the distance between the two centers of mass of the aggregates perpendicular to the direction of their relative velocity. Using the definition of the vector product, the impact parameter can be calculated as

$$b = |\vec{b}| = |\vec{R}| \cdot \sin\alpha = \frac{|\vec{R} \times \vec{v}_\mathrm{rel}|}{|\vec{v}_\mathrm{rel}|}, \tag{5.4}$$

where $\vec{v}_\mathrm{rel}$ denotes the relative velocity vector, $\vec{R}$ the vector between the two centers of mass and α is the angle between these two vectors. The position of the centers of mass is calculated using the fitted trajectory at the time of contact.

In order to normalize the value for the impact parameter such that 0 denotes a perfectly central and 1 a perfectly grazing collision, b has to be divided by the sum of the aggregate radii. Since the aggregates are not perfectly spherical and not necessarily of the same size, the distance between the centers of mass at the time of contact is used here instead.

5.2 Influence of long-range forces

Calculating the velocities from linear fits is only feasible if all external influences on the particles can be neglected. The main sources of external forces acting on the aggregates can be of magnetic or electric nature. Magnetic influence is ruled out a priori by choosing

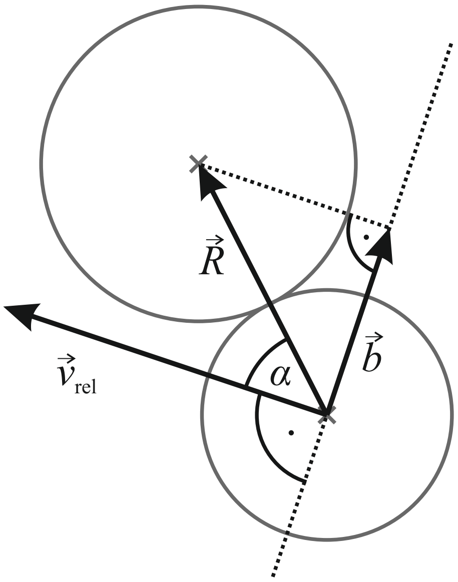

Figure 5.2: Sketch of a collision between two aggregates with relative velocity $\vec{v}_{\mathrm{rel}}$. Their centers of mass are connected by $\vec{R}$, with α being the angle between the two. The impact parameter b quantifies how grazing the collision is.

SiO_2 as the material of the dust aggregates, since this is non-magnetic. However, SiO_2 is also an insulator, which can lead to triboelectric charges accumulating on the surface (Poppe et al. 2000b), which then exert a Coulomb force on other charged aggregates. Therefore, the aggregates' trajectories were analyzed with respect to electrical charging as a possible source of disturbance.

In the vicinity of other charges a charged aggregate feels an attractive or repulsive force, leading to an acceleration. If this was an important mechanism for the dust aggregates, a quadratic fit to the aggregate trajectories would yield much better results than a linear fit. As a measure for the goodness of fit, the reduced χ^2 was calculated both for the linear and the quadratic fits. In case of linear data the values for the linear fit χ^2_{lin} and for the quadratic function χ^2_{qua} are expected to be approximately the same, with the latter being slightly smaller. However, for data coming from accelerated aggregates, χ^2_{qua} should be significantly lower than χ^2_{lin}.

Figure 5.3 shows the ratio $\chi^2_{\mathrm{lin}}/\chi^2_{\mathrm{qua}}$ for all trajectories of aggregates involved in a collision that were based on at least 10 data points. These aggregates were chosen since they were definitely in the vicinity of other aggregates and a possible acceleration due to Coulomb forces could be measured most easily for them. Shorter trajectories were omitted as they may appear to be curved due to binarization effects or the rotation of the aggregates while in reality they are straight and could potentially give wrong results when comparing the goodness-of-fit parameter in these cases. The solid orange and black lines show the ratio for the x and y coordinate, respectively. In both coordinates, one value is not shown (0.002 for the x and 0.023 for the y coordinate). These values are numerical artifacts, since the quadratic fit already includes the linear fit and the only difference in the calculation of the respective goodness of fit parameter χ^2 is in the denominator including the number of parameters. With identical errors of the fits and at least 10 data points, the ratio should in theory always be greater than 7/8. Therefore, these low values can only

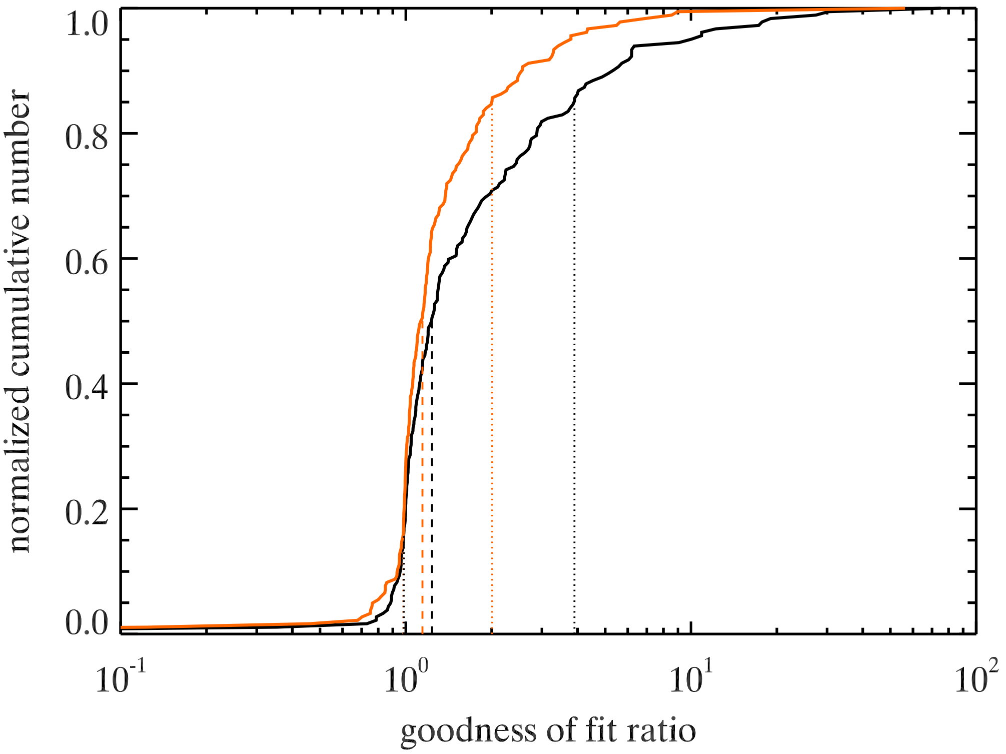

Figure 5.3: This figure shows the goodness-of-fit ratio $\chi^2_{\mathrm{lin}}/\chi^2_{\mathrm{qua}}$ for all aggregates involved in collisions. The solid orange and black lines show the data for the x and y coordinate, respectively. The dashed lines mark the median values and the dotted lines mark the 1σ range. For both coordinates there is a very low outlier value, which is 0.002 for the x and 0.023 for the y coordinate. *Data taken from Weidling and Blum (2015).*

occur, if the quadratic fit resulted in significantly higher errors, indicating a failure in the fit routine for these cases.

The median value of the goodness-of-fit ratio $\chi^2_{\mathrm{lin}}/\chi^2_{\mathrm{qua}}$ is 1.14 and 1.23 for the two coordinates, respectively. They are marked by the dashed orange and black lines in Figure 5.3. The 1σ range is 0.98 – 2.00 for the x direction and 0.98 – 3.90 for the y direction, which is marked by the dotted lines. This indicates that the quadratic fit is slightly better than the linear fit. However, both sets of goodness-of-fit parameters are within a factor of 4. If the trajectories were dominated by the quadratic term, the ratio would be several orders of magnitude higher. Therefore, it can be concluded that while the quadratic fit is slightly better, both fits are reasonably good approximations of the trajectory and the acceleration can be neglected. Also, due to the sometimes very low number of data points it can not be ruled out that alleged accelerations may be an effect of the discretization of the pixels during binarization, leading to a slight curve in the trajectory although the aggregate may have moved on a linear track.

Comparing the magnitude of the quadratic with the linear term in the quadratic fit supports the previous findings. In nearly all cases the linear term dominates the quadratic term by at least two orders of magnitude when considering the time between collisions, meaning that the velocity term is much larger than the acceleration multiplied with the time between two collisions.

Another method to determine a possible influence of electrical charges is to analyze deviations from linear trajectories in close approaches of the aggregates. Immediately before a collision two aggregates are so close together that surface charges would cause accelerations or decelerations of the aggregates. Assuming that no charge is being transferred in the collision, the direction (i.e. the sign) of the acceleration should remain unchanged after the collision. If the two aggregates were both charged positively or negatively, the acceleration would point away from their common center of mass before the collision as well as after the collision. If one aggregate was charged positively and the other one negatively, the situation would be reversed and the acceleration would point towards the center of mass both before and after the collision.

The parameters from the quadratic fit for the evaluation of χ^2 mentioned above were used for an evaluation of this. They yield 156 sets of data to investigate a possible change of the direction of acceleration. Considering an angle of up to 30° between the direction of the center of mass and the direction of the acceleration, 25 cases show a reversal, in 14 cases the direction is the same after the collision and in 117 cases the acceleration was not aligned to the direction of the center of mass. Allowing for an even larger angle of 45° between the two direction results in 40 cases of reversal, 20 cases of no change and 96 cases of no alignment. Since the direction of acceleration remains unchanged in only a few cases, it can be concluded that surface charges do not play a role in the motion of the aggregates.

In order to ensure that the parameters were not dominated by those parts of the trajectories where the aggregates were far away from each other, quadratic fits were applied to an increasing number of data points directly before the collision. Since Coulomb's force grows with decreasing distance between the charges, one would expect higher acceleration parameters for the fits to fewer data points. However, there was no evidence for this, no aggregate showed consistently lower accelerations with an increased number of data points, i.e. for a spatially and temporary longer part of the trajectory or for an equally long part that was spatially and temporary further away from the collision.

Nevertheless, the accelerations obtained from the quadratic fits can be used to estimate the number of elementary charges on the surface of the dust aggregates, assuming that they are solely generated by Coulomb's forces. The colliding aggregates are assumed to be charged with an identical number of elementary charges, which can be calculated by

$$q = \sqrt{q_1 \cdot q_2} = \sqrt{4\pi\varepsilon_0 d^2 m a}, \tag{5.5}$$

where ε_0 is the vacuum permittivity, d is the distance between the two charges, $m = m_1 + m_2$ is the mass of the charged aggregates and a is the acceleration. The mass of a typical aggregate is about $7 \cdot 10^{-7}$ kg and a typical value for the acceleration is 0.02 $\mathrm{m\,s^{-2}}$. The latter value was obtained from fits to the last 10 data points, i.e. 20 milliseconds, before a collision occured. With the typical aggregate velocity of about 1 $\mathrm{cm\,s^{-1}}$(cf. Figure 6.1), this corresponds to a distance of 0.2 mm, much less than the diameter of the aggregates. Inserting all values in Equation 5.5 yields $1.6 \cdot 10^6$ elementary charges for a typical aggregate.

The aggregates consist of polydisperse monomers, therefore, calculating the charge per monomer can only be an approximation for a specific monomer size. As a rough estimate, a single monomer radius of 1 μm (this value is in between the median of the monomer size distribution by count and mass, respectively, as found by Kothe et al. (2013)) is used to calculate the number of monomers in a typical dust aggregate, yielding a result of $5 \cdot 10^8$. This amounts to $3 \cdot 10^{-3}$ elementary charges per monomer. Previous works showed comparable values of 0.015 elementary charges per aggregate monomer (Brisset et al. 2016) and $10^6 - 10^9$ elementary charges per aggregate (Kothe 2010). In both cases the aggregates were of a similar material (monodisperse spherical SiO_2 with a diameter of 1.5 μm), but smaller ($10^{-10} - 10^{-7}$ kg, i.e. 30 – 300 μm in radius) than in this work.

Due to SiO_2 being an insulator and any charges most likely coming from triboelectric charging, the number of charges per surface monomer is used to quantify the influence of the charges in this experiment. Assuming the surface filling factor of the monomers to be identical to the volume filling factor of 0.35 yields 2.6 elementary charges per surface monomer if all charges are distributed among the monomers in the outermost layer.. The force exerted by these charges has to be compared to the van der Waals forces that are responsible for the SiO_2 particles (both monomers and aggregates) to stick together.

Following JKR theory (Johnson et al. 1971) the pull-off force between two spherical particles is $F = (3/2)\pi\gamma R$ (see Section 3.1). With $\gamma = 0.037$ J/m^2 (Heim et al. 1999, with a factor of 2 applied to account for the two particles in contact) the force keeping two monomers of 1 μm radius attached to each other is $1.7 \cdot 10^{-7}$ N. The force between two spherical particles with the properties of the aggregates would be $1.9 \cdot 10^{-4}$ N, however, the real contact area between them is reduced by the Hertz factor and the filling factor (Weidling et al. 2012) leading to van der Waals forces as low as $2.9 \cdot 10^{-8}$ N.

The strength of the Coulomb force was estimated using the above numbers for the elementary charges on a surface monomer and those on the whole aggregate, respectively. It is assumed that the charges are concentrated in the center of mass of the aggregate and monomer, respectively, instead of spread over the surface. If the two aggregates or monomers touch physically, the distance between the two charges is then two aggregate or monomer radii, respectively. In this distance, the Coulomb force between two monomers amounts to $3.9 \cdot 10^{-16}$ N and between two aggregates to $4.5 \cdot 10^{-10}$ N.

Comparing these numbers shows that charging effects can be neglected for all further considerations, even when considering the worst case scenario of all charges being accumulated on the surfaces and the van der Waals forces being very low due to the small contact area between the two aggregates.

5.3 Influence of rotation

The analysis methods presented in this work concentrate on the translational energy of the dust aggregates. While visual inspection of the experiments clearly shows rotation to be present, it is very hard to quantify its relative importance. This is due to the fact that in backlight illumination no surface features of the aggregates are visible. Rotation would not be visible at all in perfectly spherical aggregates, but can be observed in ellipsoids. However, the observable change in the projected area is often of the same order as the change due to binarization effects. Additionally, due to the high number density the observation time of an aggregate is often too short to show even one full rotation. This would lead to large errors in the determination of the angular frequency, which could be

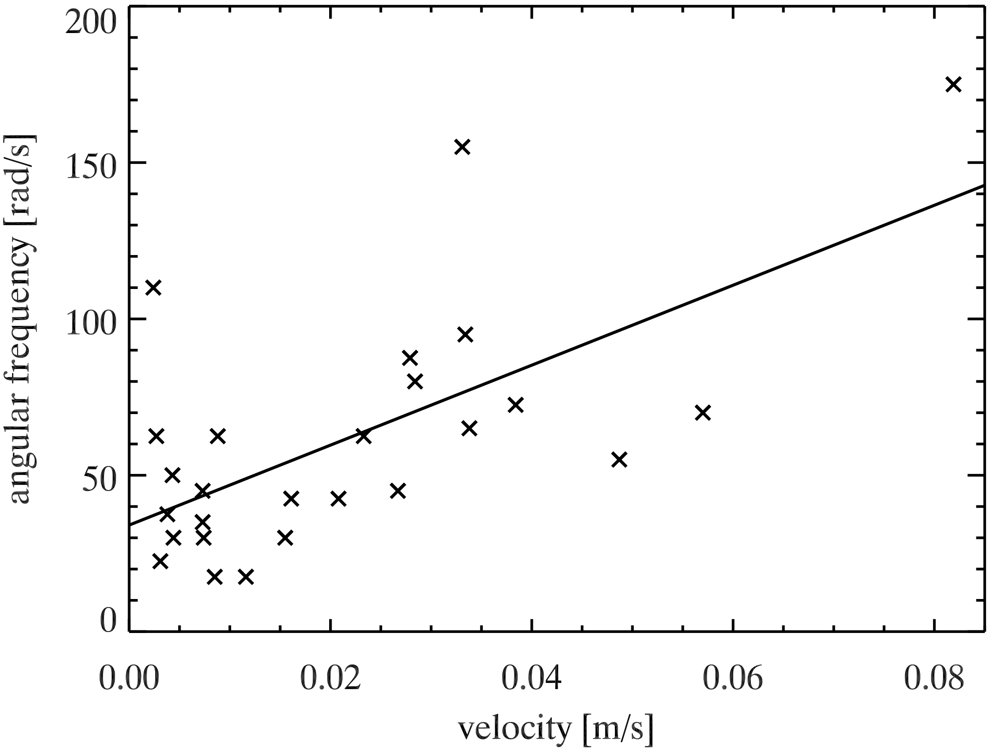

Figure 5.4: The black crosses show the angular frequency of 26 clearly rotating aggregates over their velocity. The solid line is a linear fit and shows an increase of the angular frequency with increasing aggregate velocity.

used to obtain a more precise coefficient of restitution (Schräpler et al. 2012).

Therefore, the effects of rotation were quantified using 26 aggregates whose shape deviated significantly enough from a sphere as to show clear oscillations in projected area and that were visible long enough to observe the effect before other aggregate projections overlapped with the aggregate of interest or collisions changed their velocity and rotational motion. Their angular frequency ω was determined by fitting a sine function to the observed projected area and found to be between 17 and 175 rad s^{-1} (black crosses in Figure 5.4). The velocity v was determined as described in Section 5.1.

Owing to the method of analysis, mostly slow aggregates with a velocity of less than 2.5 cm s^{-1} were investigated. Additionally, the values are biased towards strong rotation, however, for slow- or non-rotating aggregates the rotational energy can be neglected anyway. The solid line in Figure 5.4 represents a linear fit of the obtained values and shows a clear trend of an increased angular frequency with increasing aggregate velocity. This is mainly due to the high values at higher velocities, but it can not be resolved whether these values are a result of the method of analysis, i.e. if only high values for the angular frequency are found. This is possible, since at high velocities a low number of revolutions would need a long distance to be resolved and the aggregate is more likely to collide before that happens than at higher angular velocities.

Visual inspection of the experiment does show a more or less constant level of rotation throughout the experiment, although the velocities decrease with ongoing duration (cf.

Figure 6.1). While the data does show a different trend, it cannot be ruled out that this is an effect of biased choice of data. In conclusion, a correlation between the aggregate velocity and the typical angular velocity can neither be confirmed nor ruled out.

In order to neglect the rotation in the calculation of the coefficient of restitution, the kinetic energy of the aggregate has to dominate the rotational energy. While the same considerations concerning a possible bias apply as above, this comparison gives an idea on how important rotation is.

While the aggregates were clearly ellipsoids, for simplicity a spherical shape was assumed for the determination of the mass m and energies. Since the ratio of the different axes was always smaller than 2 the error introduced by this is small enough to allow for a comparison of rotational and kinetic energies in a meaningful way. The translational energy was calculated as $E_{\mathrm{kin}} = 0.5\ mv^2$ and the rotational energy as $E_{\mathrm{rot}} = 0.5\ I\omega^2$, where $I = 0.4\ mr^2$ is the moment of inertia of a sphere and the radius r is the equivalent radius of a sphere with identical mean projected area.

Figure 5.5 shows the ratio of the two energies as a function of the aggregate velocity. The ratio of the translational to the rotational energy shows that the former is dominating for aggregate velocities above about 1 $\mathrm{cm\,s^{-1}}$, while for lower velocities the rotation can not be neglected. Many aggregates reach velocities lower than that during the experiment (see Figure 6.1). Due to the difficulties in obtaining reliable values for the angular frequency and the ratio of the energies found for the exemplary 26 aggregates and the fact that most analyzed collisions took place at higher velocities (see Figure 6.5) the effect of rotation has been neglected in the following. However, it should be kept in mind that the rotational energy can be important for the slower aggregates.

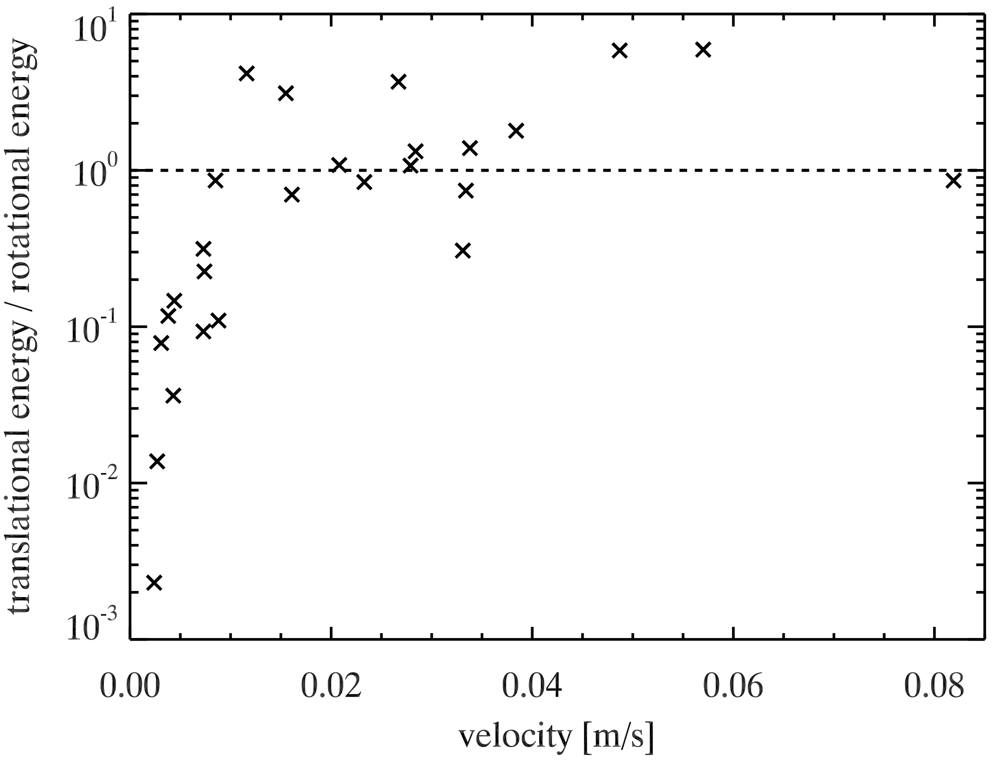

Figure 5.5: This graph shows the ratio of the translational over the rotational energy of 26 clearly rotating aggregates. The dashed line shows a ratio of 1, with data points below it being dominated by the rotational energy and those above by translational energy. For aggregates slower than about 1 cm s^{-1}, rotation can not be neglected. *Reprinted from Icarus, 253, R. Weidling and J. Blum, Free collisions in a microgravity many-particle experiment. IV. – Three-dimensional analysis of collision properties, 31-39, © 2016, with permission from Elsevier.*

6 Results

Numerical simulations rely on experimental data input to be able to recreate the physics of collisions between single dust aggregates as well as to make reliable predictions, for example in global growth simulations. In this chapter the detailed analysis of collisions among dust aggregates of one experimental run from the second drop-tower campaign is presented. Here, dust aggregates with a size of 1 to 1.6 millimeters made up of irregular SiO_2 monomers (see Section 4.3) were used. The shaking velocity was high at the beginning of the experiment and was subsequently decreased after 3 seconds and again after 6 seconds. In Section 6.1, the evolution of the aggregate velocity over the duration of the experiment is presented, followed by a comparison of the results for the velocity, the coefficient of restitution, and the impact parameter when analyzed in 2D versus the results in 3D to shed light on the reliability of experimental data that relied only on two-dimensional information (Section 6.2). In Section 6.3 the results of the collisions with respect to growth and the implications for the growth model is discussed. Lastly, collisions of dimers from several experimental runs and their impact on the further growth process are presented in Section 6.4.

6.1 Velocity evolution

The experiment is based on the fact that collisions of SiO_2-dust aggregates are inelastic (Heißelmann et al. 2007). This means that a part of their kinetic energy is consumed by plastic deformation during a collision. Therefore, the aggregate velocities decrease after each collision with another aggregate – or the experiment walls. Figure 6.1 shows the two-dimensional velocities of all tracked aggregates over time. The orange and blue dots denote aggregates tracked in the left- and right-hand projections, respectively. For aggregates with tracks of more than 60 frames (i.e. 120 milliseconds) of unobstructed movement, the trajectory was split into sections. The velocity is depicted for the point in time in the middle of the considered track.

The two sets of data show the same behavior over time, confirming that the system is homogeneous in x and y direction. As expected, the mean velocity decreases with time. Whilst the aggregates slow down, a few of them start to stick to the glass walls. This can be seen most clearly in the last third of the experiment, when the shaker velocities are of the same order as the aggregate velocities and several aggregates are sticking to the glass walls. The more pronounced double-peak features around 7.4 and 8.7 seconds are a result of the sinusoidal movement of the glass chamber, where the first peaks show the up- and the second peaks the downwards motion of the chamber.

The scatter at low velocities, for example at around 8 seconds, is caused by minute

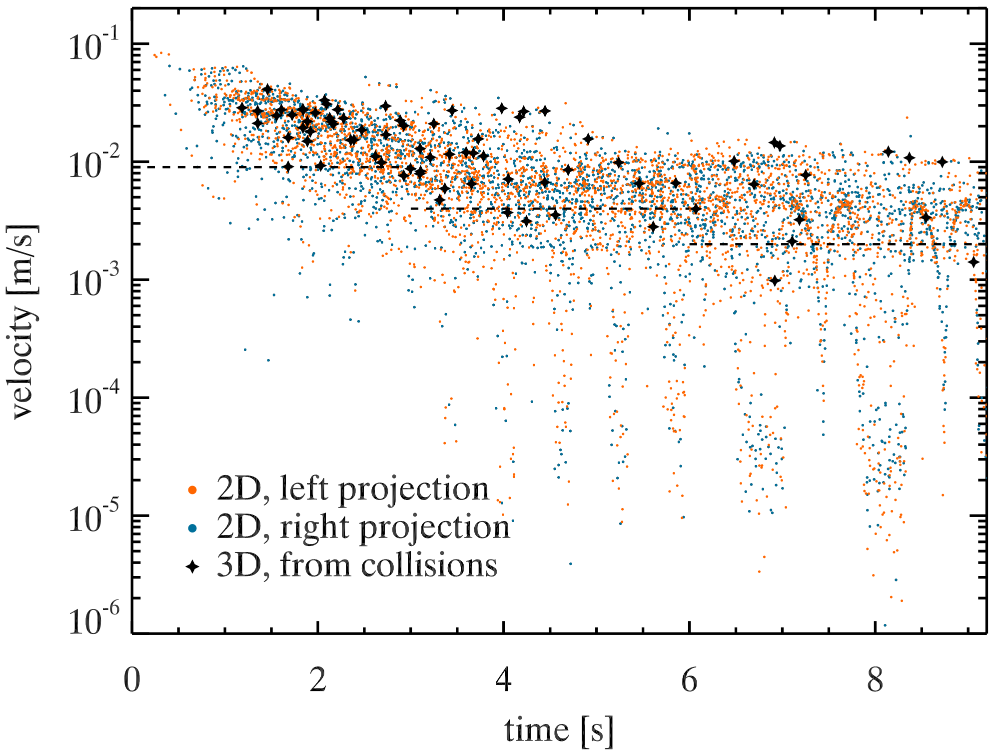

Figure 6.1: The orange and blue dots denote the two-dimensional velocities of all tracked aggregates in the left- and right-hand projections, respectively. The black stars show the three-dimensional velocities of all analyzed collisions. The dashed lines show the calculated maximum velocity of the shaker walls during the three different phases.

movement of the aggregates stuck to the walls. While low aggregate and, therefore, collision velocities are desired in this experiment, collisions with relative velocities below millimeters per second can rarely be analyzed. This is owing to the fact that at low global aggregate velocities many aggregates are already stuck to the walls, where they obscure part of the volume. The moving aggregates, on the other hand, are very slow and, consequently, take a long time to cross any area where their projection is overlapping with that of other aggregates. This makes it very likely that long parts of the trajectory of at least one of the collision partners can not be analyzed and, therefore, the collision as a whole can not be quantified.

The dashed lines in Figure 6.1 give the calculated maximum velocity of the shaking mechanism. The frequency of the shaking was reduced 3 seconds after the beginning of the experiment and again after 6 seconds. While the angular frequency ω of the shaker was 20.8 rad s^{-1} during the first 3 seconds of the experiment, it was then reduced to 10.5 rad s^{-1} and 4.9 rad s^{-1}, respectively. Since the eccentric wheel was in contact with the bottom flange of the chamber only for part of its rotation the sinusoidal motion is just an approximation, as are the frequencies that were deduced by measuring the time between peaks in the position of the lower flange. For a sinusoidal motion these frequencies correspond to a maximum velocity of $9 \cdot 10^{-3}$ m s^{-1}, $4 \cdot 10^{-3}$ m s^{-1}, and $2 \cdot 10^{-3}$ m s^{-1} of the upper and lower flange, respectively. The peak structures in the velocities of aggregates that stuck to the walls indicate that the calculated values are about a factor of 2 lower than the real wall velocities. This is likely due to the form of the eccentric wheel, whose radius increases over less than half the circumference. This, in turn, leads to a deviation from a perfect sinus and results in faster velocities.

In all three phases of shaking, most aggregates are faster than the maximum shaker velocity. Using the shaker in such a manner does not disturb the system much, but can prevent the slower part of the aggregates from getting much slower than the average. The ratio of aggregates sticking to the walls also indicates that the lowest shaking level used here should be the absolute minimum in future experiments, unless the glass walls are coated to reduce their sticking probability. With the current setup, keeping the mean aggregate velocity above a few millimeters per second is mandatory to prevent that all aggregates get stuck on the glass walls. While this means that, even with a longer duration of microgravity, observing collisions far below 1 $\mathrm{mm\,s^{-1}}$ reliably would not work, the statistics at around 1 $\mathrm{mm\,s^{-1}}$ would still increase. Since this is the velocity range where the transition from sticking to bouncing for millimeter-sized aggregates occurs (Güttler et al. 2010, Kothe et al. 2013), it is still worthwhile to conduct this kind of experiment under long-time microgravity conditions.

The black stars in Figure 6.1 give the velocities of those aggregates where a collision was analyzed in 3D. While the three-dimensional velocities are on average higher than the two-dimensional projections (cf. Section 6.2.1), comparison with the two-dimensional velocities of all aggregates shows that the analyzed collisions are a good representation of the events in the particle chamber. The average collision velocity decreases with time down to about one millimeter per second. Quantifiable collisions at velocities lower than that were not found, due to the reasons stated above.

The loss of kinetic energy in each collision is denoted by the coefficient of restitution ε. If the aggregates were behaving as a granular gas with a single coefficient of restitution ε describing the system and the shaking could be neglected, the evolution of the mean velocity would follow Haff's law (Haff 1983):

$$v(t) = \frac{1}{\frac{1}{v_0} + (1-\varepsilon)n\sigma t}, \tag{6.1}$$

where v_0 is the initial velocity, n is the number density and σ is the collisional cross section of the aggregates. Figure 6.2 shows Haff's law as the solid black line plotted over the velocity evolution explained above, with $v_0 = 0.15\ \mathrm{m\,s^{-1}}$ being the measured velocity of the bulk of aggregates at the beginning of the experiment, $\varepsilon = 0.55 \pm 0.26$ being the mean coefficient of restitution found in the analyzed collisions and its standard deviation (see Section 6.2.2), $n = 1.15 \cdot 10^7\ \mathrm{m^{-3}}$ being the average number density in the chamber and the collision cross section $\sigma = 5 \cdot 10^{-6}\ \mathrm{m^2}$ is based on the mean aggregate diameter of 1.3 millimeters. The dashed black lines envelop the area that is given by the uncertainty in the coefficient of restitution.

Comparison with the floating average across 25 velocity values (gray line) shows that Haff's law gives a pretty good estimate for the mean aggregate velocity of the system. This is surprising, considering that Equation 6.1 is idealized and in this experiment the aggregates stick to the walls, the shaker introduces additional energy into the system and the coefficient of restitution can not be described by a single value. However, it indicates that Haff's law can be used to estimate the mean aggregate velocity in this kind

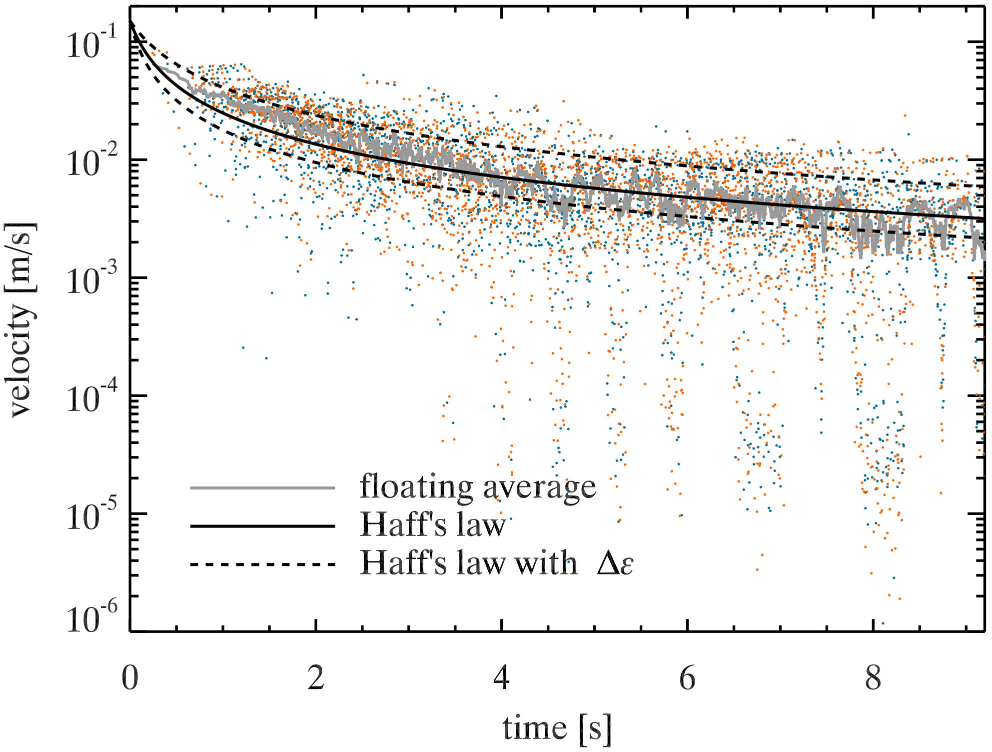

Figure 6.2: This figure shows the velocity evolution of the analyzed experiment. The two-dimensional velocities of all tracked aggregates in the left- and right-hand projections are depicted by the orange and blue dots, respectively, and the solid gray line is the floating average over 25 velocity values. The solid black line shows Haff's law with the measured parameters ($\bar{\varepsilon} = 0.55$) with the dashed black lines giving the range of Haff's law with its standard deviation ($\Delta\varepsilon = 0.26$) added or subtracted to the coefficient of restitution.

of experiment if the shaker velocity is of the same order or less than the mean aggregate velocity.

6.2 Comparison of 2D and 3D analysis

Most quantifiable parameters in a collision show a dependance on the angle of the impact. However, obtaining the full three-dimensional collision information from MEDEA-type experiments is challenging, since the aggregates in question have to be visible in both projections for an extended period of time and the two aggregate projections have to be correlated to one another. Therefore, a three-dimensional analysis requires more time on the one hand and excludes possible events on the other hand because they are only visible in one of the two projections. Thus, analysis would be much faster, if it could be restricted to two dimensions. In this section the values from the three-dimensional analysis of the collision velocity, coefficient of restitution and collision parameter are compared to the values obtained from one projection only.

6.2.1 2D and 3D velocity

The velocity observed in a two-dimensional projection is always a lower boundary for the three-dimensional velocity, since the velocity component in the line of sight can have an arbitrary value but will always add to the total value. For free-floating aggregates with a fixed speed in a microgravity environment, equipartition of the kinetic energy results in random values for the three components of the velocity but with identical mean values. This in turn allows for the deduction of the three-dimensional velocity based on an ensemble of two-dimensional velocities. The mean value of two-dimensional velocities in such a system will on average be a factor of $\sqrt{3/2}$ lower than the true, three-dimensional value.

However, in MEDEA-type experiments it is not clear a priori whether applying this factor to two-dimensional values is a valid means of estimating the three-dimensional values. The dust aggregates have a broad velocity distribution which changes over time (see Figure 6.2). Therefore, a simple statistical approach is not possible, since the effects of randomly visible velocity components and the distribution of the total velocity can not be separated. Also, there is no equipartition of energy in the experiment. Due to the shaker movement in z direction, this velocity component will dominate the others. Since this component is visible in both projections, the correction factor will be between 1 and $\sqrt{3/2}$. In order to find the exact factor, the median values of the x and z components of the velocity are compared for one projection. Additionally, it is assumed that the x and y component of the velocity are identical, which is confirmed by near-identical values of the horizontal component in the two fields of view.

For the MEDEA-II experiment, the velocity components for both projections of all tracked aggregates are shown in Figure 6.3, 3102 data points for each view. The solid and dashed black lines give the distribution of the 1D velocity component in horizontal direction of the left- and right-hand view, respectively. The solid and dashed orange lines depict the respective vertical component. While the distribution for v_z is nearly identical in the two perspectives, there is a slight difference in the horizontal velocity components. Nevertheless, the distributions are still similar enough to assume them to be equal, and as a consequence equipartition of energy is assumed for the x and y direction.

For the left-hand view, the median values (marked by the dotted lines) are $v_{x,l} = 1.5\ \mathrm{mm\,s^{-1}}$ and $v_{z,l} = 4.6\ \mathrm{mm\,s^{-1}}$, which yields a correction factor of $\sqrt{4.6^2 + 2 \cdot 1.5^2} / \sqrt{4.6^2 + 1.5^2} = 1.05$ for the 3D velocity. With the z component being about three times as large as the x component, the factor is very close to 1, since the vastly dominating velocity component is already included in the calculation of the two-dimensional velocity. The differences to the right-hand view are minor. The values obtained here are $v_{x,r} = 1.7\ \mathrm{mm\,s^{-1}}$ and $v_{z,r} = 4.4\ \mathrm{mm\,s^{-1}}$, leading to a factor of 1.06. The three-dimensional velocity could be obtained for too few aggregates to make a reliable statement on whether these factors are correct. A discussion of the obtained results is given below. It can be noted that the known three-dimensional values do not stand out from the distribution of the 2D values (see Figure 6.1), indicating that a factor close to 1 is realistic.

The amount of energy inserted into the system, mainly via the z component of the velocity, was changed over the duration of the experiment. Deriving the median values for each shaking interval and calculating the correction factor shows that while the velocities decrease over time, the distributions are self-similar to those of the complete duration (see

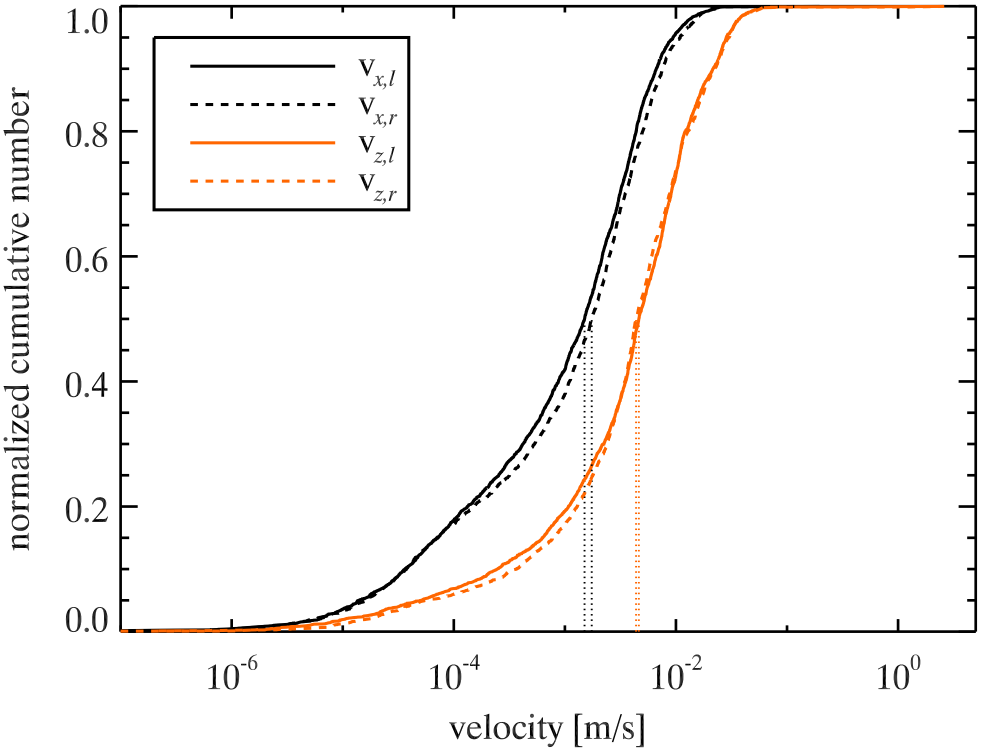

Figure 6.3: The 1D velocity components of all tracked aggregates separated into the two perspectives are shown here. The v_z component is about three times as large as the v_x component. While there is a slight difference in the v_x components between the two perspectives, the distributions are still very similar.

Figure 6.4) and yield similar correction factors, from 1.02 to 1.07 for the two projections and three shaker phases. The solid black, orange and blue lines correspond to the three shaker phases with decreasing shaker velocities, respectively. The median velocities of 16.3 $\mathrm{mm\,s^{-1}}$, 4.1 $\mathrm{mm\,s^{-1}}$, and 2.7 $\mathrm{mm\,s^{-1}}$ (dotted lines) in these phases follow well those of the shaker, with only the first value being a factor of 1.5 higher. This may be a remnant of the high starting velocity of the aggregates or due to the shaker velocities being higher than calculated (see Section 6.1).

In comparison, for one MEDEA-I experiment (cf. Weidling et al. 2012) the median velocities are $v_x = 2.9\ \mathrm{mm\,s^{-1}}$ and $v_z = 4.6\ \mathrm{mm\,s^{-1}}$. This leads to a correction factor of $\sqrt{4.6^2 + 2 \cdot 2.9^2} / \sqrt{4.6^2 + 2.9^2} = 1.13$ in order to obtain the statistical three-dimensional velocities from the 2D values. However, since only one projection has been analyzed in this experiment, no comparison to the real values is possible. The less pronounced prominence of the z component may be a result of the different shaker profile used in this experiment. Here, the shaker was switched off after 1.5 seconds and only the single event of the injected magnet provided an increase in the energy in the z component, while the collisions brought the system gradually closer to an equipartition of energy during the remainder of the experiment. Therefore, the correction factor has to be calculated individually for each experiment.

For the velocities of the aggregates involved in a fully analyzed collision, all compo-

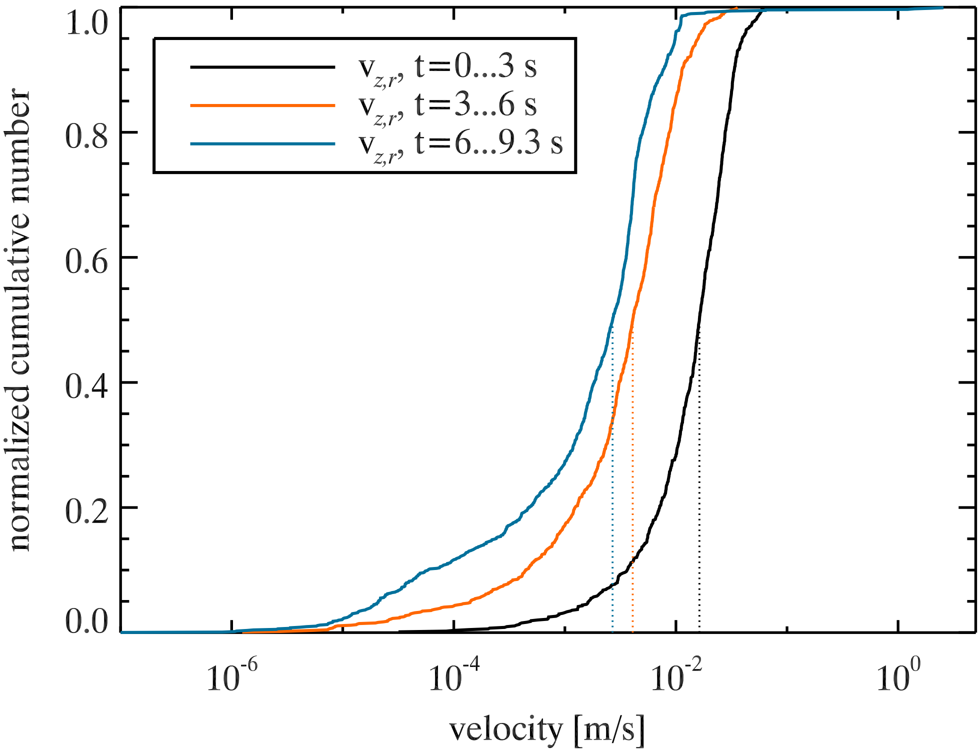

Figure 6.4: This figure shows the distribution of the z component of the velocity in the right-hand view separated into the three shaker phases in solid lines. The dotted lines give the median values, which are close to the respective maximum wall velocities of the shaker.

nents of the velocity are known. For this subset of aggregates in the MEDEA-II experiment a comparison of the 2D and 3D velocities is made in order to evaluate the accuracy of the statistical approach given above. The complete velocity information is available for 43 collisions and is shown as black circles in Figure 6.5. The corresponding two-dimensional relative velocities derived from the two projections are shown as blue crosses and orange pluses in the same rows, respectively. The four collisions leading to sticking are marked by an arrow. Comparing the velocities shows that in most cases the two-dimensional velocities are a good representation of the three-dimensional velocity. However, in 8 out of the 43 cases the two-dimensional velocity obtained from the right-hand projection differed by more than 13% from the 3D value. For the left-hand projection this occurred in 11 collisions. The velocities obtained from the right-hand projection deviate much more strongly than those of the left-hand projection, up to a factor of 2. These differences might be an effect of small-number statistics, since there is no distinct difference between the projections.

In 21 cases one 2D value is higher than the 3D value, which should not be possible by definition. However, the trajectories of the aggregates are not tracked perfectly, which can lead to an overestimation of components of the velocity, which is corrected for by the other projection, if the aggregate was tracked better there. Also, in only 2 of these collisions the higher 2D value differs by more than 5% from the corresponding 3D value.

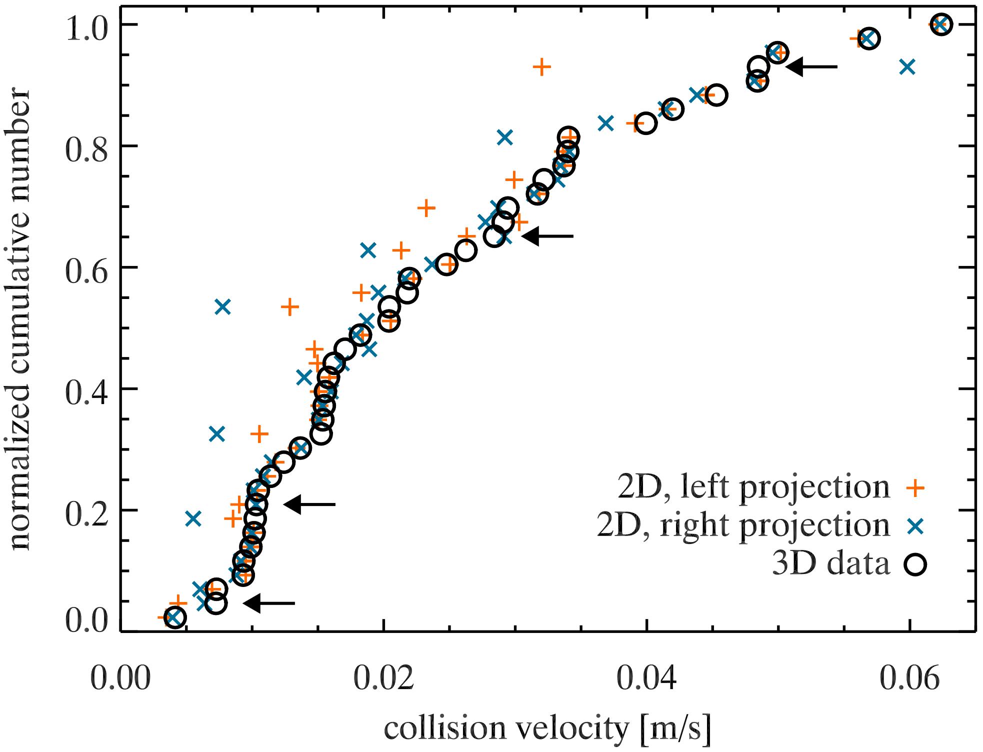

Figure 6.5: This figure shows the three-dimensional collision velocities (black circles) of 43 collisions between dust aggregates. The orange pluses and blue crosses in the same rows mark the corresponding two-dimensional velocities as derived from the left- and right-hand projection, respectively. Collisions resulting in sticking are marked by arrows. *Reprinted from Icarus, 253, R. Weidling and J. Blum, Free collisions in a microgravity many-particle experiment. IV. – Three-dimensional analysis of collision properties, 31-39, © 2016, with permission from Elsevier.*

This is especially apparent in the sticking collision with the highest velocity of 4.8 cm s^{-1}, where one aggregate could only be tracked manually over three images in close succession in the right-hand projection. The fit to these three positions leads to a very high velocity, whereas the more accurate fit to the positions in the left-handed projection indicate a much lower velocity for the components in the x-y-plane. The resulting 3D value will be in between the two 2D values and, while still being higher than the value that is likely correct, less extreme than the higher two-dimensional velocity.

The error of the three-dimensional velocity is typically on the order of a few tenths of a millimeter per second, but can be larger than 1 mm s^{-1}, which is the case in 9 of the collisions. The error is calculated by error propagation from the 1σ uncertainties to the fit parameters, based on a chi-squared test. For the sake of comprehensibility the error bars are not shown in Figure 6.5, but they can be seen in Figure 6.6.

The difference in the ensemble of 2D values can be treated statistically. Comparing the three-dimensional velocities of all bouncing and sticking collisions with the two-dimensional velocities shows the latter to be 9.5% smaller than the mean and 2.1% smaller than the median 3D value. Treating the two projections separately shows a mean reduction of 9.5% and 10.5% of the 2D values compared to the 3D data and a median reduction of 2.1% and 2.0%, respectively. The correction factor of around 1.05 calculated above is well within this range.

Therefore, using a set of velocity data from 2D projections in MEDEA-type experiments yields results very close to those of the full 3D analysis. However, single velocity values may differ significantly due to the stochastic distribution of the kinetic energy into the three components of the velocity. Additionally, this does not hold up if there is no dominant component of the velocity or if the dominant component is not visible in the 2D projection.

6.2.2 2D and 3D coefficient of restitution

The coefficient of restitution ε is an important parameter in collisions. Since it denotes the proportion of velocity lost in the collision, its square directly yields the ratio of kinetic energy conserved in collisions with mass conservation. Thus, the coefficient of restitution is an important parameter in many collision models, like the one by Thornton and Ning (1998), where the rebound velocity is predicted for a given impact velocity. Therefore, experimentally measuring the coefficient of restitution for different collision velocities and fitting the model to this data allows for the deduction of material properties, like Young's modulus or the specific surface energy (cf. Weidling et al. 2012).

Figure 6.6 shows the coefficient of restitution of the 39 analyzed bouncing collisions, which does not appear to have a dependency on the collision velocity. The reason for this is twofold: most analyzed collisions have very similar velocities (cf. Figure 6.5, more than 50% of the collisions occur between 5 and $20 \cdot 10^{-3}\ \mathrm{m\,s^{-1}}$) and the scatter is large, with the median value being $\bar{\varepsilon} = 0.55$ and the values ranging from 0.09 to 1.07. It is likely that the scatter at low velocities is due to the negligence of rotation, which is most important at velocities below about $10^{-2}\ \mathrm{m\,s^{-1}}$ (cf. Section 5.3). The error bars are based on the 1σ uncertainties in the linear fits to the trajectories and calculated by error propagation. Large errors are usually a result of very few data points of the trajectories.

In order to find a possible trend in the coefficient of restitution a linear fit was applied (solid black line). However, it is almost flat and the 1σ range, enveloped by the dotted black lines, shows that the linear trend might go either way. Additionally, the Pearson correlation coefficient being as low as 0.001 means that the fit is not a good representation of the data. Fits of higher order did not yield better results, either. Thus, no prediction for the coefficient of restitution can be made.

The broad scatter of values may be an effect of free collisions with different impact parameters, whereas models usually assume perfectly central collisions. Using only the data from collisions where the aggregates were offset by half a radius at most (i.e. $(b/R)^2 \leq 0.25$) yields slightly different results (orange crosses). Here, a linear fit shows an increase of the coefficient of restitution with increasing collision velocity (solid orange line). Again, the dotted orange lines envelop the 1σ range and show that the spread of possible solutions is still quite large. Due to this, it was not possible to fit the collision model for elastic-plastic adhesive spheres from Thornton and Ning (1998, their Equations 80 and 81) to the data or to any subset or binned version of it. However, the increasing trend for central collisions may indicate that the velocity range investigated here is in between the sticking and the yield velocity of the material.

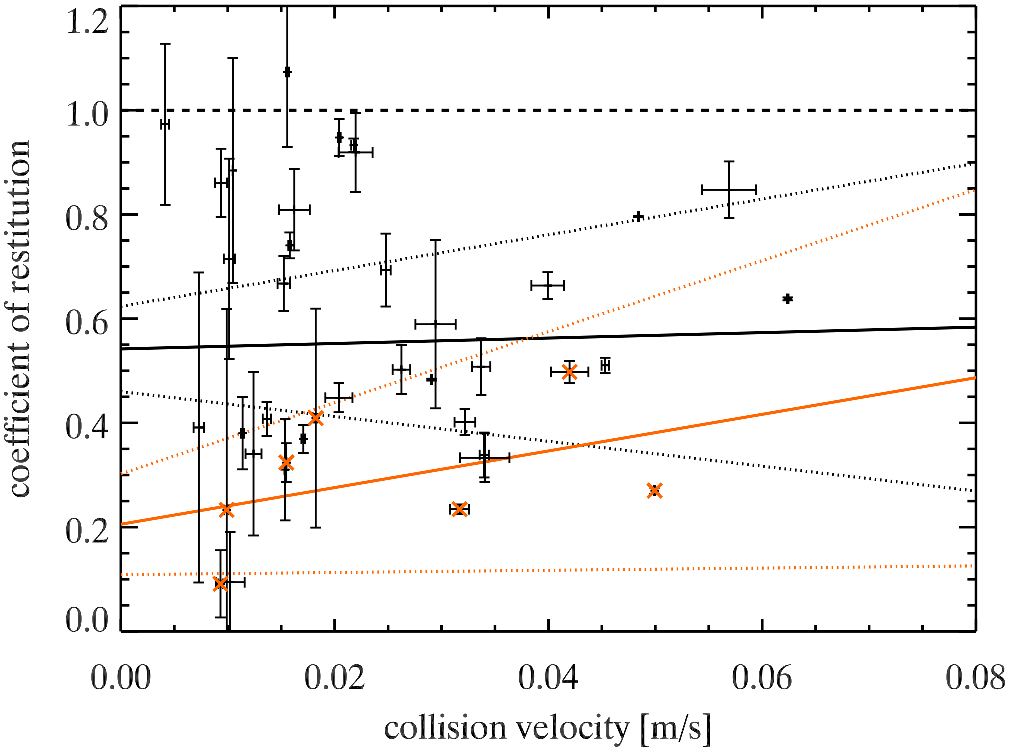

Figure 6.6: This figure shows the coefficient of restitution as a function of the collision velocity of all bouncing collisions as black pluses with the error in both parameters. A linear fit to the data (solid black line, with the 1σ range being enveloped by the dotted lines) confirms that no systematic trend can be made out. Constraining the fit to central collisions (orange crosses, $(b/R)^2 \leq 0.25$) shows an increase (solid orange line), but the error is very large. *Data taken from Weidling and Blum (2015).*

Barring the uncertainty in ε, at least one collision appears to have a coefficient of restitution larger than 1. In theory, the maximum achievable value for a perfectly elastic collision is 1, marked by the dashed black line. However, it can get larger if kinetic energy is gained in a collision. Here, this is possible, when rotational energy is converted into translational energy in the collision, as the rotation of the aggregates is neglected (cf. Section 5.3). Indeed, this collision shows significant rotation before the collision and less after it, but the frequency can not be measured. In order to make precise statements about the collisions using the coefficient of restitution, the rotation has to be taken into account, for example following the approach of Schräpler et al. (2012, their equation 1).

While before the collision the main velocity component is usually visible in the two-dimensional projection, this is not true after the collision, where the aggregates have an arbitrary direction of flight depending on the impact parameter. Therefore, obtaining the three-dimensional information is even more important for the coefficient of restitution. Figure 6.7 shows the 39 three-dimensional values of the coefficient of restitution for the bouncing collisions sorted cumulatively (black circles). The errors are not shown in favor of clarity, but can be taken from Figure 6.6. The orange pluses and blue crosses in the same rows are the corresponding 2D values obtained from the left- and right-hand pro-

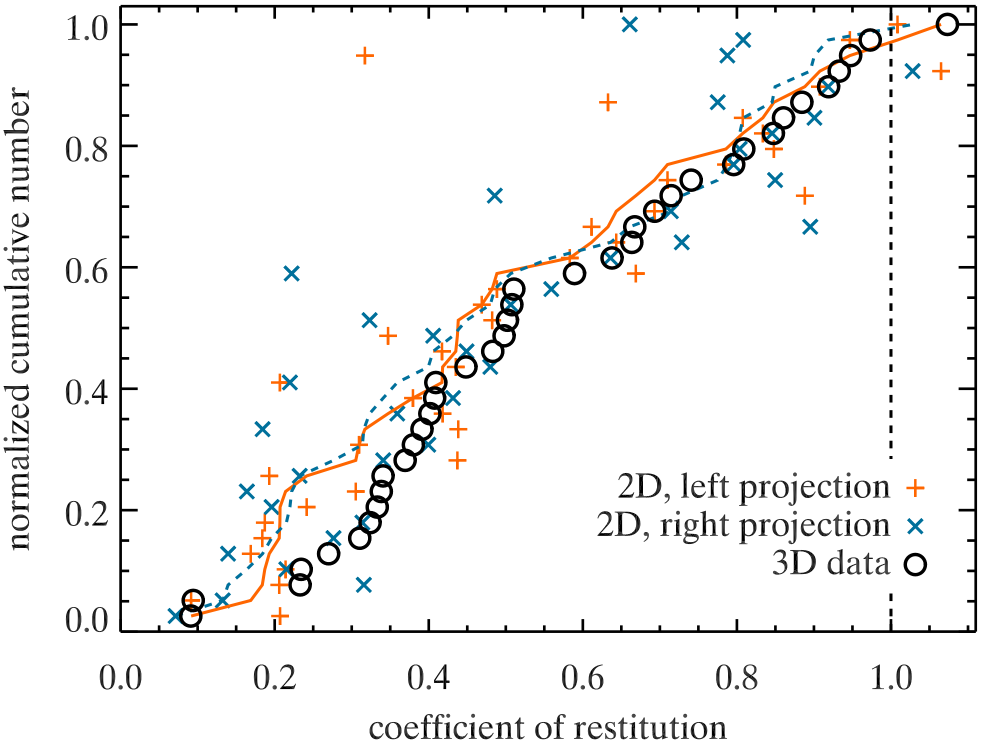

Figure 6.7: The black circles show the three-dimensional coefficient of restitution sorted cumulatively, with the orange pluses and blue crosses in the same rows being the corresponding 2D values from the left- and right-hand projection, respectively. The solid orange and dashed blue lines show the 2D values in a separate cumulative sorting. *Reprinted from Icarus, 253, R. Weidling and J. Blum, Free collisions in a microgravity many-particle experiment. IV. – Three-dimensional analysis of collision properties, 31-39, © 2016, with permission from Elsevier.*

jection, respectively. Again, there are 2D values that are higher than the corresponding 3D values, which is also due to few data points of one of the tracks being corrected for when set off with the second projection. No clear correlation between the 2D values and the corresponding 3D values could be made out. Out of the 39 data points, roughly half of the 2D values deviate by less than 10% from the three-dimensional value, 21 times in the left-hand view and 17 times in the right-hand view. About two-thirds of the two-dimensional values, 28 in the left- and 25 in the right-hand projection, are within 20% of the respective 3D value.

Sorting the 2D values separately yields the cumulative distributions shown as the solid orange and dashed blue line. Surprisingly, these distributions of the 2D values are very similar to the distribution of the 3D value. However, they do show slightly smaller values, another indication for a more isotropic distribution of the velocity after a collision, leading to underestimating the coefficient of restitution in 2D due to apparently smaller velocities after the collision.

Since no trend of the coefficient of restitution could be made out, it is best treated as uniformly distributed in the observed velocity interval, with values of $\varepsilon = 0.55 \pm 0.26$, with the error being the standard deviation of the values. The large scatter is likely a result of neglecting the aggregate rotation as well as irregularities of the aggregates and the collisions being randomly oriented instead of always head-on as assumed in models. However, any real system of dust aggregates in a protoplanetary disk is likely to show the same scatter when undergoing free collisions.

The comparison between the 2D and 3D analysis shows that it is essential to use three-dimensional information to calculate the coefficient of restitution for single collisions. While it is possible for the distribution of coefficients of restitution to appear similar in 2D and 3D, no conclusions should be based on information from a two-dimensional analysis for single collisions.

6.2.3 2D and 3D collision parameter

Obtaining three-dimensional information is crucial for the determination of the collision parameter. A collision that appears to be perfectly central in a two-dimensional projection may in reality be a grazing collision with a much larger impact parameter. Therefore, every 2D impact parameter is only a lower boundary for the true value.

For a system with free collisions, a uniform distribution of the square of the normalized impact parameter $(b/R)^2$ is expected, as the available target area increases with a power of 2 towards the rim of the aggregates' collisional cross section. Therefore, each interval between 0 and 1 for $(b/R)^2$ should contain an equal amount of the total collisions. The distribution for the analyzed experiment is shown in Figure 6.8. The open black circles show the three-dimensional data, with the collisions leading to sticking being marked by an arrow. The orange pluses and blue crosses in the same lines represent the 2D impact parameter from the left- and right-hand projections, respectively. The dashed black line shows a perfect uniform distribution.

While the measured distribution shows a trend similar to a uniform distribution, some intervals are over- and others underrepresented. Collisions with $0.1 < (b/R)^2 < 0.4$ make up only $\sim$15% instead of the expected 30% of all collisions. Then again, grazing collisions with $0.9 < (b/R)^2 < 1$ account for 25%, much more than the anticipated 10%. The remaining intervals are filled by the expected number of collisions. With only 43 collisions analyzed, this distribution represents the expectation for free, random collisions reasonably well.

The overabundance of high impact parameters in the data may be a result of a selection bias. Collisions with a low impact parameter yield a smaller coefficient of restitution than more grazing collisions (see below). Therefore, the velocity after the collision is reduced more strongly and it takes longer for the aggregates to separate again in the projections. This, in turn, increases the likelihood of other aggregates projections overlapping with one of the collision partners in the meantime, making it hard or impossible to obtain the aggregates' trajectories in both projections. For these collisions the impact velocity and outcome can still be obtained, but not the other collision parameters, which require three-dimensional information after the collision. Although the impact parameter only depends on the information before the collision, here, the aggregates' positions at the time of contact can only be calculated using the trajectories both before and after the collision. Thus, it is more likely that all necessary information can be obtained for a grazing collision.

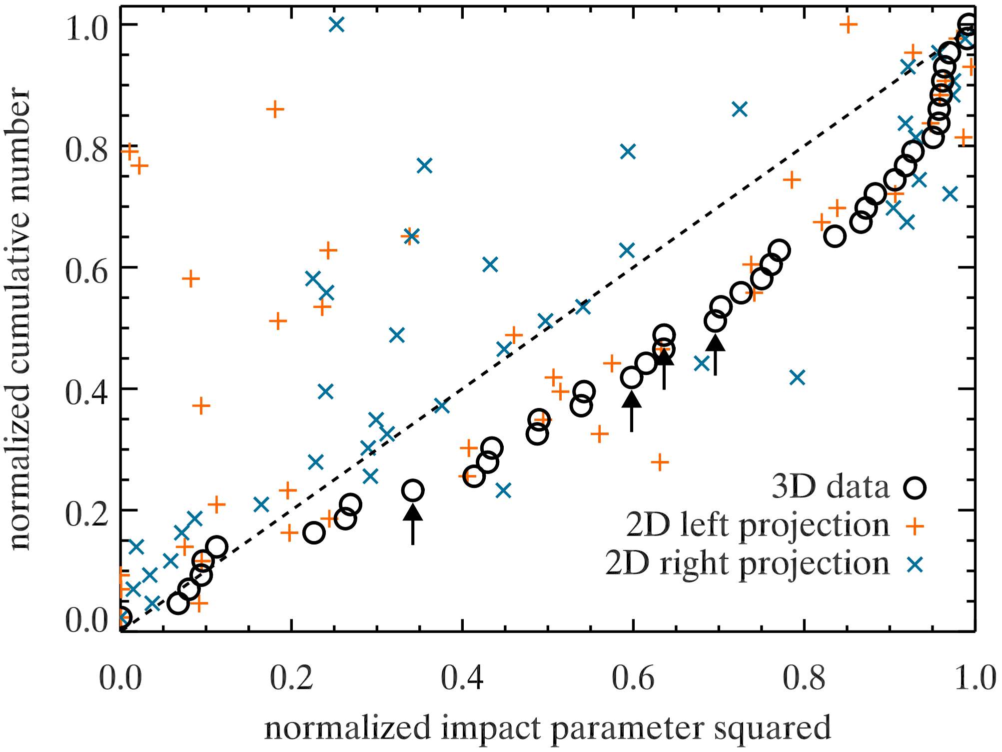

Figure 6.8: The open black circles show the cumulative distribution of the three-dimensional squared normalized impact parameter $(b/R)^2$, which deviates from the expected uniform distribution (dashed black line). The circles marked by an arrow denote the collisions that led to sticking. The orange pluses and blue crosses in the same rows depict the corresponding 2D values from the left- and right-hand projection, respectively. *Reprinted from Icarus, 253, R. Weidling and J. Blum, Free collisions in a microgravity many-particle experiment. IV. – Three-dimensional analysis of collision properties, 31-39, © 2016, with permission from Elsevier.*

The collisions that resulted in sticking do not stand out from the others. The impact parameters of these were 0.58, 0.77, 0.80, and 0.83, neither central nor very grazing. However, they do cluster a little, suggesting that an intermediate impact parameter may be best for sticking to occur.

The significance of a two-dimensionally obtained impact parameter is higher, the higher the impact parameter is. The data shows that some collisions that appear to be central in 2D are actually grazing. Two-dimensional values (orange pluses and blue crosses in Figure 6.8) appearing to be higher than their three-dimensional counterparts can occur for aggregates that deviate significantly from a spherical shape and for very uncertain trajectories. As with the coefficient of restitution, it is very important to obtain the full three-dimensional information if any analysis is to be based on the impact parameter.

Knowledge about the impact parameter also allows for an insight into a possible difference of random collisions compared to only central collisions. This difference is best seen in the loss of energy in the collision, represented by the coefficient of restitution. Figure 6.9 shows the squared coefficient of restitution ε^2 over the square of the normalized

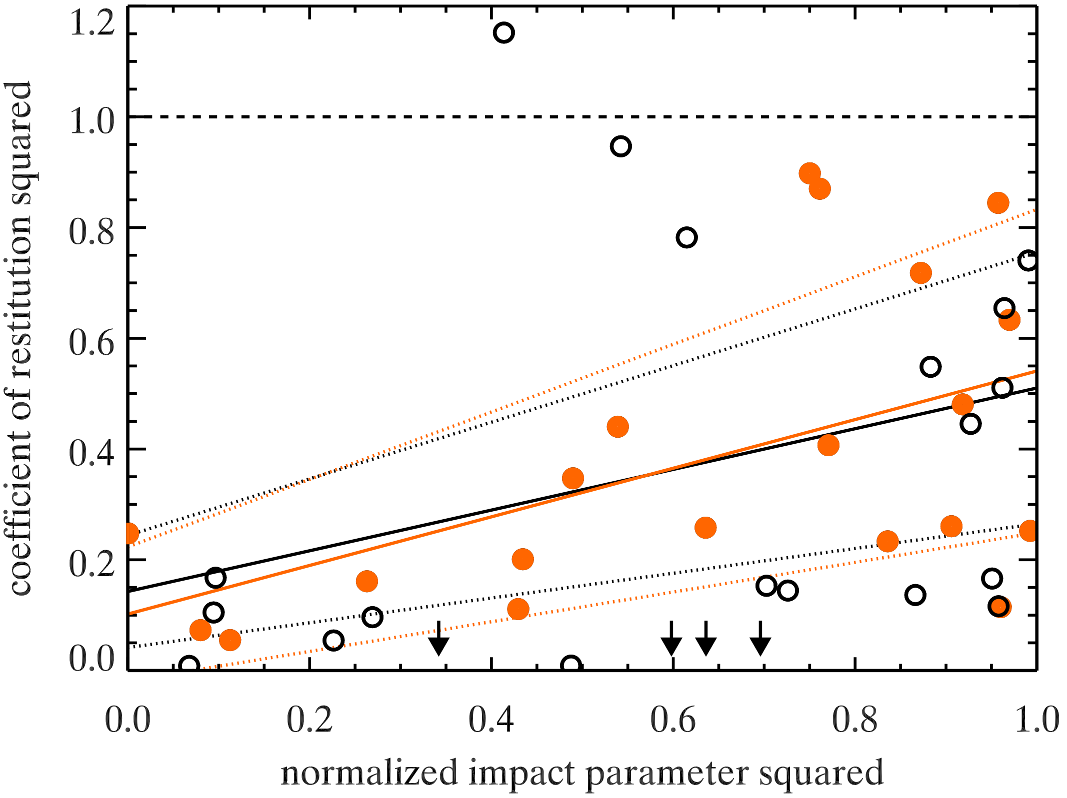

Figure 6.9: This figure shows the squared coefficient of restitution ε^2, a mark for the energy loss in a collision, as a function of the squared normalized impact parameter $(b/R)^2$. The data from collisions with velocities higher than 0.02 $\mathrm{m\,s^{-1}}$ is marked by filled orange circles, that from slower collisions by open black circles. The four sticking collisions are marked by arrows as a reference. A linear fit to all data is given by the solid black line with the 1σ range enveloped by the dotted black lines. The orange line shows the fit only taking into account collisions with a velocity above 0.02 $\mathrm{m\,s^{-1}}$. *Reprinted from Icarus, 253, R. Weidling and J. Blum, Free collisions in a microgravity many-particle experiment. IV. – Three-dimensional analysis of collision properties, 31-39, © 2016, with permission from Elsevier.*

impact parameter $(b/R)^2$. The data is divided into two groups, one with collision velocities below 0.02 $\mathrm{m\,s^{-1}}$ (open black circles) and one above (filled orange circles). This was done in order to check if the rotation of aggregates, which increases the scatter in the coefficient of restitution (cf. Section 6.2.2) and which can be neglected for the group with higher velocities (cf. Section 5.3), influences the relation between the impact parameter and the coefficient of restitution.

The graph shows that the coefficient of restitution rises with increasing impact parameter. Therefore, the ratio of energy lost in the collision is higher the more central a collision is. This is confirmed by linear fits to the data. The solid black line represents the fit to all available data and yields $\varepsilon^2 = 0.14 \pm 0.10$ for perfectly central and $\varepsilon^2 = 0.51 \pm 0.25$ for perfectly grazing collisions. The errors given here are the 1σ errors from a linear least-squares fit and are represented by the dotted black lines.

Table 6.1: Comparison of the dependance of the coefficient of restitution on the impact parameter measured by different experiments. All experimental values are the result of linear fits to data spanning the whole range of impact parameters.

$\varepsilon^2((b/R)^2 = 0)$	$\varepsilon^2((b/R)^2 = 1)$	Material	Source
0.14 ± 0.10	0.51 ± 0.25	SiO_2	this work
0.10 ± 0.12	0.54 ± 0.29	SiO_2	this work, $v > 0.02\ \mathrm{m\,s^{-1}}$
0.12 ± 0.04	0.51 ± 0.12	SiO_2	Weidling et al. (2012), 2D values
0.04 ± 0.03	0.57 ± 0.07	$ZrSiO_4$	Blum and Münch (1993)
0.12 ± 0.02	0.58 ± 0.06	$ZrSiO_4$	Blum and Münch (1993), high mass ratio
0.29 ± 0.03	0.50 ± 0.08	Aerosil	Blum and Münch (1993)
	0.51		Blum and Münch (1993), theoretical

Including only the collisions with velocities larger than $0.02\ \mathrm{m\,s^{-1}}$ (filled orange circles), the values change only slightly, to $\varepsilon^2((b/R)^2 = 0) = 0.10 \pm 0.12$ and $\varepsilon^2(1) = 0.54 \pm 0.29$ (solid orange line with the 1σ-range enveloped by the dotted orange lines). This shows that the increase in the coefficient of restitution is not an effect of rotation being more easily converted into translation for grazing collisions. About 40% more of the initial translational energy is dissipated in central collisions when compared to grazing collisions.

This has also been found in previous work. In Weidling et al. (2012) aggregates of the same material but with a smaller radius were observed two-dimensionally. There, $\varepsilon^2((b/R)^2 = 0) = 0.12 \pm 0.04$ and $\varepsilon^2(1) = 0.51 \pm 0.12$ were found, matching the findings presented in this work.

Blum and Münch (1993) did collision experiments with aggregates made up of Aerosil and $ZrSiO_4$ of about the same size as in this work, but with a lower volume filling factor. They investigated collision velocities from 0.15 to $3.86\ \mathrm{m\,s^{-1}}$, which is higher than observed here. Nevertheless, they found similar results (see Table 6.1 for details). Depending on the material, Blum and Münch found central collisions to yield $\varepsilon^2 = 0.04 \ldots 0.29$ and $\varepsilon^2 = 0.50 \ldots 0.57$ for grazing collisions. They also theoretically derive a value of $\varepsilon^2((b/R)^2 = 1) = 0.51$ with the only assumption being that sliding of the aggregate surfaces is not possible due to roughness, which induces rotation. All experiments with dust aggregates presented above agree very well with this prediction.

The analysis has shown that in order to obtain a meaningful impact parameter, a three-dimensional calculation is mandatory. However, for grazing collisions that already appear as such in 2D, the third dimension may be neglected. This is best seen in the comparison of the coefficient of restitution at perfectly grazing collisions, which was also found using only 2D data.

6.3 Collisional results

The most important aspect of collisions in the context of planet formation is their outcome with respect to the aggregate mass. Whether an aggregate gains mass, loses it or retains its mass governs if this type of collision, i.e. a collision between two aggregates of specific mass, size and material at a given velocity and impact parameter, can lead to aggregate

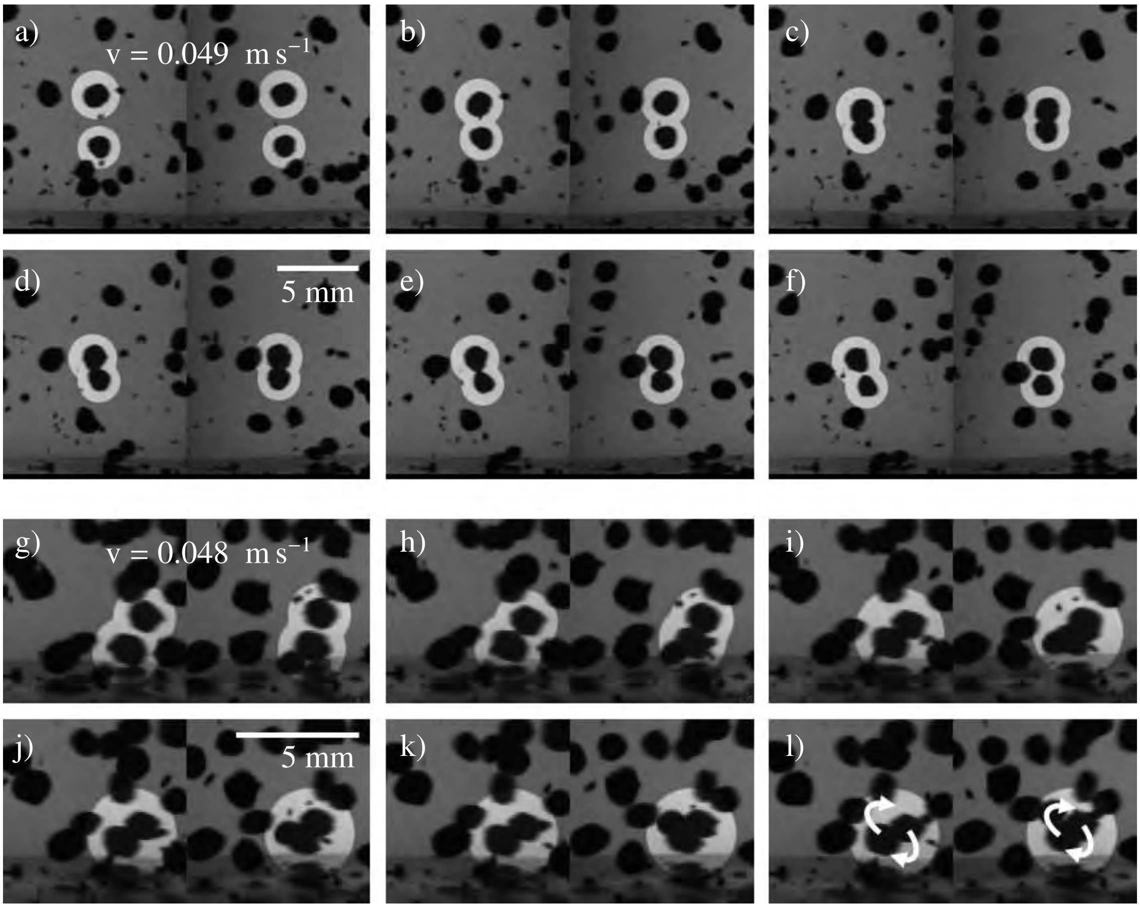

Figure 6.10: a)-f) Image sequence of a bouncing collision with a collision velocity of 0.049 m s^{-1}. The time between two subsequent images is 20 ms. Each image shows the involved aggregates, which are highlighted by the brighter background, from both perspectives. After the collision, the aggregates clearly separate again. g)-l) Image sequence of a collision at 0.048 m s^{-1}, where the two aggregates stick together and revolve around their common center of mass. The temporal spacing between the images is 10 ms.

growth. Since small differences in the composition of the aggregates may change the outcome, the possible results will occur at certain probabilities if averaged over many collisions. One goal of many-particle experiments is to obtain a large number of collisions to be able to compile those statistics.

Figure 6.10 a)-f) shows an exemplary sequence of a collision from both perspectives where two aggregates (highlighted by the lighter background) collide at a velocity of 0.049 m s^{-1} and clearly separate again. This is a perfect example of a bouncing collision. The collision is rather central, with an impact parameter of $(b/R) = 0.28$.

In Figure 6.10 g)-l) the highlighted aggregates collide at an almost identical velocity of 0.048 m s^{-1}. Here, they do not separate after the collision, but instead revolve around their common center of mass, which can be observed a little better in the left-hand view. This is a clear indication for the aggregates to be sticking together. The main difference to the previous collision, which led to bouncing, is the higher impact parameter of $(b/R) = 0.77$. The mass of the involved aggregates is nearly identical.

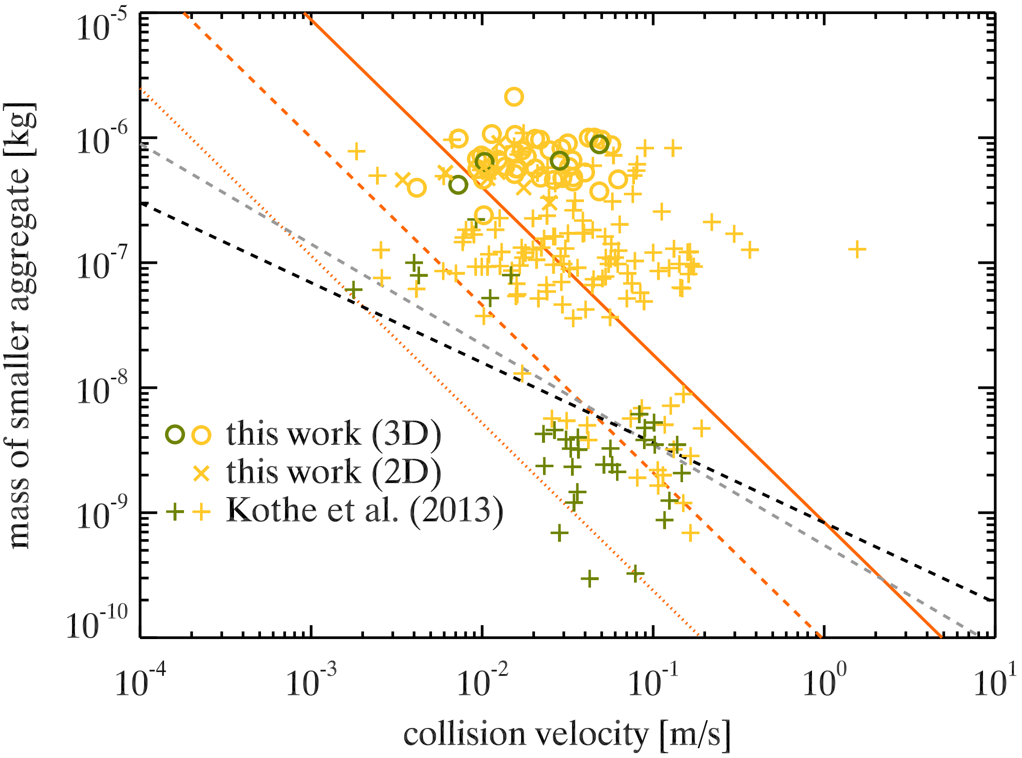

Figure 6.11: This figure shows the collisonal results of the collisions analyzed three- (open circles) and two-dimensionally (crosses) in this work together with the data used by Kothe et al. (2013) to update the collision model (pluses). Green symbols indicate sticking collisions, while yellow ones denote bouncing. The dotted, dashed and solid orange lines show the 100%, 50% and 0% sticking probability from Kothe et al., respectively. The dashed gray line is the result of an SVM fit using the data of Kothe et al. (2013) only, while the dashed black line denotes the SVM fit for all data.

52 free collisions could be analyzed quantitatively in the experimental run presented here. The results are summarized in Figure 6.11. 43 collisions were analyzed three-dimensionally. They are marked by open circles with the four sticking collisions being green, while the 39 bouncing collisions are depicted in yellow. Additionally, nine collisions were analyzed in 2D, where at least one of the aggregates could not be tracked fully in one of the projections. They all resulted in bouncing and are represented by yellow crosses.

The orange lines give the sticking probabilities as determined by Kothe et al. (2013, asymmetric least-squares fit), from always sticking (dotted line) over 50% each sticking and bouncing (dashed) to always bouncing (solid). These fits are based on the data given by the green and yellow pluses, which denote sticking and bouncing collisions, respectively. The cloud of data points at low masses was analyzed in that work directly, while the higher mass data is from Weidling et al. (2012). Both are MEDEA-type experiments and were analyzed two-dimensionally.

Three of the four sticking collisions analyzed in this work occurred at velocities where the growth model previously predicted sticking to be impossible. The difference in veloc-

Table 6.2: Fit parameters for the power law given in Equation 6.2 using different fit methods and data points. The three columns on the left-hand side give the parameters when only the data in Kothe et al. (2013) is fitted, those on the right-hand side are the results of fits to all available data points. The lines give the parameters for the fit methods presented in the text, with the first one being the fit presented by Kothe et al. (2013).

	only data from Kothe et al. (2013)			all data		
method of fit	s	a	w	s	a	w
asymmetric least squares	-1.34	-10.02	1.42			
support vector machine	-0.80	-9.26	> 2.6	-0.64	-9.08	> 4.3
probit model, linear	-0.80	-9.47	2.46	-0.36	-9.54	6.17
probit model, quadratic	-0.99	-9.61	2.49	-0.75	-9.44	5.27

ity is definitely higher than can be accounted for by the fit being based on 2D velocities. Therefore, the model has to be updated, taking the new data into account. However, using the same fit procedure as Kothe et al. (2013) did not yield a result. With the addition of the new data points, bouncing collisions are sampled much more than sticking collisions. For the fit function to find the transition between sticking and bouncing, both results have to be sampled in similar quantities.

In order to update the sticking-bouncing transition with the new data quantitatively, two different mathematical methods were used. The first is the so-called support vector machine (SVM), a method similar to the one used by Kothe et al. (2013). For two-dimensional data it can be used to classify data by finding the dividing line between the groups of data. This is done in such a way as to maximize the distance of the data points closest to the line from the line itself. If the two groups of data can not be separated cleanly, as is the case with the data here, the dividing line is chosen so as to minimize the sum of the distances of the data points on the wrong side of the divider from the divider itself. Since this balances the data points on the wrong side of the line, this is equivalent to the line where half of the collisions lead to sticking and the other half result in bouncing.

Here, the MATLAB-internal SVM function was used to find the results. A power law of the form

$$\log\left(\frac{m}{1\mathrm{kg}}\right) = s \cdot \log\left(\frac{v}{1\mathrm{m/s}}\right) + a \tag{6.2}$$

was used as input, with s and a being the parameters fitted by the SVM function. Here, s is the exponent of the power law (or slope in the $\log(m)$-$\log(v)$-diagram) and a is the logarithm of the mass in kilograms at $v = 1\ \mathrm{m\,s^{-1}}$. The dashed gray line in Figure 6.11 shows the result of the fit using only the data by Kothe et al. (2013). It results in a much flatter slope of only -0.80 compared to the -1.34 of Kothe et al. Using the SVM method to fit all data, including the collisions presented in this work, results in the dashed black line. It has a slope of only -0.64 due to the larger amount of bouncing collisions at low masses than sticking collisions at high masses. The fit parameters are summarized in Table 6.2.

Clearly, the width of the transition zone would have to be very large to encompass the newfound sticking events. However, the SVM method does not intrinsically yield a value for that. If the sticking collision farthest from this line is used as an estimate for the position of the 0% sticking probability line, the zone has to have a width of at least 4.3 orders of magnitude in mass. Keeping in mind the constraints on the validity of this velocity from the velocity analysis (cf. Section 6.2.1), this value might shift accordingly.

In order to get exact numbers, a second method to find the parameters of the transition was used, which also yields parameters for the width of the zone. The probit model also is a binary classification method, used to find the boundary between two classes of data. In contrast to a linear regression method, values are weighted with their probability when computing the goodness of fit. This allows for the definition of a transition zone where the two results are following a predefined probability distribution. In order to always find the global minimum in the optimization of the error, this distribution has to be monotone.

Again, a power law of the same form given in Equation 6.2 is used to fit the 50% sticking line. As in previous works, it is assumed that the 100% sticking and 0% sticking lines are also power laws with the same slope (i.e. parallel to the 50% line). For the sticking probability distribution perpendicular to the 50% line, a linear decrease in the $\log(m)$-$\log(v)$-parameter space was assumed, i.e. parallel lines with a given spacing represent an identical change of the sticking probability everywhere within the transition zone. The width of the transition zone w is not predetermined, but an additional fit parameter. It gives the difference in a between the 100% and 0% sticking lines, with the 50% line being right in the middle.

Using this method to fit the data given in Kothe et al. (2013) yields a transition line very similar to the SVM result (see Table 6.2). With the slope being much flatter than predicted by Kothe et al., the width of the transition zone is one order of magnitude broader in mass. Using this method to fit all data results in a very different picture. It yields a slope of only -0.36, whereas the transition region is very broad, spanning more than 6 orders of magnitude in mass. With other experimental results in mind, which are included in e.g. Güttler et al. (2010), this result seems to be physically unrealistic.

Since it is not clear if the sticking probability decreases linearly in the $\log(m)$-$\log(v)$-parameter space, a quadratic gradient was also fitted. The fitting parameter q was chosen in such a way as to yield a sticking probability of $p_{\text{stick}} = 0.5$ for $q = 0$. The following gradient was used:

$$p_{\text{stick}} = \begin{cases} 0 & , q < -0.5 \\ 2(q+0.5)^2 & , q \in [-0.5, 0] \\ 1 - 2(q-0.5)^2 & , q \in [0, 0.5] \\ 1 & , q > 0.5 \end{cases} \tag{6.3}$$

The resulting fit of the data in Kothe et al. (2013) is more similar to their fit than with the linear probability distribution, although it also has a flatter slope with $s = 0.99$ and broader transition zone with $w = 2.49$. This fit is shown as the gray lines in Figure 6.12. The dotted, dashed, and solid lines denote 100%, 50%, and 0% sticking probability, respectively. Again, including the collisions presented in this work results in a flattening of the slope and a broadening of the transition zone, but it is not as pronounced as with the linear probability gradient. The fit yields a slope of $s = 0.75$ and the transition zone has a width of $w = 5.27$ orders of magnitude in mass. Figure 6.12 shows this fit as the black lines. The fit parameters are also presented in Table 6.2.

All fits presented in this work have a similar value for a, resulting in a 50% sticking probability for aggregates with a mass of around $3 \cdot 10^{-10}$ kg at a velocity of 1 m s^{-1}. This corresponds to an aggregate diameter of 80 μm, assuming a volume filling factor of 0.35. The fit by Kothe et al. (2013) predicts a lower mass having a 50% sticking probability at this velocity. No experiments have been performed for porous aggregates of this size

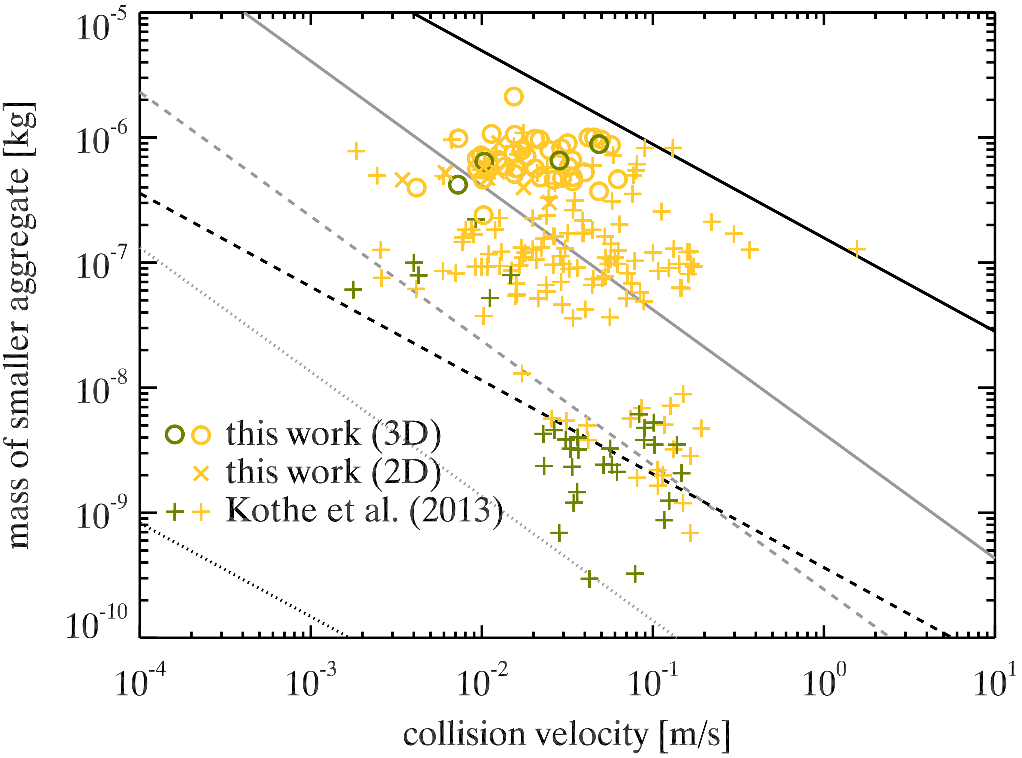

Figure 6.12: The data points for sticking and bouncing are identical to Figure 6.11. The gray lines give the fit of the probit model with a quadratic gradient of the probability distribution to the data from Kothe et al. (2013, yellow and green pluses). The black lines give the fit for all data. 100%, 50%, and 0% sticking probability is marked by the dotted, dashed, and solid lines, respectively.

yet. Without further experiments no statement can be made, which of the presented fit methods matches the results best. With data from experiments with aggregates of about 100 μm in diameter at velocities around 1 $\mathrm{m\,s^{-1}}$ and at velocities at or below 1 $\mathrm{mm\,s^{-1}}$ for millimeter-sized aggregates, the parameters of the transition zone can be constrained much better. Both kinds of experiments are possible with the MEDEA experiment.

If the slopes of the transition zone are really very flat and valid for the whole range of possible masses, this leads to an interesting characteristic for very small aggregates. Depending on the exact slope, aggregates smaller than a certain size will never bounce off each other in collisions. For them, the model predicts sticking to directly turn into fragmentation. For slightly bigger aggregates, there will be a velocity range where they bounce off with a certain probability, but none where they will always bounce.

Brisset et al. (2016) found perfect sticking up to 0.12 $\mathrm{m\,s^{-1}}$ for aggregates with a mass of about $1.6 \cdot 10^{-8}$ kg, which would be approximately in the middle of all fitted versions of the transition zone, including the fit by Kothe et al. (2013). They also found the probability for sticking to fall much more rapidly and measured a sticking probability of less than 5% for velocities larger than 0.13 $\mathrm{m\,s^{-1}}$. However, they did not observe single collisions, but the clustering behavior of an ensemble of aggregates. Therefore, no single data points from this experiment can be included in this analysis and it is unclear how much weight this measurement of the transition velocity has when compared to the single collisions analyzed here. However, it might be an indication that the assumption of an identical width of the transition zone for all masses is wrong. Without additional experiments that map the whole transition zone for several masses, this can not yet be verified, though.

6.4 Collisions between dimers and monomers

While it is important to be able to predict the outcome of a collision between two aggregates, it is of equal importance to know what happens with the aggregates in subsequent collisions to understand the full growth process. Thus, the experimental run discussed above as well as four others from the MEDEA-II and -III drop-tower campaigns with aggregate sizes of either 0.5 – 1 mm or also 1 – 1.6 mm were searched visually for dimers and their formation and collisions were analyzed where possible. A total of 55 dimers were found, which were involved in 68 collisions with other aggregates or the glass walls. However, since many dimers were observed in experiments with the quasi-2D insets where high number densities were used, for most of these events the results could only be observed but not analyzed quantitatively due to too many overlapping projections of other aggregates.

An example of a collision between a dimer and a monomer is shown in Figure 6.13. The monomer (coming from the bottom) collides with the dimer (from the top, rotating counterclockwise) in image c) at a velocity of 0.015 $\mathrm{m\,s^{-1}}$. In the last image, both have clearly separated again. The dimer is still intact and has gained rotational energy, as the monomer collides with the right part of the dimer. After the depicted collision, the dimer survives a subsequent collision with the wall and remains visible for the remainder of the experiment, which lasted for another 3 seconds.

Of the 55 dimers, the formation is visible in 24 cases, while the remaining 31 dimers emerge from regions of high optical depth and it is unclear whether they formed by a collision during the experiment or stuck together when lying on the bottom flange prior to the start of the experiment. However, just one formation sequence could be analyzed quantitatively, it is the sticking collision at 4.8 $\mathrm{cm\,s^{-1}}$ shown in the previous section. Whether the formation could be observed or not did not have a detectable influence on the result of the collisions.

About half the collisions of monomers with the dimers could be analyzed quantitatively. The results are summarized in Figure 6.14. The 5 collisions where the dimer was destroyed in the collision are marked by arrows. The blue crosses mark the mass of the monomer and the orange pluses represent the mass of the dimer, respectively. In 6 of the collisions, the monomer was more massive than the dimer. For the calculation of the dimer mass it was assumed that it is made up of two equally-sized aggregates that are fully visible in the image with the highest pixel count for the cross section.

There are too few data points to give a clear boundary at which fragmentation sets it, since the mass of the involved aggregates may also play a role. However, it is noticeable that only collisions at velocities above 1 $\mathrm{cm\,s^{-1}}$ led to fragmentation. In one third (5 out of 14) of the collisions above this velocity, the dimer was destroyed, while it always (5 out of 5) remained intact at lower velocities.

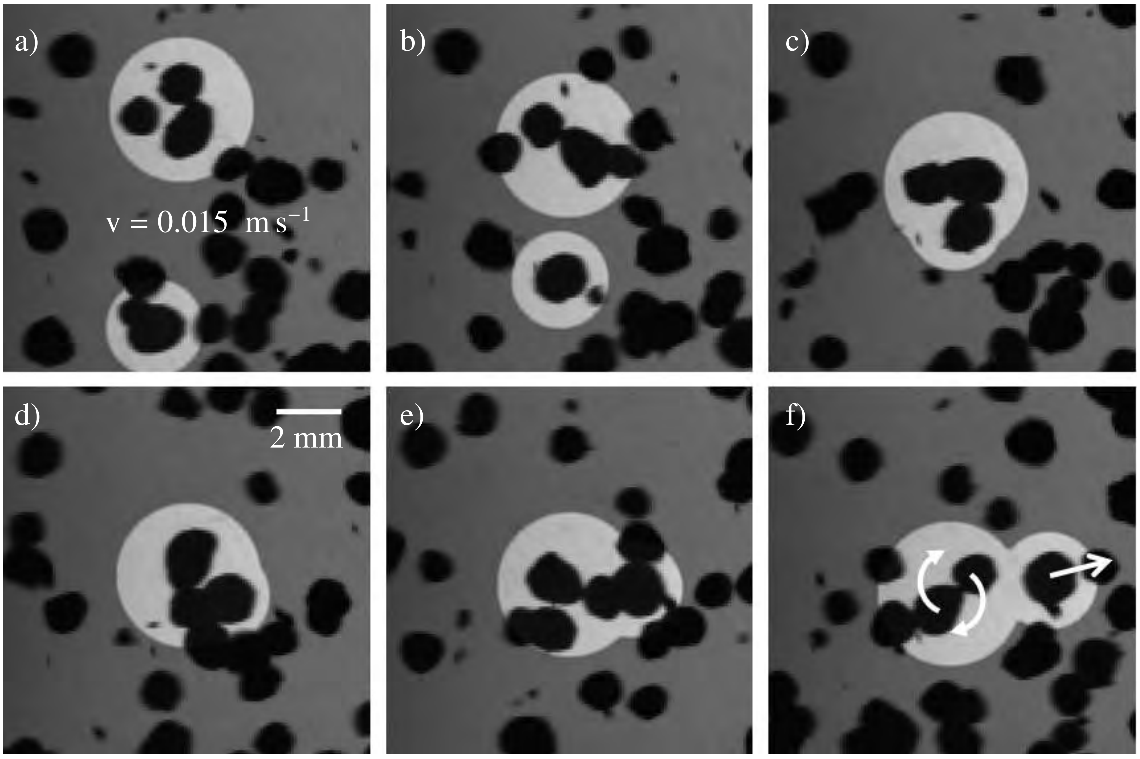

Figure 6.13: Exemplary image sequence of a dimer colliding with a monomer at 0.015 m s^{-1}. After they separate again, the parts of the dimer still revolve around their common center of mass, indicating that they still stick together. The time between two subsequent images is 102 ms.

The data from 24 other collisions of monomers with the dimers could not be obtained. Of these, the dimer remained intact in 9 cases and was destroyed in 14 cases. In total, this makes 23 cases of bouncing and 19 cases of fragmentation. In another observed event, the dimer was destroyed in the collision, but the monomer stuck to the aggregate it had collided with, forming a new dimer.

Collisions with the walls could never be analyzed quantitatively, since this would always require full three-dimensional information, which was not obtainable for any dimer. Of the 25 observed collisions with walls, the dimer survived intact 16 times and was destroyed in 9 cases.

No case of a monomer sticking to a dimer was observed. However, one formation of a larger cluster, consisting of 5 monomers, was found. A dimer is colliding with a trimer and sticking to it. The formation of both structures is not visible, they emerge from a dense cloud of aggregates at the top of the vacuum chamber. They collide at a velocity of 1.1 mm s^{-1} and stick together. The resulting chain of aggregates does not collide with other aggregates afterwards. After about 3.5 seconds it disappears in an optically thick cloud of aggregates and cannot be observed further before the experiment ends.

Based on the observations in the velocity interval between 1 millimeter and 10 centimeters per second presented above it is therefore about as likely for a dimer to be destroyed in a collision as it is for it to remain intact. Kelling et al. (2014) and Kruss et al. (2016) conducted experiments with aggregates made up out of the same monomers, with

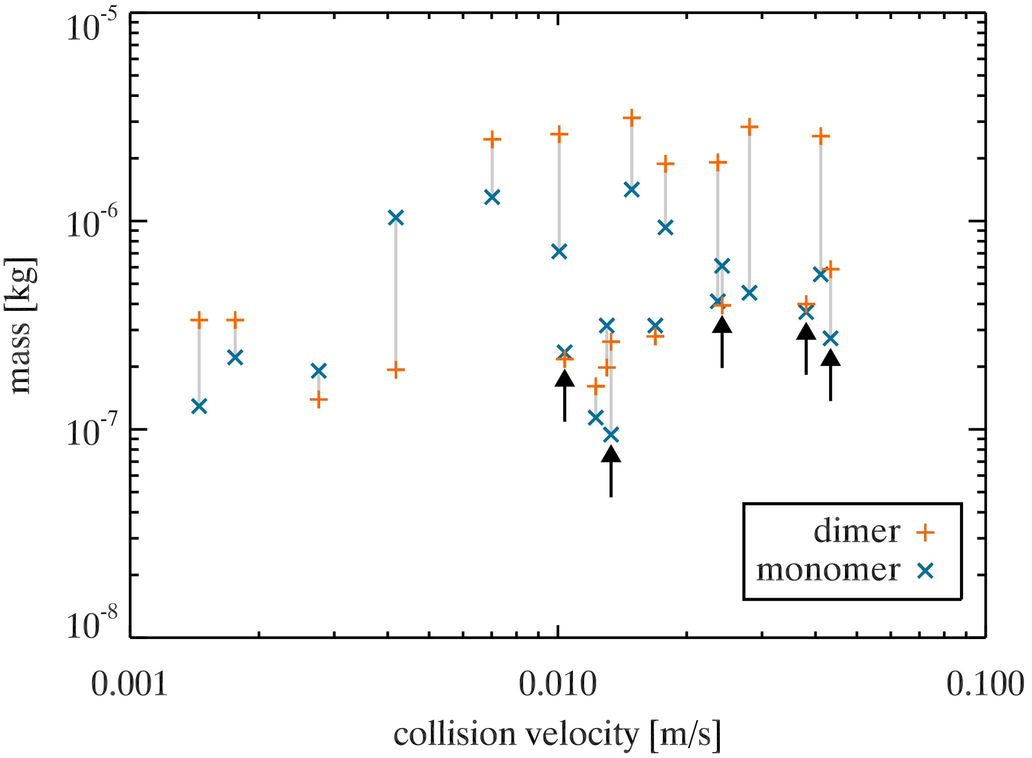

Figure 6.14: This figure shows all quantifiable collisions of dimers with monomers. The mass of the dimer is given by the orange pluses, while the mass of the monomer is given by the blue crosses. The two values that belong to one collision are connected by a gray line. In the collisions marked by arrows the dimers were destroyed in the collision, while they remained intact in all other cases.

similar aggregate sizes and at the same velocity interval. The most noticeable difference is that their aggregates are flat, collide in a quasi-2D plane and are being levitated by the Knudsen effect. They observed 10^5 and 899 collisions, respectively. Both works observe sticking between aggregates, however, all clusters are destroyed eventually, leading to zero net growth. The lifetimes of the dimers observed by Kelling et al. (2014, their Figure 10) is on the order of a few tens of milliseconds. With about 1500 collisions observed per aggregate over the course of 900 seconds, the average time between collisions is 600 ms. With only 2 dimers having lifetimes longer than that it is very likely that the dimers observed by them break apart in the collision subsequent to the one that formed them, resulting in a fragmentation probability of 1 or very close to it.

Using the same experimental setup, Jankowski et al. (2012) observed collisions between millimeter-sized aggregates which were made up of basalt that had a larger monomer size of up to 25 μm. These aggregates were very compact, with a filling factor of about 0.5. In the velocity range of 0.1 to 15 cm s^{-1} they found about one third of the collisions to lead to sticking. Clusters formed in this way are destroyed only in one in five subsequent collisions, which may open the way for some clusters to grow big enough for growth via mass transfer to occur.

A possible explanation for the observed difference in fragmentation probability is that the aggregates in the experiment discussed here are spheres instead of disks. Therefore, they have a higher mass and, at identical collision velocities, a higher momentum. This, in turn, can lead to a higher indentation by deformation upon collision, increasing the contact area and forming a more resistant contact between the two aggregates.

If dimers made up of millimeter-sized aggregates would always be destroyed in subsequent collisions, this would put severe restrictions to the way that planetesimals can form. Further direct growth would be prevented and dust aggregates would have to grow further by collective mechanisms such as the streaming instability (e.g. Johansen et al. 2007). However, since the aggregates are so small and the streaming instability works best at Stokes numbers of around 1, this would most likely only work in the outer parts of the protoplanetary disk.

There are two other ways that allow for growth beyond millimeter-sizes. One is that at slightly lower collision velocities the chance for fragmentation of dimers decreases while the chance for monomers sticking to it increases. Depending on the exact properties of the gas in the disk, velocities at or below one millimeter per second are realistic and might yield the desired outcome. With the fragmentation probability of 50% found in the experiments presented here, another option is for some "lucky winners" to not only survive subsequent collisions, but grow through direct sticking, either in a low-probability event or at a lower velocity. These "lucky winners" would quickly reach a size where they could grow via mass transfer, i.e. the colliding monomer is destroyed, but a fraction of its mass sticks to the larger cluster. This way, centimeter sizes can be reached (Windmark et al. 2012a, Drążkowska et al. 2014), which are more likely to subsequently trigger the streaming instability (e.g. Wahlberg Jansson and Johansen 2014). However, Krijt et al. (2015) show that erosion can stop the growth of aggregates. Whether growth of aggregates by mass transfer, where many monomers are generated that could erode larger bodies, is more efficient than erosion remains an open question.

7 Conclusion and Outlook

The MEDEA setup presented in Chapter 4 is suitable for generating collisions between dust aggregates at velocities of a few millimeters to centimeters per second under microgravity conditions. For the first time, low-velocity collisions of dust aggregates with a diameter of 1 to 1.6 mm were analyzed. The results help in understanding the transition from sticking to bouncing. Especially the sticking collision at a velocity of 0.048 $\mathrm{m\,s^{-1}}$ (see Figure 6.11) shows that the transition zone, where both sticking and bouncing can occur, may be much broader than assumed previously. However, the difference in results when fitting the transition zone with different models also reveals that more experimental work is necessary to better understand this process (cf. Section 6.3). Nevertheless, the results support the findings from Kothe et al. (2013) in that the slope of the transition is likely much less steep than in the first collision model by Güttler et al. (2010).

In the future, experiments at velocities of 0.1 to 1 $\mathrm{m\,s^{-1}}$ should be performed with dust aggregates with diameters of about 250 μm. Additionally, experiments should be performed with millimeter-sized dust aggregates to investigate the collisional results at velocities around 1 $\mathrm{mm\,s^{-1}}$. Together, these clouds of data points will help to anchor the fits for the transition zone as well as give insight into a possible change of the width with changing aggregate mass.

The MEDEA setup is suited to perform both sets of experiments. For the smaller aggregates, short-term microgravity like in the drop tower should be sufficient. Changing the motor to one with a higher motor speed or gear ratio will lead to collisions in the desired velocity range. For the low-velocity collisions of millimeter-sized aggregates, long-term microgravity is required to increase the probability of collisions happening at velocities below the shaking velocity. A method that allows for an effective coating of the particle chambers, preventing the sticking of aggregates while allowing for visual observation, would improve the odds for collisions at those velocities to occur. These experiments would also increase the statistics for collisions of dimers formed in free collisions. While aggregates with a diameter of a few hundred micrometers cluster very effectively (e.g. Kothe et al. 2013, Brisset et al. 2016), it is yet unclear if millimeter-sized aggregates grow beyond the dimer stage (cf. Section 6.4).

In this work, the two- and three-dimensional analysis of collisions in the MEDEA setup are compared. The results presented in Section 6.2 show that the velocities of an ensemble of collisions are reasonably similar when using only 2D data. While the velocity for any single collision may be much lower than the actual value, the median correction factor found in Section 6.2.1 was only 1.05 to 1.06. Thus, if the parameters of the collision are to be used to update the collision model, a two-dimensional analysis is usually sufficient. This also shows that the results of many previous works, which have been analyzed in 2D, are still valid and can be used for the collision model.

If the coefficient of restitution or the impact parameter is of interest, a full three-dimensional analysis is required, though. These parameters are essential to get a better understanding of the microphysics of collisions of porous, adhesive aggregates. While several models like the JKR theory (Johnson et al. 1971) exist that explain the contact mechanics of solid spheres, they are not easily adapted to porous aggregates. Solving an equation of motion to find the result of collisions between dust aggregates yields good results for millimeter-sized aggregates, but the trend at other sizes does not reflect the results of experiments. It follows the sticking-bouncing transition as presented in Weidling et al. (2012), but the results of Kothe et al. (2013) and those presented in Section 6.3 show a much shallower decrease of the sticking velocity with increasing mass.

The model by Krijt et al. (2013) yields good results for collisions of solid, icy particles, but does not work with the parameters found for porous dust aggregates. At this time, only *n*-particle simulations (e.g. Schräpler et al. 2012) can reproduce experimental results reliably, but they are limited to very small aggregates. No viable analytical model that scales well to different aggregates sizes has been found yet.

With the new collision model by Kothe (2016) and the update to the transition zone between sticking and bouncing presented in this work, new growth simulations in the fashion of Zsom et al. (2010, 2011) have to be performed. This will not only reveal whether the recent results are beneficial to growth or not. They will also disclose which parameter combinations in collisions have to be investigated in future experiments and potentially show if silicates can grow large in PPDs by themselves or if other materials with higher surface energies are crucial for the formation of larger bodies.

Bibliography

Amelin, Y., Krot, A. N., Hutcheon, I. D., and Ulyanov, A. A. (2002). Lead Isotopic Ages of Chondrules and Calcium-Aluminum-Rich Inclusions. *Science*, 297:1678–1683.

Andrews, S. M. and Williams, J. P. (2007). High-Resolution Submillimeter Constraints on Circumstellar Disk Structure. *The Astrophysical Journal*, 659:705–728.

Anglada-Escudé, G., Amado, P. J., Barnes, J., Berdiñas, Z. M., Butler, R. P., Coleman, G. A. L., de La Cueva, I., Dreizler, S., Endl, M., Giesers, B., Jeffers, S. V., Jenkins, J. S., Jones, H. R. A., Kiraga, M., Kürster, M., López-González, M. J., Marvin, C. J., Morales, N., Morin, J., Nelson, R. P., Ortiz, J. L., Ofir, A., Paardekooper, S.-J., Reiners, A., Rodríguez, E., Rodríguez-López, C., Sarmiento, L. F., Strachan, J. P., Tsapras, Y., Tuomi, M., and Zechmeister, M. (2016). A terrestrial planet candidate in a temperate orbit around Proxima Centauri. *Nature*, 536:437–440.

Bai, X.-N. and Stone, J. M. (2010). Dynamics of Solids in the Midplane of Protoplanetary Disks: Implications for Planetesimal Formation. *The Astrophysical Journal*, 722:1437–1459.

Beitz, E., Güttler, C., Blum, J., Meisner, T., Teiser, J., and Wurm, G. (2011). Low-velocity Collisions of Centimeter-sized Dust Aggregates. *The Astrophysical Journal*, 736:34.

Beitz, E., Güttler, C., Weidling, R., and Blum, J. (2012). Free collisions in a microgravity many-particle experiment - II: The collision dynamics of dust-coated chondrules. *Icarus*, 218:701–706.

Blum, J. (2006). Dust agglomeration. *Advances in Physics*, 55:881–947.

Blum, J., Gundlach, B., Mühle, S., and Trigo-Rodriguez, J. M. (2014). Comets formed in solar-nebula instabilities! - An experimental and modeling attempt to relate the activity of comets to their formation process. *Icarus*, 235:156–169.

Blum, J. and Münch, M. (1993). Experimental investigations on aggregate-aggregate collisions in the early solar nebula. *Icarus*, 106:151.

Blum, J., Schräpler, R., Davidsson, B. J. R., and Trigo-Rodríguez, J. M. (2006). The Physics of Protoplanetesimal Dust Agglomerates. I. Mechanical Properties and Relations to Primitive Bodies in the Solar System. *The Astrophysical Journal*, 652:1768–1781.

Blum, J. and Wurm, G. (2000). Experiments on Sticking, Restructuring, and Fragmentation of Preplanetary Dust Aggregates. *Icarus*, 143:138–146.

Blum, J., Wurm, G., Kempf, S., and Henning, T. (1996). The Brownian Motion of Dust Particles in the Solar Nebula: an Experimental Approach to the Problem of Preplanetary Dust Aggregation. *Icarus*, 124:441–451.

Blum, J., Wurm, G., Kempf, S., Poppe, T., Klahr, H., Kozasa, T., Rott, M., Henning, T., Dorschner, J., Schräpler, R., Keller, H. U., Markiewicz, W. J., Mann, I., Gustafson, B. A., Giovane, F., Neuhaus, D., Fechtig, H., Grün, E., Feuerbacher, B., Kochan, H., Ratke, L., El Goresy, A., Morfill, G., Weidenschilling, S. J., Schwehm, G., Metzler, K., and Ip, W.-H. (2000). Growth and Form of Planetary Seedlings: Results from a Microgravity Aggregation Experiment. *Physical Review Letters*, 85:2426–2429.

Blum, J., Wurm, G., Poppe, T., and Heim, L.-O. (1998). Aspects of Laboratory Dust Aggregation with Relevance to the Formation of Planetesimals. *Earth Moon and Planets*, 80:285–309.

Blum, J., Wurm, G., Poppe, T., Kempf, S., and Kozasa, T. (2002). First results from the cosmic dust aggregation experiment codag. *Advances in Space Research*, 29:497–503.

Brisset, J., Heißelmann, D., Kothe, S., Weidling, R., and Blum, J. (2013). The suborbital particle aggregation and collision experiment (SPACE): Studying the collision behavior of submillimeter-sized dust aggregates on the suborbital rocket flight REXUS 12. *Review of Scientific Instruments*, 84(9):094501.

Brisset, J., Heißelmann, D., Kothe, S., Weidling, R., and Blum, J. (2016). Submillimetre-sized dust aggregate collision and growth properties. Experimental study of a multi-particle system on a suborbital rocket. *Astronomy and Astrophysics*, 593:A3.

Brownlee, D., Tsou, P., Aléon, J., Alexander, C. M. O. ., Araki, T., Bajt, S., Baratta, G. A., Bastien, R., Bland, P., Bleuet, P., Borg, J., Bradley, J. P., Brearley, A., Brenker, F., Brennan, S., Bridges, J. C., Browning, N. D., Brucato, J. R., Bullock, E., Burchell, M. J., Busemann, H., Butterworth, A., Chaussidon, M., Cheuvront, A., Chi, M., Cintala, M. J., Clark, B. C., Clemett, S. J., Cody, G., Colangeli, L., Cooper, G., Cordier, P., Daghlian, C., Dai, Z., D'Hendecourt, L., Djouadi, Z., Dominguez, G., Duxbury, T., Dworkin, J. P., Ebel, D. S., Economou, T. E., Fakra, S., Fairey, S. A. J., Fallon, S., Ferrini, G., Ferroir, T., Fleckenstein, H., Floss, C., Flynn, G., Franchi, I. A., Fries, M., Gainsforth, Z., Gallien, J.-P., Genge, M., Gilles, M. K., Gillet, P., Gilmour, J., Glavin, D. P., Gounelle, M., Grady, M. M., Graham, G. A., Grant, P. G., Green, S. F., Grossemy, F., Grossman, L., Grossman, J. N., Guan, Y., Hagiya, K., Harvey, R., Heck, P., Herzog, G. F., Hoppe, P., Hörz, F., Huth, J., Hutcheon, I. D., Ignatyev, K., Ishii, H., Ito, M., Jacob, D., Jacobsen, C., Jacobsen, S., Jones, S., Joswiak, D., Jurewicz, A., Kearsley, A. T., Keller, L. P., Khodja, H., Kilcoyne, A. L. D., Kissel, J., Krot, A., Langenhorst, F., Lanzirotti, A., Le, L., Leshin, L. A., Leitner, J., Lemelle, L., Leroux, H., Liu, M.-C., Luening, K., Lyon, I., MacPherson, G., Marcus, M. A., Marhas, K., Marty, B., Matrajt, G., McKeegan, K., Meibom, A., Mennella, V., Messenger, K., Messenger, S., Mikouchi, T., Mostefaoui, S., Nakamura, T., Nakano, T., Newville, M., Nittler, L. R., Ohnishi, I., Ohsumi, K., Okudaira, K., Papanastassiou, D. A., Palma, R., Palumbo, M. E., Pepin, R. O., Perkins, D., Perronnet, M., Pianetta, P., Rao, W., Rietmeijer, F. J. M., Robert, F., Rost, D., Rotundi, A., Ryan, R., Sandford, S. A., Schwandt, C. S., See, T. H., Schlutter, D., Sheffield-Parker, J., Simionovici, A., Simon, S., Sitnitsky, I., Snead, C. J., Spencer, M. K., Stadermann, F. J., Steele, A., Stephan, T., Stroud, R., Susini, J., Sutton, S. R., Suzuki, Y., Taheri, M., Taylor, S., Teslich, N., Tomeoka, K., Tomioka, N., Toppani, A., Trigo-Rodríguez, J. M., Troadec, D., Tsuchiyama, A., Tuzzolino, A. J., Tyliszczak, T., Uesugi, K., Velbel, M., Vellenga, J., Vicenzi, E., Vincze, L., Warren, J., Weber, I., Weisberg, M., Westphal, A. J., Wirick, S., Wooden, D., Wopenka, B., Wozniakiewicz, P., Wright, I., Yabuta, H., Yano, H., Young, E. D., Zare, R. N., Zega, T., Ziegler, K., Zimmerman, L., Zinner, E., and Zolensky, M. (2006). Comet 81P/Wild 2 Under a Microscope. *Science*, 314:1711–1716.

Bukhari Syed, M., Blum, J., Wahlberg Jansson, K., and Johansen, A. (2016). The role of pebble fragmentation in planetesimal formation I. Experimental study. *The Astrophysical Journal*.

Carrera, D., Johansen, A., and Davies, M. B. (2015). How to form planetesimals from mm-sized chondrules and chondrule aggregates. *Astronomy and Astrophysics*, 579:A43.

Clark, S. P. (1966). *Handbook of Physical Constants*. The Geological Society of America, Inc. Revised Edition.

Currie, T., Debes, J., Rodigas, T. J., Burrows, A., Itoh, Y., Fukagawa, M., Kenyon, S. J., Kuchner, M., and Matsumura, S. (2012). Direct Imaging Confirmation and Characterization of a Dust-enshrouded Candidate Exoplanet Orbiting Fomalhaut. *The Astrophysical Journal, Letters to the Editor*, 760:L32.

Deckers, J. and Teiser, J. (2014). Macroscopic Dust in Protoplanetary Disks - from Growth to Destruction. *The Astrophysical Journal*, 796:99.

Derjaguin, B. V., Muller, V. M., and Toporov, Y. P. (1975). Effect of contact deformations on the adhesion of particles. *Journal of Colloid and Interface Science*, 53:314–326.

Desch, S. J. (2007). Mass Distribution and Planet Formation in the Solar Nebula. *The Astrophysical Journal*, 671:878–893.

Dominik, C. and Nübold, H. (2002). Magnetic Aggregation: Dynamics and Numerical Modeling. *Icarus*, 157:173–186.

Dominik, C. and Tielens, A. G. G. M. (1997). The Physics of Dust Coagulation and the Structure of Dust Aggregates in Space. *The Astrophysical Journal*, 480:647.

Drążkowska, J. and Dullemond, C. P. (2014). Can dust coagulation trigger streaming instability? *Astronomy and Astrophysics*, 572:A78.

Drążkowska, J., Windmark, F., and Dullemond, C. P. (2014). Modeling dust growth in protoplanetary disks: The breakthrough case. *Astronomy and Astrophysics*, 567:A38.

Dullemond, C. P. and Dominik, C. (2008). Size-sorting dust grains in the surface layers of protoplanetary disks. *Astronomy and Astrophysics*, 487:205–209.

Dullemond, C. P., Hollenbach, D., Kamp, I., and D'Alessio, P. (2007). Models of the Structure and Evolution of Protoplanetary Disks. In Reipurth, B., Jewitt, D., and Keil, K., editors, *Protostars and Planets V*, pages 555–572.

Einstein, A. (1905). Über die von der molekularkinetischen Theorie der Wärme geforderte Bewegung von in ruhenden Flüssigkeiten suspendierten Teilchen. *Annalen der Physik*, 322:549–560.

Fressin, F., Torres, G., Charbonneau, D., Bryson, S. T., Christiansen, J., Dressing, C. D., Jenkins, J. M., Walkowicz, L. M., and Batalha, N. M. (2013). The False Positive Rate of Kepler and the Occurrence of Planets. *The Astrophysical Journal*, 766:81.

Gail, H.-P. (2004). Radial mixing in protoplanetary accretion disks. IV. Metamorphosis of the silicate dust complex. *Astronomy and Astrophysics*, 413:571–591.

Garaud, P., Meru, F., Galvagni, M., and Olczak, C. (2013). From Dust to Planetesimals: An Improved Model for Collisional Growth in Protoplanetary Disks. *The Astrophysical Journal*, 764:146.

Geretshauser, R. J., Meru, F., Speith, R., and Kley, W. (2011a). The four-population model: a new classification scheme for pre-planetesimal collisions. *Astronomy and Astrophysics*, 531:A166.

Geretshauser, R. J., Speith, R., Güttler, C., Krause, M., and Blum, J. (2010). Numerical simulations of highly porous dust aggregates in the low-velocity collision regime. Implementation and calibration of a smooth particle hydrodynamics code. *Astronomy and Astrophysics*, 513:A58.

Geretshauser, R. J., Speith, R., and Kley, W. (2011b). Collisions of inhomogeneous pre-planetesimals. *Astronomy and Astrophysics*, 536:A104.

Goldhirsch, I. and Zanetti, G. (1993). Clustering instability in dissipative gases. *Phys. Rev. Lett.*, 70:1619–1622.

Greenberg, R., Hartmann, W. K., Chapman, C. R., and Wacker, J. F. (1978). Planetesimals to planets - Numerical simulation of collisional evolution. *Icarus*, 35:1–26.

Greenwood, J. A. (2004). The theory of viscoelastic crack propagation and healing. *Journal of Physics D: Applied Physics*, 37(18):2557.

Gundlach, B., Kilias, S., Beitz, E., and Blum, J. (2011). Micrometer-sized ice particles for planetary-science experiments - I. Preparation, critical rolling friction force, and specific surface energy. *Icarus*, 214:717–723.

Güttler, C., Blum, J., Zsom, A., Ormel, C. W., and Dullemond, C. P. (2010). The outcome of protoplanetary dust growth: pebbles, boulders, or planetesimals?. I. Mapping the zoo of laboratory collision experiments. *Astronomy and Astrophysics*, 513:A56.

Güttler, C., Krause, M., Geretshauser, R. J., Speith, R., and Blum, J. (2009). The Physics of Protoplanetesimal Dust Agglomerates. IV. Toward a Dynamical Collision Model. *The Astrophysical Journal*, 701:130–141.

Haff, P. K. (1983). Grain flow as a fluid-mechanical phenomenon. *Journal of Fluid Mechanics*, 134:401–430.

Heim, L.-O., Blum, J., Preuss, M., and Butt, H.-J. (1999). Adhesion and Friction Forces between Spherical Micrometer-Sized Particles. *Physical Review Letters*, 83:3328–3331.

Heißelmann, D. (2015). Collisional properties of Saturnian ring particles.

Heißelmann, D., Blum, J., Fraser, H. J., and Wolling, K. (2010). Microgravity experiments on the collisional behavior of saturnian ring particles. *Icarus*, 206:424–430.

Heißelmann, D., Fraser, H., and Blum, J. (2007). Experimental Studies on the Aggregation Properties of Ice and Dust in Planet-Forming Regions. In *Proceedings of the 58th International Astronautical Congress 2007*. IAC-07-A2.1.02.

Hertz, H. (1881). Über die Berührung fester elastischer Körper. *Journal für die reine und angewandte Mathematik*, 92:156–171.

Jankowski, T., Wurm, G., Kelling, T., Teiser, J., Sabolo, W., Gutiérrez, P. J., and Bertini, I. (2012). Crossing barriers in planetesimal formation: The growth of mm-dust aggregates with large constituent grains. *Astronomy and Astrophysics*, 542:A80.

Jessberger, E. K., Stephan, T., Rost, D., Arndt, P., Maetz, M., Stadermann, F. J., Brownlee, D. E., Bradley, J., and Kurat, G. (2001). *Properties of interplanetary dust: Information from collected samples*, page 253. Springer Verlag, Berlin.

Johansen, A., Blum, J., Tanaka, H., Ormel, C., Bizzarro, M., and Rickman, H. (2014). The multifaceted planetesimal formation process. *Protostars and Planets VI*, pages 547–570.

Johansen, A., Oishi, J. S., Low, M.-M. M., Klahr, H., Henning, T., and Youdin, A. (2007). Rapid planetesimal formation in turbulent circumstellar disks. *Nature*, 448:1022–1025.

Johansen, A. and Youdin, A. (2007). Protoplanetary Disk Turbulence Driven by the Streaming Instability: Nonlinear Saturation and Particle Concentration. *The Astrophysical Journal*, 662:627–641.

Johansen, A., Youdin, A., and Mac Low, M. (2009). Particle Clumping and Planetesimal Formation Depend Strongly on Metallicity. *The Astrophysical Journal, Letters to the Editor*, 704:L75–L79.

Johnson, K. L. (1958). A note on the adhesion of elastic solids. *British Journal of Applied Physics*, 9(5):199.

Johnson, K. L., Kendall, K., and Roberts, A. D. (1971). Surface Energy and the Contact of Elastic Solids. *Royal Society of London Proceedings Series A*, 324:301–313.

Kalas, P., Graham, J. R., Chiang, E., Fitzgerald, M. P., Clampin, M., Kite, E. S., Stapelfeldt, K., Marois, C., and Krist, J. (2008). Optical Images of an Exosolar Planet 25 Light-Years from Earth. *Science*, 322:1345–1348.

Kataoka, A., Tanaka, H., Okuzumi, S., and Wada, K. (2013). Fluffy dust forms icy planetesimals by static compression. *Astronomy and Astrophysics*, 557:L4.

Kelling, T., Wurm, G., and Köster, M. (2014). Experimental Study on Bouncing Barriers in Protoplanetary Disks. *The Astrophysical Journal*, 783:111.

Kimura, H., Wada, K., Senshu, H., and Kobayashi, H. (2015). Cohesion of amorphous silica spheres: Toward a better understanding of the coagulation growth of silicate dust aggregates. *The Astrophysical Journal*, 812:67.

Kokubo, E. and Ida, S. (1998). Oligarchic Growth of Protoplanets. *Icarus*, 131:171–178.

Kokubo, E. and Ida, S. (2000). Formation of Protoplanets from Planetesimals in the Solar Nebula. *Icarus*, 143:15–27.

Kokubo, E. and Ida, S. (2002). Formation of Protoplanet Systems and Diversity of Planetary Systems. *The Astrophysical Journal*, 581:666–680.

Kokubo, E. and Ida, S. (2012). Dynamics and accretion of planetesimals. *Progress of Theoretical and Experimental Physics*, 2012(1):01A308.

Kothe, S. (2010). Multiple impakte staubiger körper. Diploma thesis, TU Braunschweig, Institut für Geophysik und extraterrestrische Physik.

Kothe, S. (2016). Mikrogravitationsexperimente zur Entwicklung eines empirischen Stoßmodells für protoplanetare Staubagglomerate.

Kothe, S., Blum, J., Weidling, R., and Güttler, C. (2013). Free collisions in a microgravity many-particle experiment. III. The collision behavior of sub-millimeter-sized dust aggregates. *Icarus*, 225:75–85.

Kothe, S., Güttler, C., and Blum, J. (2010). The Physics of Protoplanetesimal Dust Agglomerates. V. Multiple Impacts of Dusty Agglomerates at Velocities Above the Fragmentation Threshold. *The Astrophysical Journal*, 725:1242–1251.

Krause, M. and Blum, J. (2004). Growth and Form of Planetary Seedlings: Results from a Sounding Rocket Microgravity Aggregation Experiment. *Physical Review Letters*, 93(2):021103.

Krijt, S., Güttler, C., Heißelmann, D., Dominik, C., and Tielens, A. G. G. M. (2013). Energy dissipation in head-on collisions of spheres. *Journal of Physics D: Applied Physics*, 46(43):435303.

Krijt, S., Ormel, C. W., Dominik, C., and Tielens, A. G. G. M. (2015). Erosion and the limits to planetesimal growth. *Astronomy and Astrophysics*, 574:A83.

Kruss, M., Demirci, T., Koester, M., Kelling, T., and Wurm, G. (2016). Failed Growth at the Bouncing Barrier in Planetesimal Formation. *The Astrophysical Journal*, 827:110.

Lammel, C. (2008). Experimentelle Untersuchungen zur Fragmentation von Staubagglomeraten im Zweiteilchenstoß bei mittleren Geschwindigkeiten. Bachelor's thesis, Technische Universität Carolo Wilhelmina zu Braunschweig.

Lodders, K. (2003). Solar System Abundances and Condensation Temperatures of the Elements. *The Astrophysical Journal*, 591:1220–1247.

Loesche, C., Wurm, G., Kelling, T., Teiser, J., and Ebel, D. S. (2016). The motion of chondrules and other particles in a protoplanetary disc with temperature fluctuations. *The Monthly Notices of the Royal Astronomical Society*, 463:4167–4174.

Matthews, L. S., Kimery, J. B., Wurm, G., de Beule, C., Kuepper, M., and Hyde, T. W. (2016). Photophoretic force on aggregate grains. *The Monthly Notices of the Royal Astronomical Society*, 455:2582–2591.

Matthews, L. S., Land, V., and Hyde, T. W. (2012). Charging and Coagulation of Dust in Protoplanetary Plasma Environments. *The Astrophysical Journal*, 744:8.

Meisner, T., Wurm, G., Teiser, J., and Schywek, M. (2013). Preplanetary scavengers: Growing tall in dust collisions. *Astronomy and Astrophysics*, 559:A123.

Meru, F., Geretshauser, R. J., Schäfer, C., Speith, R., and Kley, W. (2013). Growth and fragmentation of centimetre-sized dust aggregates: the dependence on aggregate size and porosity. *The Monthly Notices of the Royal Astronomical Society*, 435:2371–2390.

Miller, S. and Luding, S. (2004). Cluster growth in two- and three-dimensional granular gases. *Physical Review E*, 69(3):031305.

Morbidelli, A., Crida, A., Masset, F., and Nelson, R. P. (2008). Building giant-planet cores at a planet trap. *Astronomy and Astrophysics*, 478:929–937.

Nübold, H., Poppe, T., Rost, M., Dominik, C., and Glassmeier, K.-H. (2003). Magnetic aggregation. II. Laboratory and microgravity experiments. *Icarus*, 165:195–214.

Nuth, III, J. A., Faris, J., Wasilewski, P., and Berg, O. (1994). Magnetically enhanced coagulation of very small iron grains. *Icarus*, 107:155.

O'Brien, D. P., Morbidelli, A., and Levison, H. F. (2006). Terrestrial planet formation with strong dynamical friction. *Icarus*, 184:39–58.

Okuzumi, S., Tanaka, H., Kobayashi, H., and Wada, K. (2012). Rapid Coagulation of Porous Dust Aggregates outside the Snow Line: A Pathway to Successful Icy Planetesimal Formation. *The Astrophysical Journal*, 752:106.

Okuzumi, S., Tanaka, H., Takeuchi, T., and Sakagami, M.-a. (2011). Electrostatic Barrier Against Dust Growth in Protoplanetary Disks. II. Measuring the Size of the ”Frozen” Zone. *The Astrophysical Journal*, 731:96.

Opsomer, E., Ludewig, F., and Vandewalle, N. (2012). Dynamical clustering in driven granular gas. *Europhysics Letters*, 99(4):40001.

Paraskov, G. B., Wurm, G., and Krauss, O. (2007). Impacts into weak dust targets under microgravity and the formation of planetesimals. *Icarus*, 191:779–789.

Pinte, C., Fouchet, L., Ménard, F., Gonzalez, J.-F., and Duchêne, G. (2007). On the stratified dust distribution of the GG Tauri circumbinary ring. *Astronomy and Astrophysics*, 469:963–971.

Poppe, T., Blum, J., and Henning, T. (2000a). Analogous Experiments on the Stickiness of Micron-sized Preplanetary Dust. *The Astrophysical Journal*, 533:454–471.

Poppe, T., Blum, J., and Henning, T. (2000b). Experiments on Collisional Grain Charging of Micron-sized Preplanetary Dust. *The Astrophysical Journal*, 533:472–480.

Poppe, T. and Schräpler, R. (2005). Further experiments on collisional tribocharging of cosmic grains. *Astronomy and Astrophysics*, pages 1–9.

Raymond, S. N., O'Brien, D. P., Morbidelli, A., and Kaib, N. A. (2009). Building the terrestrial planets: Constrained accretion in the inner Solar System. *Icarus*, 203:644–662.

Schräpler, R. and Blum, J. (2011). The Physics of Protoplanetesimal Dust Agglomerates. VI. Erosion of Large Aggregates as a Source of Micrometer-sized Particles. *The Astrophysical Journal*, 734:108.

Schräpler, R., Blum, J., Seizinger, A., and Kley, W. (2012). The Physics of Protoplanetesimal Dust Agglomerates. VII. The Low-velocity Collision Behavior of Large Dust Agglomerates. *The Astrophysical Journal*, 758:35.

Scott, E. R. D. and Krot, A. N. (2005). Thermal Processing of Silicate Dust in the Solar Nebula: Clues from Primitive Chondrite Matrices. *The Astrophysical Journal*, 623:571–578.

Seizinger, A. and Kley, W. (2013). Bouncing behavior of microscopic dust aggregates. *Astronomy and Astrophysics*, 551:A65.

Seizinger, A., Krijt, S., and Kley, W. (2013). Erosion of dust aggregates. *Astronomy and Astrophysics*, 560:A45.

Seizinger, A., Speith, R., and Kley, W. (2012). Compression behavior of porous dust agglomerates. *Astronomy and Astrophysics*, 541:A59.

Skorov, Y. and Blum, J. (2012). Dust release and tensile strength of the non-volatile layer of cometary nuclei. *Icarus*, 221:1–11.

Sorace, C., Louge, M., Crozier, M., and Law, V. (2009). High apparent adhesion energy in the breakdown of normal restitution for binary impacts of small spheres at low speed. *Mechanics Research Communications*, 36(3):364–368.

Tabor, D. (1977). Surface forces and surface interactions. *Journal of Colloid and Interface Science*, 58(1):2–13.

Teiser, J., Engelhardt, I., and Wurm, G. (2011). Porosities of Protoplanetary Dust Agglomerates from Collision Experiments. *The Astrophysical Journal*, 742:5.

Teiser, J. and Wurm, G. (2009). High-velocity dust collisions: forming planetesimals in a fragmentation cascade with final accretion. *The Monthly Notices of the Royal Astronomical Society*, 393:1584–1594.

Testi, L., Birnstiel, T., Ricci, L., Andrews, S., Blum, J., Carpenter, J., Dominik, C., Isella, A., Natta, A., Williams, J. P., and Wilner, D. J. (2014). Dust Evolution in Protoplanetary Disks. *Protostars and Planets VI*, pages 339–361.

Thornton, C. and Ning, Z. (1998). A theoretical model for the stick/bounce behaviour of adhesive, elastic-plastic spheres. *Powder Technology*, 99(2):154–162.

Trieloff, M. (2009). Chronology of the Solar System. *Landolt Börnstein*.

Tsiganis, K., Gomes, R., Morbidelli, A., and Levison, H. F. (2005). Origin of the orbital architecture of the giant planets of the Solar System. *Nature*, 435:459–461.

Wada, K., Tanaka, H., Okuzumi, S., Kobayashi, H., Suyama, T., Kimura, H., and Yamamoto, T. (2013). Growth efficiency of dust aggregates through collisions with high mass ratios. *Astronomy and Astrophysics*, 559:A62.

Wada, K., Tanaka, H., Suyama, T., Kimura, H., and Yamamoto, T. (2007). Numerical Simulation of Dust Aggregate Collisions. I. Compression and Disruption of Two-Dimensional Aggregates. *The Astrophysical Journal*, 661:320–333.

Wada, K., Tanaka, H., Suyama, T., Kimura, H., and Yamamoto, T. (2011). The Rebound Condition of Dust Aggregates Revealed by Numerical Simulation of Their Collisions. *The Astrophysical Journal*, 737:36.

Wahlberg Jansson, K. and Johansen, A. (2014). Formation of pebble-pile planetesimals. *Astronomy and Astrophysics*, 570:A47.

Walsh, K. J., Morbidelli, A., Raymond, S. N., O'Brien, D. P., and Mandell, A. M. (2011). A low mass for Mars from Jupiter's early gas-driven migration. *Nature*, 475:206–209.

Walsh, K. J., Morbidelli, A., Raymond, S. N., O'Brien, D. P., and Mandell, A. M. (2012). Populating the asteroid belt from two parent source regions due to the migration of giant planets – "The Grand Tack". *Meteoritics and Planetary Science*, 47:1941–1947.

Weidenschilling, S. J. (1977a). Aerodynamics of solid bodies in the solar nebula. *The Monthly Notices of the Royal Astronomical Society*, 180:57–70.

Weidenschilling, S. J. (1977b). The distribution of mass in the planetary system and solar nebula. *Astrophysics and Space Science*, 51:153–158.

Weidenschilling, S. J. and Cuzzi, J. N. (1993). Formation of planetesimals in the solar nebula. In Levy, E. H. and Lunine, J. I., editors, *Protostars and Planets III*, pages 1031–1060.

Weidling, R. (2010). Stöße in einem vielteilchensystem aus staubagglomeraten. Master's thesis, TU Braunschweig, Institut für Geophysik und extraterrestrische Physik.

Weidling, R. and Blum, J. (2015). Free collisions in a microgravity many-particle experiment. IV. - Three-dimensional analysis of collision properties. *Icarus*, 253:31–39.

Weidling, R., Güttler, C., and Blum, J. (2012). Free collisions in a microgravity many-particle experiment. I. Dust aggregate sticking at low velocities. *Icarus*, 218:688–700.

Weidling, R., Güttler, C., Blum, J., and Brauer, F. (2009). The Physics of Protoplanetesimal Dust Agglomerates. III. Compaction in Multiple Collisions. *The Astrophysical Journal*, 696:2036–2043.

Windmark, F., Birnstiel, T., Güttler, C., Blum, J., Dullemond, C. P., and Henning, T. (2012a). Planetesimal formation by sweep-up: how the bouncing barrier can be beneficial to growth. *Astronomy and Astrophysics*, 540:A73.

Windmark, F., Birnstiel, T., Ormel, C. W., and Dullemond, C. P. (2012b). Breaking through: The effects of a velocity distribution on barriers to dust growth. *Astronomy and Astrophysics*, 544:L16.

Wolszczan, A. and Frail, D. A. (1992). A planetary system around the millisecond pulsar PSR1257 + 12. *Nature*, 355:145–147.

Wurm, G. and Blum, J. (1998). Experiments on Preplanetary Dust Aggregation. *Icarus*, 132:125–136.

Wurm, G., Paraskov, G., and Krauss, O. (2005a). Ejection of dust by elastic waves in collisions between millimeter- and centimeter-sized dust aggregates at 16.5 to 37.5 m/s impact velocities. *Physical Review E*, 71(2):021304.

Wurm, G., Paraskov, G., and Krauss, O. (2005b). Growth of planetesimals by impacts at ~25 m/s. *Icarus*, 178:253–263.

Wyatt, M. C. (2008). Evolution of Debris Disks. *Annual Review of Astronomy and Astrophysics*, 46:339–383.

Youdin, A. N. and Goodman, J. (2005). Streaming Instabilities in Protoplanetary Disks. *The Astrophysical Journal*, 620:459–469.

Zsom, A., Ormel, C. W., Dullemond, C. P., and Henning, T. (2011). The outcome of protoplanetary dust growth: pebbles, boulders, or planetesimals?. III. Sedimentation driven coagulation inside the snowline. *Astronomy and Astrophysics*, 534:A73.

Zsom, A., Ormel, C. W., Güttler, C., Blum, J., and Dullemond, C. P. (2010). The outcome of protoplanetary dust growth: pebbles, boulders, or planetesimals? II. Introducing the bouncing barrier. *Astronomy and Astrophysics*, 513:A57.

Acknowledgments

First and foremost, I want to thank Jürgen Blum for entrusting me with the MEDEA project and supervising me during my PhD thesis. His door was always open for discussions and he was full of new, sometimes demanding, ideas both for the scientific work as well as for the design of the setup at all times. I learned a lot from him and really hope that he will one day find the missing puzzle pieces to understand planet formation.

I am grateful to Gerhard Wurm for reviewing my thesis, as well as for numerous discussions over the last years.

My special thanks go to Carsten Güttler, whose dedication and hard work helped a lot in designing and building the first versions of the MEDEA setup. Furthermore, he was a constant source of ideas on how to learn the most out of the experimental data scientifically.

The experiments presented in this work would not have been possible without the invaluable help from our fine-mechanics and electronics workshops. Kathrin Gebauer, Bernd Stoll, and Dennis Lühr did a great job in building various components for the MEDEA setup and offering their expertise and knowledge whenever some components had to be redesigned.

I want to thank Carsten Güttler, Stefan Kothe, Daniel Heißelmann, Julie Brisset, Eike Beitz, Ingo von Borstel, and Rainer Schräpler, for their help preparing various experimental campaigns and in conducting the experiments on site.

This work would not have been possible without the funding by the German Space Agency (DLR) under grant Nos. 50WM0936 and 50WM1236. Too many people at ZARM, Armadillo, Novespace, and Blue Origin were involved in providing microgravity platforms for the experiment and helping me prepare for the campagins to name them all, but I am very grateful to have worked with all of them.

I really appreciate the work Daniel Heißelmann invested when proofreading this thesis. His thorough search for typos and valuable comments really helped improving this work. I am also indebted to my brother Frederic, whose mathematical knowledge was invaluable in finding suitable methods for fitting the data.

The members of the IGEP made my time at this institute a very special and pleasant one. The genial atmosphere created by the colleagues was one of a kind. Whether for fruitful scientific discussions, help with programming, or for some distraction, I always knew someone to ask. The lunch breaks and subsequent table soccer matches, as well as numerous barbecues and other activities, will always remain in my memory.

I want to thank all of my friends, especially the Kochrunde, for their wonderful company. I sincerely hope that we will continue to spend great time and create delicious meals together.

Finally, I want to thank my parents, Ria, and the rest of my family for their inexhaustible support and motivation during my thesis.

Curriculum Vitae

Persönliche Daten:

Name:	Weidling
Vorname:	René
Geburtstag:	28.06.1985
Geburtsort:	Hameln, Niedersachsen
Staatsangehörigkeit:	Deutsch

Schulbildung:

1991 - 1995:	Grundschule Bakede, Bakede
1995 - 1997:	Hinrich-Wilhelm-Kopf-Schule, Bad Münder
1997 - 2004:	Schillergymnasium, Hameln
2004:	Abitur

Hochschulbildung:

2005 - 2010:	Physikstudium an der Technischen Universität Braunschweig
2008:	Bachelor of Science (Titel der Bachelorarbeit: “Der Einfluss von Vielfachstößen auf die Struktur von protoplanetaren Staubagglomeraten”)
2010:	Master of Science (Titel der Masterarbeit: “Stöße in einem Vielteilchensystem aus Staubagglomeraten”)
seit 2010:	Promotionsstudium an der Technischen Universität Braunschweig

Beruflicher Werdegang:

2008 - 2010:	Wissenschaftliche Hilfskraft am Institut für Geophysik und extraterrestrische Physik, Technische Universität Braunschweig
2010 - 2016:	Wissenschaftlicher Mitarbeiter am Institut für Geophysik und extraterrestrische Physik, Technische Universität Braunschweig